CYRIC

ANNUAL REPORT

2012-2013

(January 2012 - December 2013)

CYCLOTRON AND RADIOISOTOPE CENTER
TOHOKU UNIVERSITY

CYRIC

ANNUAL REPORT

2012-2013

(January 2012 - December 2013)

CYCLOTRON AND RADIOISOTOPE CENTER
TOHOKU UNIVERSITY
http://www.cyric.tohoku.ac.jp/

PREFACE

CYRIC was established in 1977 as an institution for carrying out research studies in various fields with the cyclotron and radioisotopes, and for training researchers of Tohoku University for safe treatment of radioisotopes and radiations. The cyclotron of CYRIC was manufactured by Sumitomo Heavy Industry Inc., Japan, form the design of CGR-Mev, France. The first beam was extracted at the end of December 1977. The scheduled operation of the cyclotron for research studies started in July 1979. We usually operate the cyclotron four whole days a week for research studies. The Great East Japan Earthquake occurred on March 11, 2011, the accelerator facilities were severely damaged because of strong shaking that continued for a few minutes. We have made great efforts on the recovery of our daily research activities until now. Our goals of efforts are “Resilience, Ingenuity, and Rebirth” during the three years. Fortunately, the scheduled operation of the cyclotron for collaborative research studies has re-started since October, 2012 from the one year and half interruption of our services. CYRIC consists of four buildings: cyclotron building (5400 m^2), radioisotope building (2000 m^2), molecular imaging research building (1000 m^2), and CYRIC Collaboration building (250 m^2). The molecular imaging research building has recently been renewed, and the President of Tohoku University, Dr. Susumu Satomi, attended the inauguration of the molecular imaging research building, which is recently completed. Fully functioning CYRIC facilities can ensure the further development in near future.

In conformity with the aim of establishment of CYRIC, the cyclotron has been used for studies in various fields of research, such as nuclear physics, nuclear chemistry, solid-state physics and element analysis by PIXE and activation, and for radioisotope production for use in engineering, biology and medicine. Seven divisions (Division of Accelerator, Division of Instrumentations, Division of Radio-pharmaceutical Chemistry, Division of Cyclotron Nuclear Medicine, Division of Radiation Protection and Safety Control, Division of Nuclear Fuel Science, and Division of Advanced Radiation Application) work for maintenance, development of facilities, and for studies of their individual research fields. The divisions belong to the graduate schools of Tohoku University.

The repair work on the accelerator facilities damaged by the Great East Japan

Earthquake was completed in October 2012. The beam time of both the K=110 MeV AVF cyclotron and the K=12 MeV AVF cyclotron were restarted, one and a half years after the earthquake. The reliability and availability of both the cyclotrons were returned to the level before the earthquake, though there were some minor troubles for a month after restarting the beam time. For a 10 GHz electron cyclotron resonance ion source, a gas mixing method was newly installed aiming at improvement in beam intensities and beam energies. Owing to the gas mixing method, the beam intensities were increased two to six times, and the beam energies were enhanced two to three times. Moreover, the ions of Kr and Xe were newly been provided for beam times at CYRIC.

The construction of the laser cooled RI source facility at TR5 and TOF, where the study on the fundamental symmetry and interaction will be performed, has been in progress. The development of the minimum setup of thermal ionizer, neutralizer, magneto-optical trapping system is ready now. The first trial experiment to trap the francium (^{210}Fr) was already done and the detailed analysis to check the performance is now going on. The measurement of the electric dipole moment of ^{210}Fr will be started after the magnetometer and magnetic field shield are installed. The study of the cluster structure of the atomic nuclei has obtained an impressive result. The direct 3α decay branch from the 0^+_2 state at E_x=7.65 MeV in ^{12}C, which is well known as the Hoyle state, has been measured with ^{12}C(^{12}C,3α)^{12}C reaction, and got the upper limit of 0.2%. This result will have important information on stellar nucleosynthesis and published in Physical Review Letters.

In the research program on proton therapy, a micro-pattern gaseous detector on the basis of gas electron multiplier technology (GEM detector) was developed as a new transmission beam monitor for charged particle therapy to obtain real-time information about parameters of a therapeutic beam. The feasibility tests were successfully performed using an 80-MeV proton beam to evaluate the lateral intensity distributions of a pencil beam. It is expected that the GEM-based transmission monitor provides real-time and simultaneous monitoring of various beam parameters for beam control in charged particle therapy.

In October 2012 production of PET nuclides with the HM12 Cyclotron was resumed after one and half year shutdown by the earthquake damage, and the routine production of PET probes was restarted after thorough preparations of the automated modules as well. Our original new tau protein imaging probe, [^{18}F]THK5117, was for the first time applied to clinical PET July 2013 and [^{11}C]PiB was introduced as an amyloid imaging probe at the same time. As clinical PET studies discontinued for repairs of the PET building August

2013, the numbers of PET probe productions in two years were comparatively smaller: [^{18}F]FDG (10 preparations), [^{18}F]FRP-170 (3), [^{18}F]THK5117 (6), [^{11}C]doxepin (32), [^{11}C]raclopride (6), [^{11}C]BF-227 (42) [^{11}C]PiB (10), and [^{15}O]water (11).

While a clinical PET study of [^{18}F]THK5117 had launched, further optimization of THK tau probes had been continued to reduce non-specific binding to subcortical white matter. In the end we developed a new candidate, THK-5351, which shows better brain kinetics and less non-specific binding to white matter than THK-5117. New researches on in vitro ^{11}C-labeled protein synthesis using cell-free protein synthesis system and [^{11}C]MET and on development of ^{18}F-labeled phosphonium compounds for imaging tissues rich in mitochondria had started and are achieving some promising results recently. Research on microfluidic ^{18}F-fluorination showed high reactivity of electrochemically concentrated [^{18}F]fluoride.

At last, clinical PET examinations started again in October 2012 after a long interval (a year and a half) due to the damage of Great Northeastern Earthquake in 2011. Later, fortunately or unfortunately, clinical PET examinations had to be stopped again for preparation of total renovation of the PET building. PET examinations were performed until August 2013. A part of examinations were done as so called “priority examinations”. We have introduced this new system in 2013, where the costs for PET examinations are charged through Technical Support Center of Tohoku University.

In spite of such limited time resources, several important papers were published in 2013 on beta-amyloid imaging, acetylcholine imaging and histamine H1 receptor imaging. First in the world as far as we know, beta-amyloid deposition in cardiac muscles of a patient with familial systemic amyloidosis was visualized using [^{11}C]BF-227. Effects of oral donepezil in patients with Parkinson’s disease with dementia was examined using [^{11}C]donepezil PET. In addition, initial papers on our new fluorinated amyloid imaging compound of Tohoku University ([^{18}F]FACT) were published. Histamine H1 receptor occupancy was first measured for antidepressants such as fluvoxamine and mirtazapine using [^{11}C]doxepin PET. Effect of psychological stress on brain histamine release was examined in healthy volunteers also using [^{11}C]doxepin PET.

The research program on PIXE analysis has been carried out by using a 4.5 MV Dynamitron accelerator at the Fast Neutron Laboratory, Graduate School of Engineering, Tohoku University, under the scientific tip up between CYRIC and FNL. The Dynamitron accelerator, beam line and other sub-system suffered damages by the earthquake. Almost all of the damages except for microbeam analysis system were temporarily recovered and the

research program on PIXE analysis was restarted in September 2011. Full-scale restoration work was started from April 2012 and completely finished at the end of FY 2012. Research studies using submilli-PIXE camera, microbeam analysis system, and micron-CT has been carried out. A total of 2000 hours of beam-time including test was served to this program without serious problems in FY2012 and 2013.

We conducted the beginners training for safe handling of radiation and radioisotopes twice a year in 2012 and 2013 for staffs and students of Tohoku University. The courses included 1) Radiositopes and radiation generators (460 trainees in 2012 and 475 trainees in 2013), 2) X-ray machines and electron microscope (338 trainees in 2012 and 361 trainees in 2013), and 3) Synchrotron Radiation (95 trainees in 2012 and 128 trainees in 2013). The total numbers of trainees in English classes for foreign students and scientists were 56 in 2012 and 79 in 2013, respectively.

There were no persons who were exposed occupational radiation more than 5.0 mSv among 199 (2012) and 289 (2013) radiation workers at CYRIC.

To separate the long-life and significant fission product elements from HLLW, a novel partitioning process for the treatment of HLLW has been studied experimentally based on column separation technique using macroporous silica-based adsorbents. The macroporous silica-based adsorbents were prepared by impregnating each extractant and molecule modifier 1-dodecanol into a macroporous silica/polymer composite support (SiO_2-P), respectively. The multistep process was suggested to be constructed five steps as follows. This process consists of (1) Cs and Rb are removed by the first separation column packed with Calix[4]arene-R14/SiO_2-P (Calix[4]arene-R14: 1,3-[(2,4-diethylheptylethoxy)oxy]-2,4-crown-6-calix[4]arene) adsorbent; (2) Sr and Ba are eluted out by the second separation column packed with DtBuCH18C6/SiO_2-P (DtBuCH18C6: 4,4',(5')-di-(tert-butyl-cyclohexano)-18-crown-6) adsorbent; (3)Pd is partitioned by the third separation column packed with MOTDGA-TOA/SiO_2-P (MOTDGA: *N*,*N*'-dimethyl-*N*,*N*'-di-*n*-octyl-thiodiglycolamide, TOA: Tri-*n*-octylamine) adsorbent; (4) Ru, Rh and Mo can be separated by the fourth separation column packed with TODGA/SiO_2-P (TODGA: *N*,*N*,*N*',*N*'-tetraoctyl-3-oxapentane-1,5-diamide) adsorbent; (5) Am is separated from RE by the fifth column is packed with *iso*butyl-BTP/SiO_2-P (*iso*butyl-BTP: 2,6-di(5,6-diisobutyl-1,2,4-triazin-3-yl) pyridine) adsorbent. The experimental results indicated that this partitioning process is essentially feasible.

Development of semiconductor gamma-ray detectors aiming for advanced radiation applications was carried out at Rokkasho branch of CYRIC. A compound semiconductor,

thallium bromide (TlBr), was studied as the gamma-ray detector material since it exhibits extremely high photon stopping power due to its high atomic number and high density. TlBr detectors with pixelated electrodes were developed in the Rokkasho branch. An energy resolution of ~1% FWHM at 662 keV was obtained from the detector at room temperature. Since the pixelated TlBr detectors exhibited high energy and position resolutions, they are promising for the application to Compton imaging devices.

We are most grateful to Tohoku University and to the Ministry of Education, Sports, Culture, Science and Technology for continuous support.

December 2014

Kazuhiko YANAI
Director
Cyclotron and Radioisotope Center, Tohoku University

EDITORS:

Kazuhiko YANAI
Ren IWATA
Yasuhiro SAKEMI
Manabu TASHIRO
Hiroshi WATABE

ASSISTANT EDITOR:

Ikuko TOJO

CONTENTS

IV. NUCLEAR MEDICAL ENGINEERING

V. PIXE AND ENVIRONMENTAL ANALYSIS

VI. RADIOCHEMISRTY AND NUCLEAR CHEMISTRY

VII. RADIOPHARMACEUTICAL CHEMISTRY AND BIOLOGY

In Memory of Professor Hiromichi Yamazaki

Suddenly Prof. Hiromichi Yamazaki, Director of Cyclotron and Radioisotope Center, Tohoku University, passed away early in the morning on April 8, 2012. It is only a week ago that he took a director position with big expectations to lead us for rapid restoration from the serious damage caused by the Great East Japan Earthquake.

He was born in Wakuya, Miyagi Prefecture on October 5, 1953 and grew up in Sendai. He entered Department of Engineering of Tohoku University and finished a PhD course at Graduate School of Engineering Tohoku University and obtained a doctorate in nuclear engineering in 1983. He immediately started to work as an assistant professor at Department of Nuclear Engineering (presently Quantum Science and Energy Engineering). His first major research field was radiochemistry in nuclear fuel and made an excellent contribution to developing nuclear reprocessing technology for irradiated nuclear fuel. He studied abroad at Prof. Choppin's laboratory of Florida State University for 1990-91. Then he turned his interest to PIXE analysis especially of environmental samples from river waters and aerosols in the atmosphere. He was also involved in developing PET cameras and related devices. Later he developed the production and labeling of ^{124}I and succeeded in its application to imaging of the rat brain with a high-resolution semiconductor animal PET scanner.

In 2006 he became a professor at CYRIC and since then he worked very actively for radiation protection and management throughout the university as a chairperson of the Committee for Prevention of Radiation Hazards. He also devoted himself to the education of safety handling of radiation and radioisotopes for university students and faculty engaged in research using radioactive materials. CYRIC gained two divisions, Division of Nuclear Fuel Science and Division of Advanced Radiation Application as a detached lab in

Rokkasho in 2009. As the research fields of these new labs were literally overlapped by those in which he had made numerous scientific achievements in his career, he was indeed expected to lead them as not only a director but also excellent chemist.

On March 11 2011, the Tohoku region was struck by a huge earthquake, the Great East Japan Earthquake, and the following merciless attack of a giant tsunami on the whole east coast killed nearly 20,000 people and caused the meltdown of nuclear fuels at three Fukushima Daiichi reactors resulting in high radioactive release over the neighboring districts. Although CYRIC suffered serious damages especially on the 930 cyclotron, Prof. Yamazaki was always at the head of careful investigation of damages one by one on instruments and did his best towards the restoration of the CYRIC facilities. At that time he was also busy as a core member of the Tohoku University group with monitoring radiation in the field and measuring radioactive contamination in fish and crops. He often visited the southern area of Miyagi Prefecture and even Fukushima Prefecture to decontaminate soils on the playgrounds of schools and kindergartens or to receive people coming for advices about radiation and contamination. He worked hard outdoors even on hot days for decontamination and by riversides even on cold windy days for sampling waters for one year after the disaster.

Apart from his distinguished scientific activities, Prof. Yamazaki was truly a man of a gentle and warm nature. He was deeply respected by his students and loved by all of us. We shall keep a good memory of him with his calm and elegant smile.

Ren Iwata
Shigeo Matsuyama
Keizo Ishii

I. NUCLEAR PHYSICS

I. 1. Further Improvement of the Upper Limit on the Direct 3α Decay from the Hoyle State

Itoh M., Ando S., Aoki T., Arikawa H., Ezure S., Harada K., Hayamizu T., Inoue T., Ishikawa T., Kato K., Kawamura K., Sakemi Y., and Uchiyama A.

Cyclotron and Radioisotope Center, Tohoku University

The 0_2^+ state at E_x = 7.65 MeV in ^{12}C plays an important role in the creation of the ^{12}C nucleus in stellar nucleosynthesis. The ^{12}C nucleus is produced by the triple-α reaction: two α particles form the resonance state of ^{8}Be at first, and the short-lived ^{8}Be captures a third particle before decaying back to two α particles. Fred Hoyle claimed that the capture of a third α particle proceeds through a resonant state in ^{12}C near the α + ^{8}Be threshold, thus, enhancing the triple-α reaction rate[1]. This resonant state, 0_2^+, in ^{12}C was discovered soon after his prediction[2]. For that reason, the 0_2^+ state in ^{12}C is called the Hoyle state.

The structure of the Hoyle state is highly related to the triple-α reaction rate, since it is considered to have a typical 3α cluster structure. According to the microscopic α cluster models, the Hoyle state has been considered to have a dilute gaslike structure in which the α clusters are loosely coupled to each other[3,4]. About a decade ago, Tohsaki *et al*. proposed that this dilute α gaslike structure was similar to the Bose-Einstein condensation of α clusters in the nucleus[5]. Recently, a lattice calculation with the chiral effective field theory, which is one of the *ab initio* calculations, succeeded in reproducing the excitation energy of the Hoyle state in ^{12}C. It indicated that the Hoyle state was considered to have a “bent-arm” or obtuse triangular configuration[6]. Therefore, its configuration of 3α clusters is still controversial.

It is difficult to determine the structure of the nuclear excited state, especially the unbound states, experimentally. One possible way is the decay particle measurement. Recently, Rana *et al.* reported the nonzero value of the direct 3α decay branch from the Hoyle state[7]. Although it could be evidence for the 3α cluster structure of the Hoyle state, it

was incompatible with the previous experimental result as the upper limit of 0.5% on the direct 3α decay branch[8].

In order to investigate the structure of the Hoyle state, experimentally, we have performed a measurement of decay α particles from the Hoyle state via the $^{12}C(^{12}C,^{12}C^{*}[3\alpha])^{12}C$ reaction using the large scattering chamber in Target Room 4. The $^{12}C^{4+}$ beam was accelerated up to 110 MeV by AVF cyclotron, and bombarded to the self-supported carbon foil with a thickness of 50 μg/cm^2. The decay 3α particles were detected by the double-sided silicon strip detector (DSSD) with a size of 50 × 50 mm^2 and with a thickness of 1500 μm which has 16 × 16 strips oriented vertically in the front side and horizontally in the rear side. The recoiling ^{12}C particles were caught by a silicon detector with a thickness of 150 μm at 67°. This angle corresponds to that of the third maximum of the angular distribution for the $^{12}C(^{12}C,^{12}C^{*}[0_2^{+}])^{12}C$ reaction. The silicon detectors were kept cooling around 0 ℃ during the experiment. Figure 1 shows the kinematics of the $^{12}C(^{12}C,^{12}C^{*}[3\alpha])^{12}C$ reaction and the energy spectrum of the recoiling ^{12}C particles. The thick solid line in Fig. 1(b) shows that in coincidence with the decay 3α particles. It indicates only the Hoyle state can be coincident with the decay 3α particles.

To visualize the energy correlation of the decay 3α particles, the symmetric Dalitz plot is adopted. Figure 2 shows the symmetric Dalitz plot in the present experiment. We compared it with the Monte Carlo simulation of the experiment. Three decay mechanisms were compared to the result of the experiment. The first is the sequential decay (SD) through the ^{8}Be. The second is the direct decay with an equal energy of three α particles (DDE). The third is the direct decay to the phase space uniformly (DDΦ). In order to obtain the branching ratio for each decay mechanism, we fitted the normalized energy distribution for the highest energy among the decay 3α particles with those obtained in the simulation. The normalized energy, ε_x, is defined as $\varepsilon_x = E_x/(E_i+E_j+E_k)$, x=*i*,*j*,*k*. $E_{i,j,k}$ are kinetic energies of the decay 3α particles, and defined as $E_i > E_j > E_k$. Figure 3 shows the result of the fit. The decay branch of the SD mechanism was almost 100%. After the statistical treatment, the upper limit of 0.2% on the DDE and DDΦ mechanisms was obtained. In Fig. 3, results obtained by Rana et al. were also shown. It seems to reproduce the shoulders in Fig. 3. However, from the result of the simulation, we found they were originated from the misassignment of the position of decay α particles due to the finite energy resolution of the DSSD.

This result has been already published in Ref. 9.

References

1) Hoyle F., Astrophys. J. Suppl. Ser. **1** (1954) 121.
2) Cook C.W., Fowler W.A., Lauritsen C.C. and Lauritzen, Phys. Rev. **107** (1957) 508.
3) Uegaki E. *et al*, Prog. Theor. Phys.
4) Kamimura K., Nucl. Phys. A
5) Tohsaki A. *et al.*, Phys. Rev. Lett. **87** (2001) 192501.
6) Epelbaum E. *et al.*, Phys. Rev. Lett. **109** (2012) 252501.
7) Rana T.K. *et al.*, Phys. Rev. C **88** (2013) 021601(R).
8) Kirsebom O.S. *et al.*, Phys. Rev. Lett. **108** (2012) 202501.
9) Itoh M. *et al*, Phys. Rev. Lett. **113** (2014) 102501.

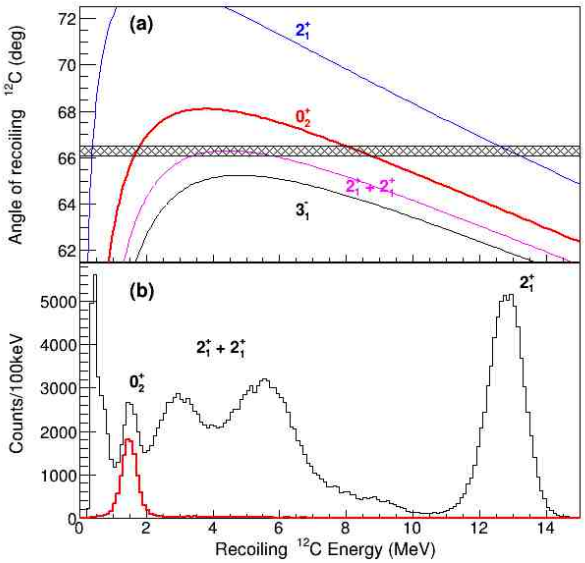

Figure 1. (a) The kinematics of the $^{12}C(^{12}C,^{12}C^*[3\alpha])^{12}C$ reaction. The of the 4.44 MeV 2_1^+, the 7.65 MeV 0_2^+, and the 9.64 MeV 3^- states are drawn by the blue, the red, and the black lines. The mutual 2_1^+ excitations for the beam and the target ^{12}C is indicated by the magenta line. (b) Energy spectra of the recoiling ^{12}C at 67° are shown. The black and red lines show that of the singles trigger and the coincidence energy spectrum.

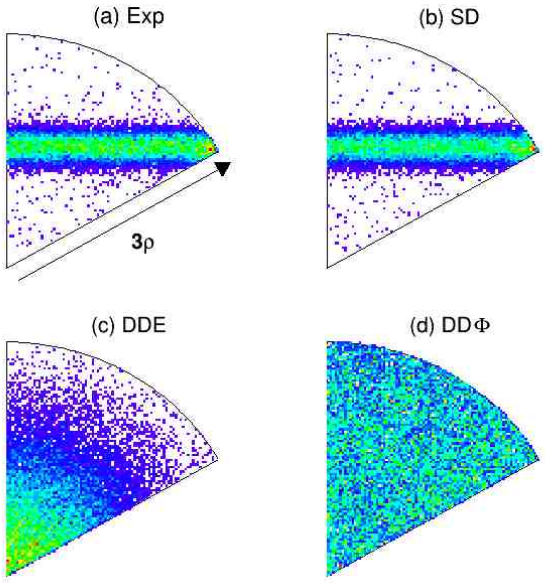

Figure 2. Symmetric Dalitz plots for (a) the experiment, (b) the sequential decay (SD), (c) the direct decay with an equal energy of three α particles (DDE) and (d) the direct decay to the phase space uniformly (DDΦ) are shown. The Dalitz plots for the SD, DDE and DDΦ are obtained by the Monte Carlo simulation.

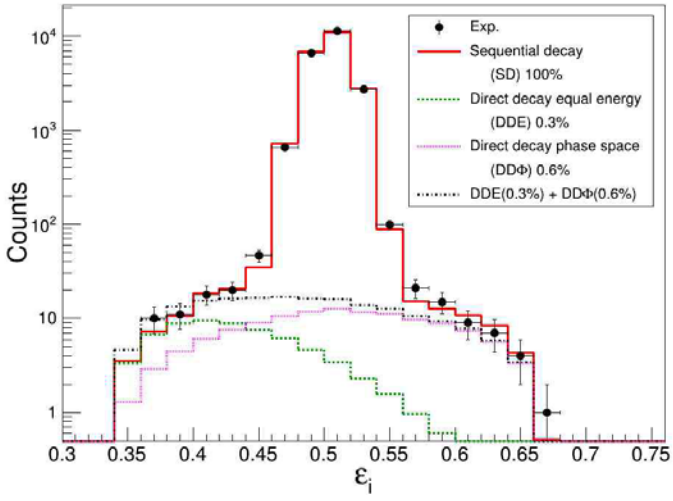

Figure 3. The normalized energy distribution for the highest energy of the decay 3α particles. The experimental result was reproduced completely by the Monte Carlo simulation of the SD mechanism.

I. 2. Test Experiment of the 0° Measurement of Decay α Particles in the $^{12}C(^{12}C,3\alpha)$ Reaction

Ando S.[1], Itoh M.[1], Aoki T.[1], Arikawa H.[1], Ezure S.[1], Harada K.[1], Hayamizu T.[1], Inoue T.[1,2], Ishikawa T.[1], Kato K.[1], Kawamura H.[1,2], Uchiyama A.[1], and Sakemi Y.[1]

[1]*Cycrotoron and Radioisotope Center, Tohoku University*
[2]*Frontier Research Institute for Interdisciplinary Sciences (FRIS), Tohoku University*

The 0_2^+ state at E_x = 7.65 MeV in ^{12}C is called Hoyle state, which plays an important role in the creation of the ^{12}C nucleus in stellar nucleosynthesis. Moreover, in nuclear structure studies, the Hoyle state is considered to have a dilute gaslike structure in which the α clusters are loosely coupled to each other[1,2]. Because of these astrophysical importance and specificity in nuclear structure, it has been studied from both theory and experiment for a long time. However, clear evidence for the dilute α gaslike structure has not been obtained, yet. About a decade ago, Tohsaki et al. proposed that this dilute α gaslike structure was similar to the Bose-Einstein condensation of α clusters in the nucleus[3]. Recently, the 2_2^+ state at 10 MeV has been found[4-6]. It is considered to be the 2^+ excitation of the Hoyle state. However, since there is not enough experimental evidence for the structure of the Hoyle state, it is still controversial.

To study the structure of the Hoyle state, we performed the measurement of the decay 3α particles via the $^{12}C(^{12}C, ^{12}C^*(0_2^+)[3\alpha])^{12}C$ reaction at the 41 course at CYRIC. By measuring the momenta and scattering angles of decay three α particles from the Hoyle state, the relative momentum distribution was obtained. This relative momentum distribution is considered as reflecting the α structure of the Hoyle state. Figure 1 shows a picture of the inside of the scattering chamber. The $^{12}C^{4+}$ beam was accelerated up to 110 MeV by the K110 AVF cyclotron and bombarded on a self-supporting natural carbon foil target with a thickness of 200 μg /cm^2 (or 100 μg /cm^2) installed in the scattering chamber. The incident ^{12}C was inelastically excited to the Hoyle state and the breakup three α particles were detected in a double-sided Si strip detector (DSSD) with a size of 50 × 50 mm and a thickness of 1,500 μm. The DSSD consists of 16 × 16 strips oriented vertically in

the front side and horizontally in the rear side with a size of 3 × 50 mm. The positions of three α particles at the DSSD which was located at 290 mm from the target, were determined by comparing the energies obtained from the strips in the front and the rear sides. For monitoring the beam position, the recoiling ^{12}C of elastic scattering was caught in the silicon detectors at -79.35° (SSD1) and 79.35° (SSD2). The latest experimental result for the upper limit of the direct decay branching ratio from the Hoyle state is less than 5 × 10^{-3}. To determine the structure of the Hoyle state better than the previous result, more than 20,000 events of the decay three α particles from the Hoyle state is needed.

The purpose of this test experiment was to find an efficient setup for detecting the three α particles from the Hoyle state. In the previous experiment, we measured decay three α particles at the DSSD angle of 7.5° to the ^{12}C beam axis. The event rate of the Hoyle state in that experiment was 130 events per hour. In this experiment, in order to increase the detection efficiency of the three α, we measured by condition that DSSD was located at 0°. There are two reasons for this condition of DSSD. The first reason is that cross section of the ^{12}C(^{12}C, ^{12}C*(0_2^+))^{12}C reaction is maximum at 0°. The second reason is that the relative energy of the decay three α particles is small enough to detect by a DSSD. However, in this condition, the background would become much larger than the measurement at 7.5° because the ^{12}C beam enters on the DSSD directly. Thus, we installed a beam-stopper together with an Al plate in 4.7 mm front of the DSSD. The thickness of the Al plate was 200 μm, and the size of beam-stopper was 6 mm ϕ, which is enough to stop the ^{12}C beam. The protons and deuterons events generated by the reaction were rejected by the VETO signal from a plastic scintillator located just behind the DSSD. To reduce the trigger rate from the background, we studied the trigger condition by changing multiplicity of DSSD signals from 1 to 3. In order to optimize the measurement, we varied the combination of the following conditions.

1. Trigger multiplicity of discriminator module : 1, 2, 3
2. VETO signal by plastic scintillator : ON or OFF
3. Beam Stopper : IN or OUT
4. Thickness of the ^{12}C target : 100 μg/cm^2 or 200 μg/cm^2

The sum of kinetic energies of detected three α particles and recoiling ^{12}C is equal to the beam energy being reduced by separation energy of threeα particles from ^{12}C . The energy of recoiling ^{12}C at 0° is much small. Thus, in the spectrum of that, the peak of the Hoyle state is located about 103 MeV. Figures 2(a) and, 2(b) show the spectra of the

summed kinetic energies of three detected particles respectively. Figure 2(a) shows the spectrum in condition (a) that trigger multiplicity sets 2, VETO is ON, beam-stopper is OUT, and thickness of ^{12}C is 200 μg/cm^2. On the other hand, Fig. 2(b) shows the spectrum in condition (b) where existence of beam-stopper is only difference from the condition (a). The entries in Figs. 2(a) and 2(b) correspond to the measurement time. By comparing these two spectra, the background in Fig. 2(b) was less than in Fig. 2(a), and it is possible to find the definitive peak of the Hoyle state in Fig. 2(b). Consequently, the setup in condition (b) found to be the best for detecting the three α particles decayed from the Hoyle state. The event rate was 700 events per hour. However, the setup in condition (b) is not suitable for detecting the α particles via the direct decay from the Hoyle state. Figure 3 shows the symmetric Dalitz-plot of the α particles from the Hoyle state in the condition (b). The X- and Y- axis labels, x and y, of the Daltz-plot are defined in Refs. 7-9. The x and y are calculated by the α particles energies in the $^{12}C^*$ rest frame normalized to the total kinetic energies of the decay 3α particles. Different decay mechanisms result in different Dalitz-plot distributions[8-9]. In Fig. 3, we found that the α particles detected in the condition (b) were all α particles via sequential decay[8-9]. The cause of this problem is the small direct decay branch of the Hoyle state, the upper limit is 0.2%[8-9]. In Fig. 2(b), there are events which have the energy higher than 103 MeV. The summed energy of the decay three α particles cannot be higher than 103 MeV, because the separation energy of three α particles is 7.27 MeV. Thus, the background are contained in the peak of the Hoyle state in condition (b). We considered a reason for background is accidental coincidence. Since we cannot remove these background, this setup is not suitable for the precise measurement of the small branch reaction of the direct decay from the Hoyle state. Further development for clean measurement is in progress.

References

1) Uegaki E., et al., *Prog. Theor. Phys.* **57** (1977) 1262.
2) Kamimura K., *Nucl. Phys.* A **351** (1981) 456.
3) Tohsaki A., et al., *Phys. Rev. Lett.* **87** (2001) 192501.
4) Itoh M., et al., *Phys. Rev.* C **84** (2011) 054308.
5) Freer M., et al., *Phys. Rev.* C **80** (2009) 041303(R).
6) Zimmerman W.R., et al., *Phys. Rev. Lett.* **110** (2013) 152502.
7) Kirsebom O.S., et al., *Phys. Rev. Lett.* **108** (2012) 202501.
8) Itoh M., et al., *Phys. Rev. Lett.* **113** (2014) 102501.
9) Itoh M., et al., *CYRIC Annual Report* 2012-2013.

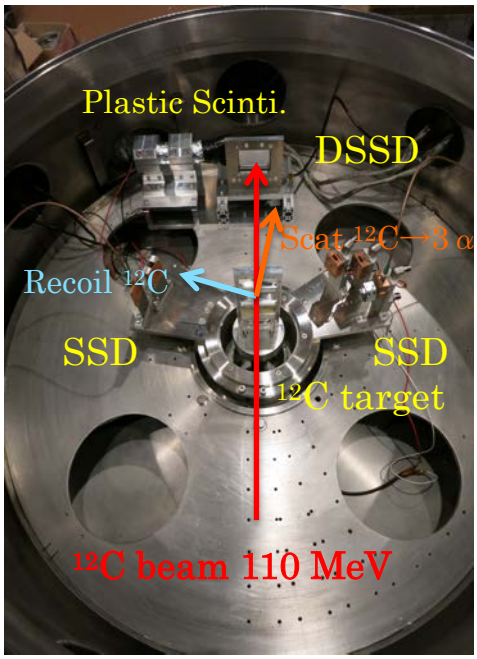

Figure 1. Detectors setup in the large Scattering chamber.

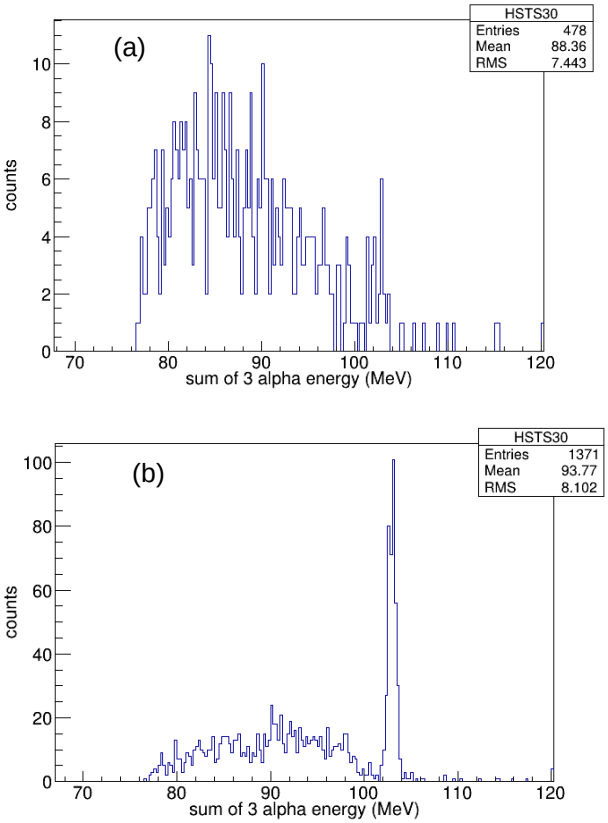

Figure 2. The spectra of the summed kinetic energies of three detected particles. (a): The spectrum in condition that trigger multiplicity sets 2, VETO is ON, beam-stopper is OUT, and thickness of ^{12}C is 200 μg/cm^2. (b): The spectrum in same condition as condition (a), except for beam-stopper.

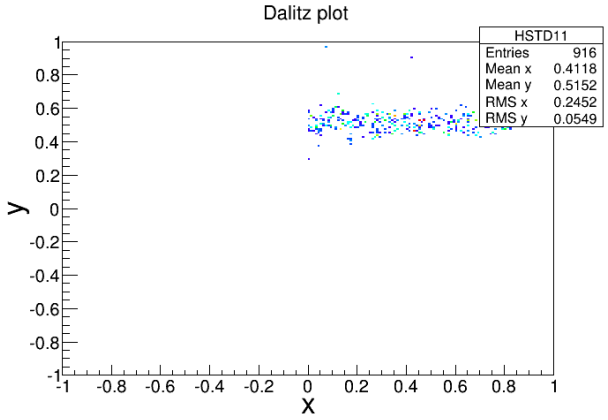

Figure 3. Symmetric Dalitz plots of the α particles from the Hoyle state in the condition (b) are shown. The X and Y labels, x and y, are defined in Ref. 8.

I. 3. Present Status of the Experimental Project for the Study on the Fundamental Symmetry Using Laser Cooled Radioactive Atoms

Sakemi Y.[1], Ando T.[1], Aoki T.[1], Aoki T.[2], Arikawa H.[1], Ezure S.[1], Harada K.[1], Hayamizu T.[1], Inoue T.[1,3], Ishikawa T.[1], Itoh M.[1], Kato K.[1], Kawamura H.[1,3], and Uchiyama A.[1]

[1]*Cyclotron and Radioisotope Center, Tohoku University*
[2]*Graduate school of Arts and Sciences, University of Tokyo*
[3]*Frontier Research Institute for Interdisciplinary Sciences, Tohoku University*

Matter-antimatter asymmetry (CP violation) is a subject that has relevance in many branches of physics. It has been observed in the decays of K and B mesons, and the results can be understood under the light of the work of Prof. Kobayashi and Maskawa in the context of the Standard Model (SM). However, the origin of CP violation is still not well understood. The observed matter-antimatter asymmetry in the Universe is linked to CP violation which is associated with unknown physics Beyond the Standard Model (BSM). In the contemporary era of the Large Hadron Collider (LHC) in which physicists in the world are waiting to find answers to many outstanding questions, attempts to look for new physics via non-accelerator probes are complementary and very significant. The experiments to search for the electric dipole moment (EDM) of elementary particles and CP violating interactions such as the electron-quark CP odd interactions certainly fall into the category of the highest precision low energy physics. They become important to know which energy should be explored for BSM with the next generation accelerator ILC.

The field of CP violation is vast and is growing rapidly and independently in different research areas. It needs the collaborations and coherent works between many areas of physics such as particle, nuclear, atomic and molecular physics and involves theoretical, mathematical, computational and experimental methods. In the case of the atomic EDM, the electron EDM is enhanced with 895 times for the heaviest alkali element francium (Fr). Also the observable of the parity non-conservation of nuclear system, so called anapole moment, is enhanced in Fr. At present, the development of the laser cooled Fr source at TR5 and TOF, CYRIC has been in progress to study the fundamental symmetry and interactions.

In this experimental project, the Fr is produced with the nuclear fusion reaction with ^{18}O beam supplied from AVF cyclotron and ^{197}Au target, and ionized by the high intensity thermal ionizer. The extracted Fr ion beam is transported to the neutralizer to get the neutral Fr atoms. In this year, we have installed the Wien filter in the beam line, which is the velocity filter to reject the residual atoms emitted from many sources with high temperature around the thermal ionizer, and to improve the purity of the Fr beam. The Fr atoms are loaded into the magneto-optical trap (MOT) to realize the cooled Fr source. The test experiments have been done already to observe the trapped Fr with MOT, and the detailed analysis is in progress.

The trapped Fr in the 1st MOT will be loaded to the 2nd MOT and transported to the EDM measurement cell with optical tweezers using optical dipole force. Then, the Fr atoms are trapped with optical dipole trap and optical lattice in the final stage in this project. The experimental overview is shown in Fig. 1. The double MOT system and optical dipole trap have been developed already and studied in more detail by stable element Rb. The optical dipole trap is treated, in principle, as the same technique of 1 dimensional optical lattice, so we have already accumulated the cooling and trapping techniques required for the EDM measurement. The EDM has to be measured in the magnetic field shield with co-magnetometer. The design of the shield system and the development of the prototype of the magnetometer have been done, and all the components will be studied further with online using the accelerator and offline experiment to check the performance to realize the EDM measurement accuracy with 10^{-29} ecm in next year.

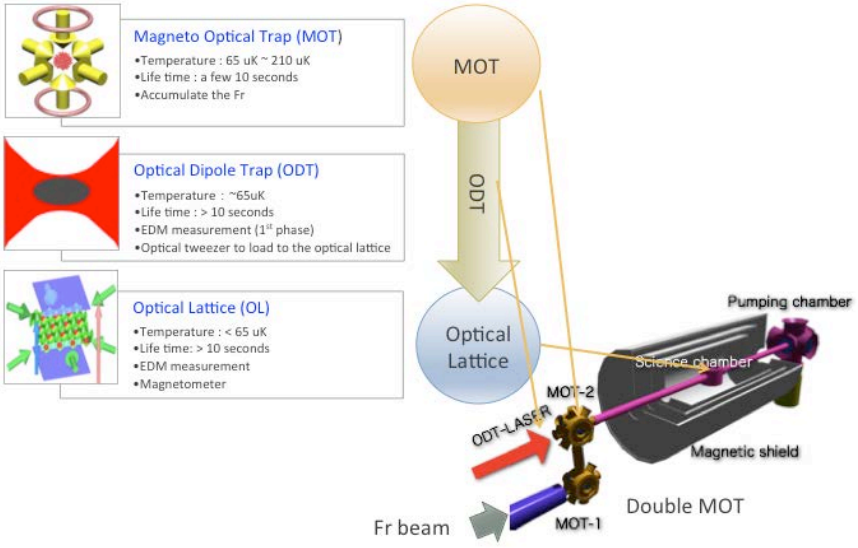

Figure 1. Overview of setup for the EDM measurement system.

I. 4. Development of an Ion-to-Atom Converter Based on the Orthotropic Source for a Magneto-Optical Trapping of Francium

Kawamura H.[*], Sato T.[†], Arikawa H., Ezure S., Harada K., Hayamizu T., Inoue T.[*], Ishikawa T., Itoh M., Kato T., and Sakemi Y.

Cyclotron and Radioisotope Center, Tohoku University

A device converting ions to neutral atoms has been developed for a magneto-optical trapping of francium toward a test of fundamental symmetries. The neutralized francium atoms were successfully observed and the parameter dependence of the device was studied. The current value of the ion-to-atom conversion efficiency does not reach our goal. Hence, further developments are required for the achievement of the magneto-optical trapping of francium.

Introduction

Francium (Fr), which is the heaviest alkali element, is a promising candidate for the precise testing of physics models[1)]. We plan to discover the new physics beyond the standard model through a test of fundamental symmetries using Fr atoms. A pending problem is to capture the Fr, produced via a nuclear reaction, in a magneto-optical trap (MOT).

The first issue confronting the laser cooling of radioactive isotopes produced using an accelerator is how to extract the objective element from a production target. In cases where Fr is produced by the reaction between oxygen beam and gold target, most Fr produced is desorbed as univalent positive ions. In fact, the groups employing this reaction extract and transport the Fr ions using electrostatic fields[2,3)].

When the Fr is extracted as an ion, the next issue is the neutralization of the ion. For the purpose of our Fr project, a positive Fr ion is not useful at all, because we utilize the

[*]*Present address: Frontier Research Institute for Interdisciplinary Sciences (FRIS), Tohoku University*

[†]*Present address: Department of Physics, Tokyo Institute of Technology*

interaction of the heavy nucleus and the outermost unpaired electron. Therefore, the neutralization process of Fr ions is necessary. In experiments performing MOT of radioactive isotopes, the general method is thermal neutralization using a metal target with a small work function, such as yttrium (Y). Since the atoms are emitted diffusely from the metal surface, some artifice is required in order to use these atoms as an atomic beam.

To form an atomic beam from an ion beam, we developed an ion-to-atom converter (KNB-01 from Kitano Seiki Co., Ltd.) based on the orthotropic source[4]. This converter consists of a small Y target and a platinum oven surrounding the target. In principle, the converter can make a collimated atomic beam that suppresses the loss of the incident ions. With a collimated beam, it is expected that the efficient MOT will be realized using Zeeman slowing.

In a pilot setup where the converter was combined with a dedicated Rb ion source[5], ^{87}Rb was neutralized and captured in MOT (without Zeeman slowing). After the pilot experiment, the converter was installed on the 51 course in target room No. 5 and in the TOF room, where the secondary Fr beam line is located[6]. In this beam line, the ^{87}Rb produced by the Fr ion source was neutralized with this converter and captured in the same way. After that, the experiment using Fr was performed to be sure of the neutralization of the Fr[7].

Experiment and results

The experiment challenged with Fr after the operation test and performance estimate with Rb. Before Fr MOT, the neutralization of Fr was confirmed using a solid state detector (SSD) that identified the particle by measuring decay-α particles. An ion reflector electrode was placed in front of the SSD to sweep out stray ions as shown in Fig. 1.

SSD is susceptible to heat and light. In this experiment, this SSD was cooled using a Peltier device and water chiller. Water leakage inside the vacuum chamber worsened the vacuum pressure on the order of 10^{-3} Pa, but this was not critical for this neutralization experiment. The temperature of the SSD did not rise above 15^{o}C and it worked well, even though the converter was heated to 1000^{o}C. To overcome the light problem, a thin aluminum foil (800 nm) cover was placed on the SSD. Accordingly, it was expected that the energy resolution of the detector would be ~100 keV. Since the α-particle energies of ^{209}Fr and ^{210}Fr are 6.646 MeV and 6.543 MeV, respectively, a better resolution is desired

in order to resolve these energies.

Figure 2 shows an acquired α spectrum. There are clearly different events, with a peak of ^{241}Am as the source for an energy calibration. Owing to the low resolution, these events do not contradict α particles of $^{208\text{-}211}$Fr. Considering the original production yield, ^{210}Fr should dominate. In the following analyses, the event number in this peak was counted.

The ion-to-atom converter and the detector based on SSD have adjustable parameters: that include the temperature of the converter, the neutralizer target voltage, the ionizer oven voltage, the shield voltage, and the voltage of the ion reflector in front of the SSD. The standard operation parameter settings are the temperature at 1000^{o}C, the neutralizer at -2000 V, the ionizer at 0 V, the shield at +1 V and the reflector at +100 V. If not specified in the text, these parameters were used. The count rate increases as the temperature rises, as shown in Fig. 3a. It suggests that the diffusion and desorption of the particles are enhanced due to the high temperature of the material surface. The count rate also increases as the voltage of the neutralizer target rises, as shown in Fig. 3b. These data imply that higher voltage attracts more ions, and also that ions that are not attracted are still present. Other parameter dependences shown in Figs. 3c and 4 include some difficult-to-grasp behaviors. One of the reasons for this could be the complex electric fields formed by a complex internal configuration. Another reason might be the energy dependence of the ion implantation. Some ions with energy around 1 keV do not adsorb on the surface of a material[8)]. It is possible that such circumstances make for further complicated conditions.

Assuming that all the events in a certain peak of the α spectrum are from ^{210}Fr, the ratio of the incident ^{210}Fr going into the converter to the ^{210}Fr leaving the converter is estimated at ~0.1% under the best of conditions. This conversion efficiency is quite low in comparison with the estimation in the pilot Rb experiment. In the Rb case, the conversion efficiency might be overrated because the measurement method of the Rb experiment was quite different from that of the Fr case. Furthermore, the principle of this ion-to-atom conversion is no problem for stable Rb isotopes, but could be a fatal problem for radioactive Fr isotopes, because of the time it takes to output from the converter after the cycles of ionization and neutralization.

Summary and plans

This project aimed to search for the violation of fundamental symmetries using Fr. A device to convert ions into atoms was developed to apply MOT to Fr produced as ions. However, the conversion efficiency of Fr was too low, and further improvements are needed for the implementation of MOT. Reducing the diameter of the ion entrance could lead to an increase in conversion efficiency. To realize this, the size of the ion beam spot must be minimized by improving the beam transportation. There should be still room for the optimization of the size and configuration of the whole device. Moreover, the materials of this device will be selected to have better ionization and neutralization efficiencies. A device that produces a fine atomic beam must be developed in order to apply Zeeman slowing and achieve an efficient MOT of Fr.

This work was carried out with part of “Training school on nuclear and particle physics experiments using accelerator beams” in the Support Program of KEK and Tohoku University. We gratefully acknowledge participants in the school for the ion beam transportation. Among them are Fuchiue Hiroyuki, Ishihara Yukiko, Miyamoto Takahiro, Nakajima Yujiro, Okano Toshihiro, Omika Shun-ichiro, Shimodate Tomoya, Yamazaki Tomohiro and Uchiyama Aiko. The authors would like to also thank the staffs of the CYRIC machine group. This work was supported by JSPS/MEXT KAKENHI Grant Numbers 21104405 and 23740166 and Tohoku University’s Focused Research Project.

References

1) Ginges J.S.M., Flambaum V.V., *Phys. Rep.* **397** (2004) 63.
2) Behr J.A., Cahn S.B., Dutta S.B., Ghosh A., Gwinner G., Holbrow C.H., Orozco L.A., Sprouse G.D., Urayama J., Xu F., *Nucl. Instrum. Meth.* A **351** (1994) 256.
3) Stancari G., Corradi L., Dainelli A., *Nucl. Instrum. Meth.* A **594** (2008) 321.
4) Dinneen T., Ghiorso A., Gould H., *Rev. Sci. Inst.* **67** (1996) 752.
5) Sato T. et al., *CYRIC Annual Report* 2010-2011 18.
6) Kawamura H. et al., *Nucl. Instrum. Meth.* B **317** (2013) 582.
7) Sato T. et al., *EPJ Web of Conf.* **66** (2014) 05019.
8) Brown F. and Davies J.A., *Can. J. Phys.* **41** (1963) 844.

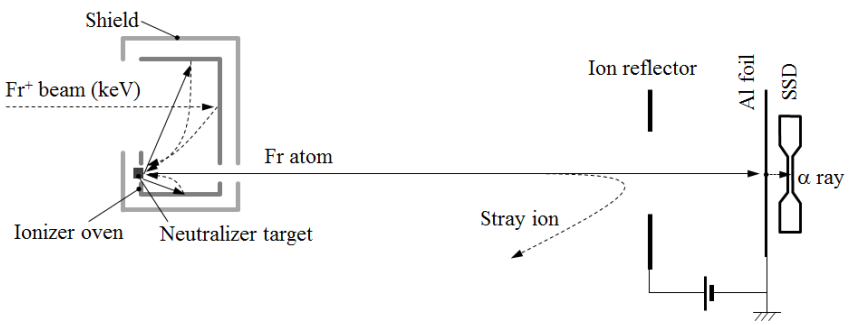

Figure 1. Schematic of the ion-to-atom converter and the detector based on SSD.

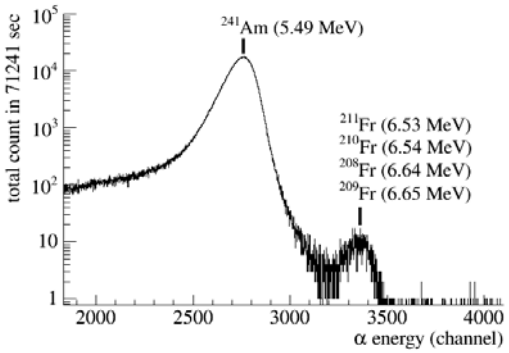

Figure 2. Total α spectrum acquired by the SSD after the ion-to-atom converter.

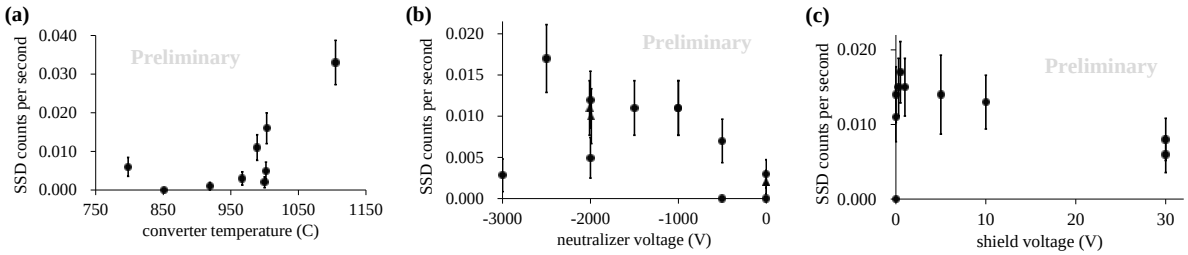

Figure 3. (a) Converter temperature dependence of the SSD count rate. (b) Neutralizer target voltage dependence. The shape of the plot indicates different runs under the same condition. (c) Shield voltage dependence of the SSD count rate. The shield voltage is used to confine ions to the oven. It looks like it has an optimum voltage.

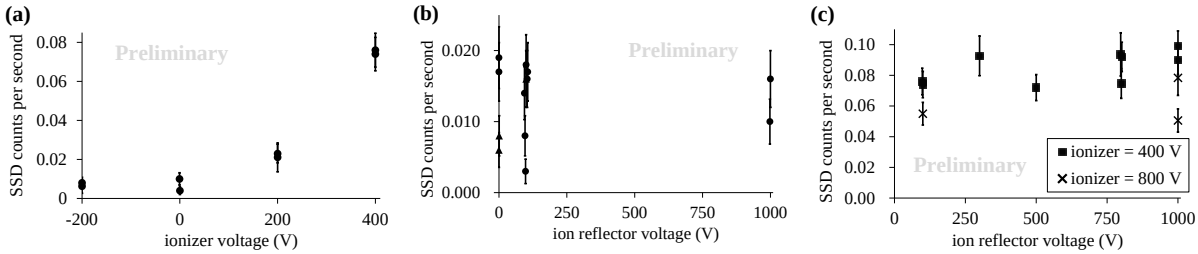

Figure 4. (a) Ionizer oven voltage dependence of the SSD count rate. This is an unexplained reaction. (b, c) Ion reflector voltage dependence. Ionizer dependence of (a) is difficult to understand. It might show that the output at higher ionizer voltages could include many charged components. However, from these figures, no significant dependence on the ion reflector is seen. This means that the dominant component must be electrically neutral.

I. 5. Neutralization of Radioactive Francium Atoms Using a Rotatable Yttrium Target

Kawamura H.[1,2], Aoki T.[2], Ando S.[2], Arikawa H.[2], Ezure S.[2], Harada K.[2], Hayamizu T.[2], Inoue T.[1,2], Ishikawa T.[2], Itoh M.[2], Kato K.[2], Uchiyama A.[2], and Sakemi Y.[2]

[1]*Frontier Research Institute for Interdisciplinary Sciences (FRIS), Tohoku University*
[2]*Cyclotron and Radioisotope Center, Tohoku University*

Magneto-optical trapping is one way to precisely measure the properties of francium. A yttrium target that can neutralize francium ions was developed for the magneto-optical trap. In this experiment, a signal that seems to be from the neutral francium atoms was obtained, although an accurate performance estimate was too difficult to accomplish.

Introduction

Francium (Fr), a radioactive element having no stable isotope, is a naturally occurring element that was only recently discovered[1)]. Consequently, the properties of Fr are understood very little, even now.

In order to study its properties, physical quantities are often measured by capturing Fr atoms in a magneto-optical trap (MOT). In the case of stable isotopes, researchers can usually produce an atomic beam and measure in flight. In the case of radioactive isotopes, by contrast, the particle density is too low to adequately measure because the number of atoms is very small. Trapping the atoms increases the number of atoms to be measured per unit time, thus allowing for adequate measurement.

Executing a MOT of Fr requires the neutralization of Fr ions. Our group produced Fr via the nuclear fusion reaction of an oxygen beam and a gold target, extracting positive ions by electrostatic fields. The ion must be converted to a neutral atom because the objective is to study the properties of neutral Fr. There are several methods to carry out this neutralization, such as a charge exchange with alkali vapor[2)] and a recombination with an electron[3)]. A thermal neutralization process at the metal surface is usually utilized for MOT[4)]. The particle desorbs with neutralization at the surface of the metal, having a smaller

work function than the ionization potential of the incident particle. A yttrium (Y) target is generally employed for Fr MOT[5]. The neutralization experiment with Fr ions was performed using the Y target.

Experiment

Magneto-optical trap

The experimental apparatus was developed by combining the Y target with a glass cell for MOT[6]. First, ions in the beam accumulated on the surface of the Y target for some time. Next, the target was rotated toward the glass cell and heated for thermal desorption. Finally, the neutralized atoms were captured via MOT inside the cell. The atoms originating in a rubidium ion beam were successfully trapped in the pilot experiment.

On the basis of achieving the Rb MOT, we tried to demonstrate the Fr trapping experiment. However, no signal seeming to originate from the Fr MOT was observed in this experiment.

Detection of the α particles

The experiment demonstrated the possibility that the number of Fr atoms from the neutralizer could be quite small. The paucity of the atoms is considered to be one of the reasons why the signal of Fr trapping was not observed. The glass cell was replaced with a solid state detector (SSD) for the particle identification by detecting the decay-α particles from Fr, as shown in Fig. 1. The relationship among the beam accumulation, Y target rotation, Y target heating, and SSD measurement is presented in Fig. 2.

Figure 3 shows the acquired α spectrum. The energy resolution was very poor due to the malfunction of a pre-amplifier for the SSD. Therefore, satisfactory particle identification was impossible. It is speculated from the original beam intensity that the large peak at ~2860 ch would correspond to the Fr isotopes with mass of 208-211.

The lifetime of this peak event was measured and can be seen in Fig. 4. The time constant derived from fitting roughly coincides with the lifetime of ^{210}Fr and ^{211}Fr.

The dependence of the detector count on the ion reflection voltage was investigated in Fig. 5. Since positive ions from the Y target will be swept out by applying positive voltage to the catcher, it is expected that the total count decreases and that the only component of the neutral atoms is measured unalterably. This behavior was roughly confirmed. However, quantitative interpretation is difficult. It is assumed that the ionized

particle desorbs from the Y surface with only thermal energy because no acceleration voltage is applied to it. If so, just 10 V exceeding the thermal energy could sweep out all the ions, meaning there should be no changes beyond that voltage. In reality, the detector count decreased gradually with the increase of the reflection voltage up to 100 V. The expected behavior did not occur due to the complex fields generated by a complex configuration around the detector. Additional information is necessary to judge whether the local decrease at 0 V originated simply from statistical error or was a significant change. Some of the particles could desorb with neither neutralization nor positive ionization, but with negative ionization instead[7].

Figure 6 shows the dependence of the count on the loading time of the ion beam. When the loading time is lengthened, the number of Fr accumulating on the Y target will increase with a decrease by radioactive decay. The loading time dependence was measured, and the result roughly corresponds to the prediction. Considering the increase of a background component on the Y, an optimum loading time must be maintained for efficient trapping.

Summary

We plan to perform the magneto-optical trapping in order to precisely evaluate the properties of Fr. An apparatus has been developed to convert Fr ions to neutral atoms and deliver the atoms to the MOT region. The experiment demonstrated Fr neutralization using this apparatus with a SSD. The apparatus met the minimal performance level and proved to emit the neutral component of radioactive isotopes looking like Fr. Still, detailed understanding will require more experiments. It is advantageous to study Fr in that the same method of particle identification can be employed for both an ion and an atom by detecting the decay-α particles. However, detailed experimental data are difficult to acquire because the machine time of our cyclotron is limited and may be not able to produce Fr. The quantitative evaluation of the neutralization will be achieved when a more reliable method of particle identification is employed for both an ion and an atom of stable Rb isotopes.

This work was carried out as part of “Training school on nuclear and particle physics experiments using accelerator beams” in the Support Program of KEK and Tohoku University. The authors gratefully acknowledge participants in the school, including Hasegawa Kunihiko, Hoshino Yukiko, Kitamura Noritaka, Kondo Gaku, Mizukami Atsushi, Ohashi Yuki, Takahashi Kenta, and Yamada Kohei. We also thank the organizers of the

school and the staffs of the CYRIC machine group. This work was supported by JSPS/MEXT KAKENHI Grant Numbers 21104005 and 25610112, and Tohoku University's Focused Research Project.

References

1) Scerri E., *Nature Chemistry* **1** (2009) 670.
2) Sell J.F., Gulyuz K., and Sprouse G.D., *Rev. Sci. Instrum.* **80** (2009) 123108.
3) Kawamura H. et al., *CYRIC Annual Report* 2010-2011 10.
4) Gwinner G., Behr J.A., Cahn S.B., Ghosh A., Orozco L.A., Sprouse G.D., Xu F., *Phys. Rev. Lett.* **72** (1994) 3795.
5) Simsarian J.E., Ghosh A., Gwinner G., Orozco L.A., Sprouse G.D., Voytas P.A., *Phys. Rev. Lett.* **76** (1996) 3522.
6) Aubin S., Gomez E., Orozco L.A., and Sprouse G.D., *Rev. Sci. Instrum.* **74** (2003) 4342.
7) Kawano H., Page F.M., *Int'l J. Mass Spectrom. Ion Phys.* **50** (1983) 1.

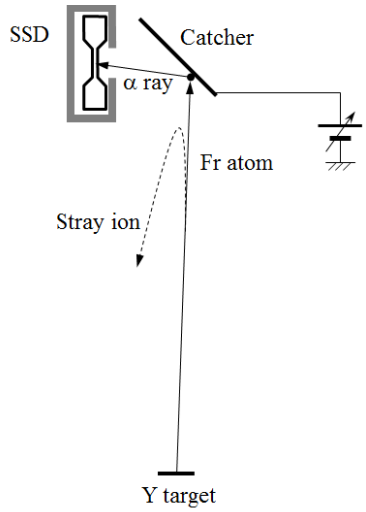

Figure 1. Schematic of the apparatus in the situation that the Y target rotates upward and heats up for the atomic desorption.

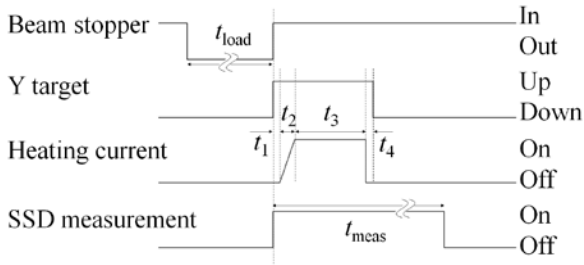

Figure 2. Time sequence of the measurement. The time periods t_1, t_2, t_3, t_4, and t_{meas} are fixed at 1, 2, 10, 1, and 300 sec, respectively. The loading time t_{load} is normally 50 sec except for the t_{load} dependence measurement.

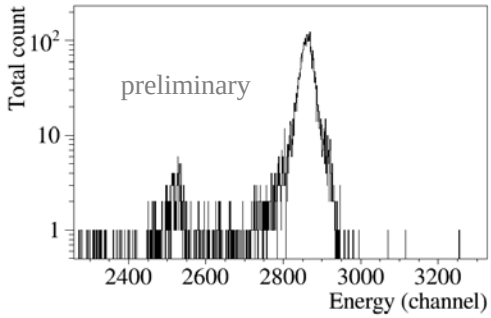

Figure 3. Total energy spectrum acquired during this experiment. The total measurement time is 16162 sec. The peaks at ~2860 ch and ~2530 ch are considered to originate from the Fr isotopes and their daughter nuclei, respectively.

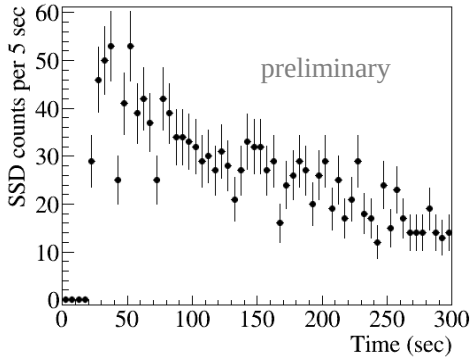

Figure 4. Total time spectrum. According to Fig. 2, the events start after the Y target heatup.

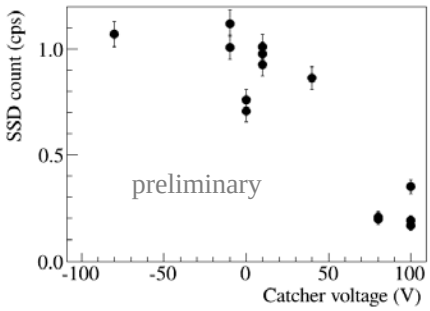

Figue 5. The dependence of the SSD count on the ion reflection voltage applying on the catcher.

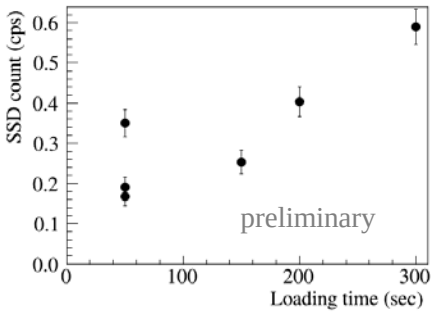

Figure 6. The dependence of the SSD count on the loading time t_{load}.

I. 6. Study of the Magneto-Optical Trap Using Rubidium with a Glass Cell*

Aoki T.[1], Ando S.[1],Arikawa H.[1], Ezure S.[1], Harada K.[1], Hayamizu T.[1], Inoue T.[1,2], Ishikawa T.[1], Itoh M.[1], Kato K.[1], Kawamura H.[1,2], Uchiyama A.[1], and Sakemi Y.[1]

[1]*Cyclotoron and Radioisotope Center, Tohoku University*
[2]*Frontier Research Institute for Interdisciplinary Sciences (FRIS), Tohoku University*

Our final goal is to measure the permanent electric dipole moment (EDM) which violates the time reversal symmetry directly. To trap francium (Fr) atoms in a magneto-optical trap (MOT) is a needed process in our plan of the search for the electron EDM[1)].

There are technical issues to trap Fr atoms in MOT. One of them is that the fluorescence from the trapped Fr atoms might be too weak to observe even if Fr was trapped in our setup. This issue requires the optimization of experimental parameters to observe a small number of trapped atoms. The optimization experiment prefers an element whose properties are well-known. Rubidium (Rb), which has stable isotopes, is easy to measure its atomic frequencies and to trap it. Moreover, Rb atoms can be used for the equipment development instead of Fr atoms because Rb has similar chemical properties to Fr.

The experimental setup is shown in Fig. 1. This experiment used ^{87}Rb. Since we concentrated on searching for the optimum parameters that are required for the observation of a small number of trapped Rb atoms by a CCD camera, Rb dispenser providing neutral Rb atoms stably was utilized. Thanks to the dispenser, the ion production, transportation, and neutralization are not required. The amount of supplying Rb atoms can be adjusted by applying current on the dispenser. A glass cell for MOT is made from quartz. Both inner and outer walls of this cell were originally coated with an anti-reflection coating. The inner wall was washed with what we call “piranha solution”

*Condensed from the article in Proceedings of 7th International Workshop on Fundamental Physics Using Atoms 2014 (FPUA2014)

and was coated with octadecyltrichlorosilane (OTS). OTS is used to prevent from sticking Rb atoms on the glass surface.

The trapped Rb atoms were observed by a CCD camera. The number N of trapped atoms is estimated by the following equation:

$$N = \frac{P}{\hbar\omega} \cdot \frac{1 + 6(I/I_s) + (2\delta/\gamma)^2}{6(I/I_s)(\gamma/2)} \cdot \frac{4R^2}{r^2}, \qquad (1)$$

where P is the intensity of fluorescence from trapped Rb atoms, $\hbar\omega$ is the energy of the fluorescence originating from trapped Rb atoms, I is the intensity of trapping laser per unit area, I_s is the saturation intensity per unit area, δ is a detuning of trapping laser, γ is a natural line width of $F = 3$ of $P_{3/2}$level, R is a distance between trapped area and a CCD camera lens, and r is a radius of a CCD camera lens. There are 6 trapping beams for MOT and this is the reason why we multiply I/I_s by 6. The image brightness was calibrated by reference laser and was converted to watt that is used for Equation (1).

The parameters of this experiment were the following: I/I_s=1.16, $\hbar\omega$=1.61 eV, δ=20 MHz, γ=6.06 MHz, R=50 mm, and r=25.4 mm. Using these parameters, the fluorescence originating from one atom was estimated at approximately 6.0 fW. The exposure time of the CCD camera was 500 ms and the applying current to the Rb dispenser was 3.5 A.

The photograph indicating the weakest fluorescence taken in this experiment is shown in Fig. 2. The brightness of this fluorescence was estimated at 6.5±0.60 fW. This value corresponds to the calculated value of the fluorescence from one Rb atom. We were able to observe the small number of trapped Rb atoms by a CCD camera.

This work was supported by Grants-in-Aid for Scientific Research (Nos. 21104005 and 25610112) and Tohoku University's Focused Research Project. We acknowledge Furumoto S. and the staffs of Division of Radiopharmaceutical Chemistry for help of the OTS coating.

References

1) Sakemi Y., et al., *J. Phys. Conf. Ser.* **302** (2011) 012051.
2) Mukherjee D., Sahoo B.K., Nataraj H.S., Das B.P., *J. Phys. Chem.* A **113** (2009) 12549.
3) Sandars P.G.H., *Phys. Lett.* **22** (1966) 290.
4) Nataraj H.S., Sahoo B.K., Das B.P., Mukherjee D., *Phys. Rev. Lett.* **101** (2008) 033002.
5) Simasarian J.E., et al., *Phys. Rev. Lett.* **76** (1996) 3522.
6) Ishikawa T., et al., *FPUA2014 proceedings*.

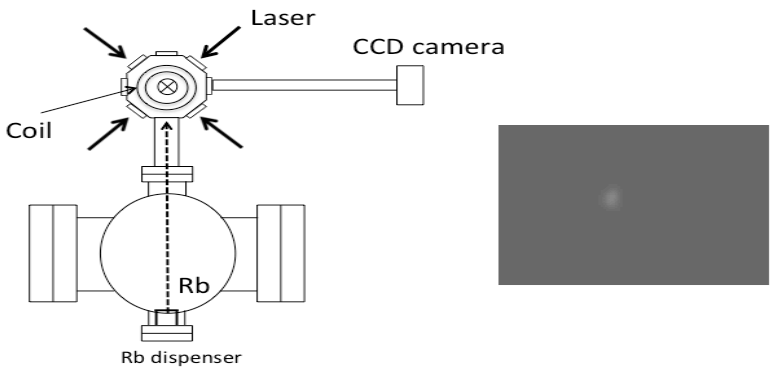

Figure 1. Experimental setup. This setup is used to neutralize ions and to trap neutral atoms[6]. The right figure is the photograph of the fluorescence from approximately 2000 Rb atoms captured by the CCD camera.

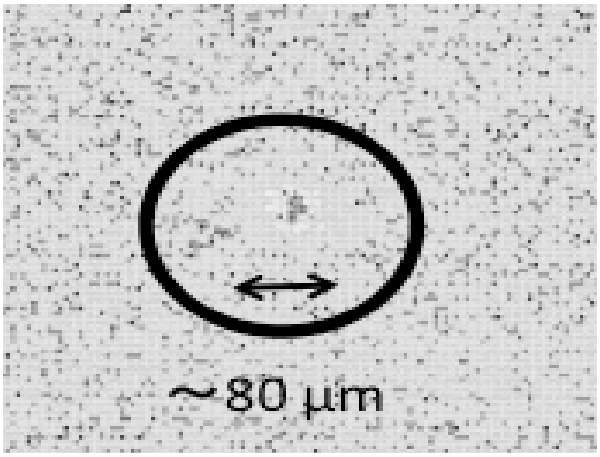

Figure 2. This photograph indicates the fluorescence corresponding to one Rb atom. The Rb atoms should be trapped in the area surrounded by a circle.

I. 7. Progress in Development of a Francium Atomic Beam: towards a Measurement of an Electron EDM

Sato T.[1], Arikawa H.[2], Ezure S.[2], Harada K.[2], Hayamizu T.[2], Inoue T.[2], Ishikawa T.[2], Itoh M.[2], Kato T.[2], Kawamura H.[2], and Sakemi Y.[2]

[1]*Department of Physics, Tokyo Institute of Technology*
[2]*Cyclotron and Radioisotope Center, Tohoku University*

An electric dipole moment (EDM) is a non-trivial distribution of the electric charge in the non-degenerate system of elementary particles. A non-zero EDM of an elementary particle violates time reversal symmetry, and hence CP-symmetry, which is necessary to explain the evolution mechanism of this matter dominated universe. The EDM is one of the most promising candidates to search for the physics beyond the Standard Model (SM), because the almost all contributions for the predicted finite value of the EDM come from the physics beyond the SM due to the small contribution from the SM.

The final objective of our project is to search for the electron EDM (e-EDM) using an enhancement mechanism of e-EDM in a paramagnetic atomic system, the francium (Fr, Z=82) which is the heaviest alkali element and has the e-EDM enhancement factor of approximately 895[1)]. Final sensitivity for the e-EDM in this project is expected as $|d_e| \sim 10^{-28}$ e·cm, which is approximately an order of magnitude smaller than the current experimental e-EDM limit in the atomic system obtained in Tl experiment with $|d_e| \sim 10^{-27}$ e·cm[2)].

In this project, ^{210}Fr is produced as a keV energetic ion beam by the fusion reaction of ^{18}O + ^{197}Au in a thermal ionizer[3)], and then the Fr ions are transported to a neutralizer[4)]. After the neutralization, the Fr atoms will be slowed down by a Zeeman slower, and then introduced to a magneto-optical trap (MOT) in order to cool down to the milli-kelvin temperature[5)], which is necessary to transport to a final optical trap used for the EDM measurement[6)] with high loading and trapping efficiency. In this scheme, there is a concern about the loss of the Fr atoms in the Zeeman slower tube due to the divergence of the beam. In order to reduce the loss of the atoms during the cooling scheme, a cooling of the

transverse velocity of the beam can be adopted. Here, a design of the apparatus for the transverse cooling of the atomic beam is discussed.

The neutralizer enables us to convert the keV ion beam to the thermal neutral atomic beam. The divergence of the atomic beam is approximately 100 mrad, on the other hand, the acceptance of the Zeeman slower is typicaly about 1 mrad. Consequently, the transport efficiency from the neutralizer to the MOT is limited as approximately 0.8%. The beam divergence comes from the transverse velocity of the beam; thus, a decrease of the transverse velocity causes a decrease of the beam divergence.

The transverse cooling has been applied to metastable He[7], Rb[8], metastable Ar[9] and other atoms. The cooling of the transverse component of the velocity is realized by the pressure force from laser lights. When the two counter-propagating laser lights irradiate the moving atom, the atom feels the asymmetric pressure force from the laser light because the difference of the absorption probability of the light due to the Doppler shift of the absorption line. As a result, in the case of irradiation of red shift light, the atom feels the force opposite to the direction of the motion; thus, the atomic beam is collimated. In order to cool down hot Fr atoms effectively, the cooling laser light tuned near the resonance of the D2 transition of Fr is reflected many times typically up to ~100 between a pair of the mirrors as shown in Fig. 1. Moreover, to correct the difference of the Doppler shift corresponding to the transverse velocity of the atom, two mirrors are set as slightly non-parallel[7]. The two-dimensional collimating is realized with the use of two pairs of the mirrors.

In order to study the design for an efficient cooling, a Monte-Carlo simulation of the transverse cooling was performed[10]. The setup in the simulation is shown in Fig. 2. Each particle was produced on the surface of the neutralization target of the neutralizer. The initial position of the particle was randomized in the diameter of the 2 mm corresponding to the realistic shape of the neutralization target. The initial velocity distribution of the particle obeyed to the thermal Boltzmann distribution of 1000 ^{o}C. Atoms whose velocities were over 400 m/s were ignored, because of the limit of the cooling velocity of 2 m length Zeeman slower. Three-dimensional components of the velocity of the atoms were randomized. Only the particles which go through the extraction hole of the neutralizer were used for the estimation of the transport efficiency. After the neutralizer, the two-dimensional transverse cooling was performed. For the pressure force of the laser light, the Lorentz-type force was used. The equation of the motion of the particle was solved by the 4th order of the Runge-Kutta method. After the transverse cooling, a two-dimensional optical molasses was

applied in order to match the atomic beam axis to the Zeeman slower axis[7]. After the optical molasses, two chambers for the differential pumping and the Zeeman slower were considered. In this simulation, these were treated as simple beam collimators. The particle which reached the area of the diameter of 30 mm were used for the numerator of the efficiency calculation.

In order to determine the optimum length of the mirror, the mirror length dependence of the transport efficiency was studied. The result of the simulation is shown in Fig. 3. The initial laser angle and mirror tilt were optimized for each mirror length. The transport efficiency was improved as an increase of the mirror length. However, the region over 400 mm, the efficiency was saturated. In practice, considering the difficulty of making a huge size mirror, the 400 mm mirror was appropriate.

In order to study about the requirement for the apparatus, the transport efficiency dependence of the laser and mirror condition was calculated. Figure 4 shows the laser detuning, initial laser angle and mirror tilt dependence of the transport efficiency at the mirror length of the 400 mm. For the laser detuning, the positive detuning was suitable because the laser irradiation with too small initial laser angle is practically difficult. For the mirror tilt, the change of the 0.5 mrad mirror tilt caused the decrease of the approximately 3% of the transport efficiency. The mirror adjustment system should have 0.1 mrad accuracy.

Based on this simulation works, the construction of the transverse cooling is in progress. In the first step, the test experiment using Rb atoms whose chemical properties are similar to the Fr will be performed. The transverse cooling will be installed in the Fr production and transport beam line.

References

1) Mukherjee D., Sahoo B. K., Nataraj H. S., Das B. P., *J. Phys. Chem.* A **113** (2009) 12549.
2) Regan B. C., Commins E. D., Schmidt C. J., DeMille D., *Phys. Rev. Lett.* **88** (2002) 071805.
3) Arikawa H. et al.,*CYRIC Annual Report* 2012-2013 (this report).
4) Kawamura H. et al., *CYRIC Annual Report* 2012-2013 (this report).
5) Aoki T. et al., *CYRIC Annual Report* 2012-2013 (this report).
6) Hayamizu T. et al., *CYRIC Annual Report* 2012-2013 (this report).
7) Rooijakkers W., Hogervorst W., Vassen W., *Opt. Comm.* **123** (1996) 321.
8) Slowe C., Vernac L., Hau L. V., *Rev. Sci. Instrum.* **76** (2005) 103101.
9) Welte J. et al., *New J. Phys.* **12** (2010) 065031.
10) Sato T., "Development of a Francium Atomic Beam Honyarara Hogehoge (in Japanese)", Master thesis, Tohoku University (2013).

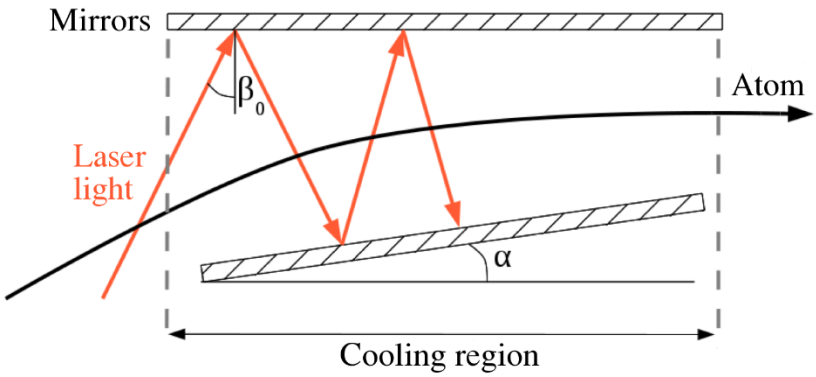

Figure 1. Schematic view of a transverse cooling. α is a mirror tilt angle and β_0 is a initial angle of incidence of the laser light.

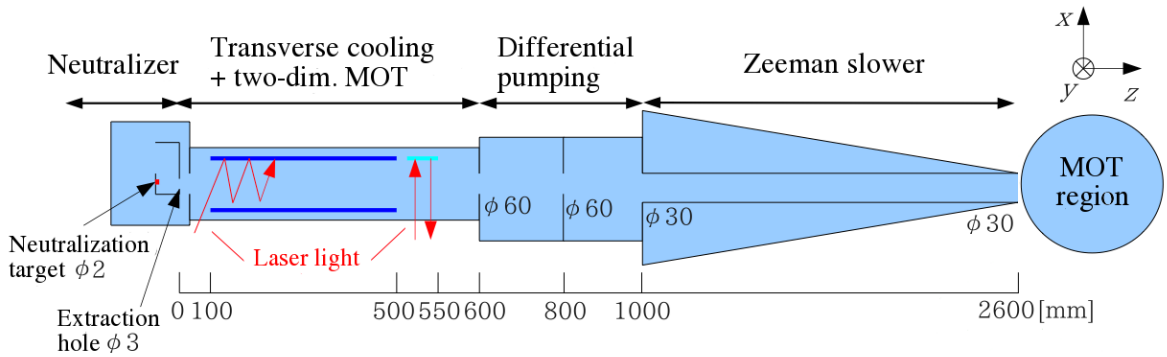

Figure 2. Setup of the simulation of the transverse cooling.

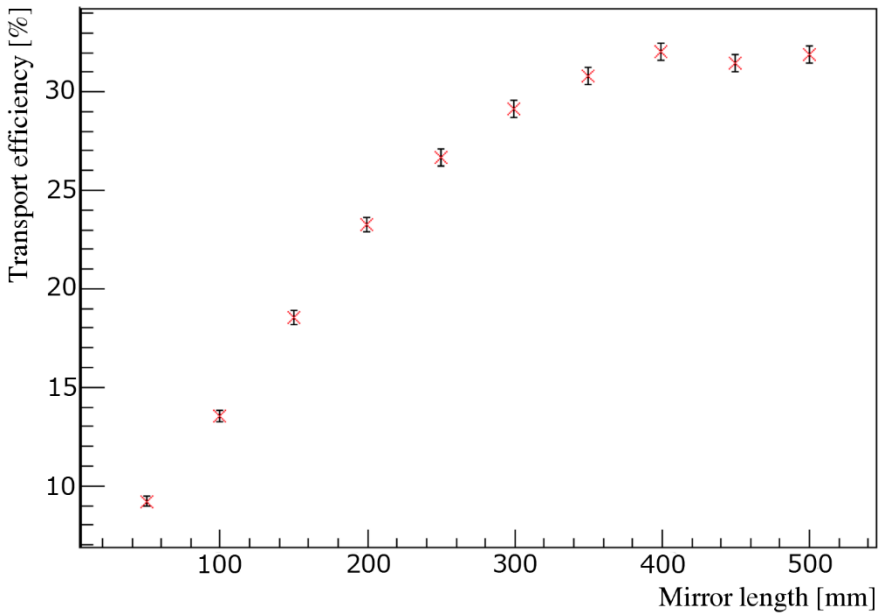

Figure 3. Mirror length dependence of the transport efficiency.

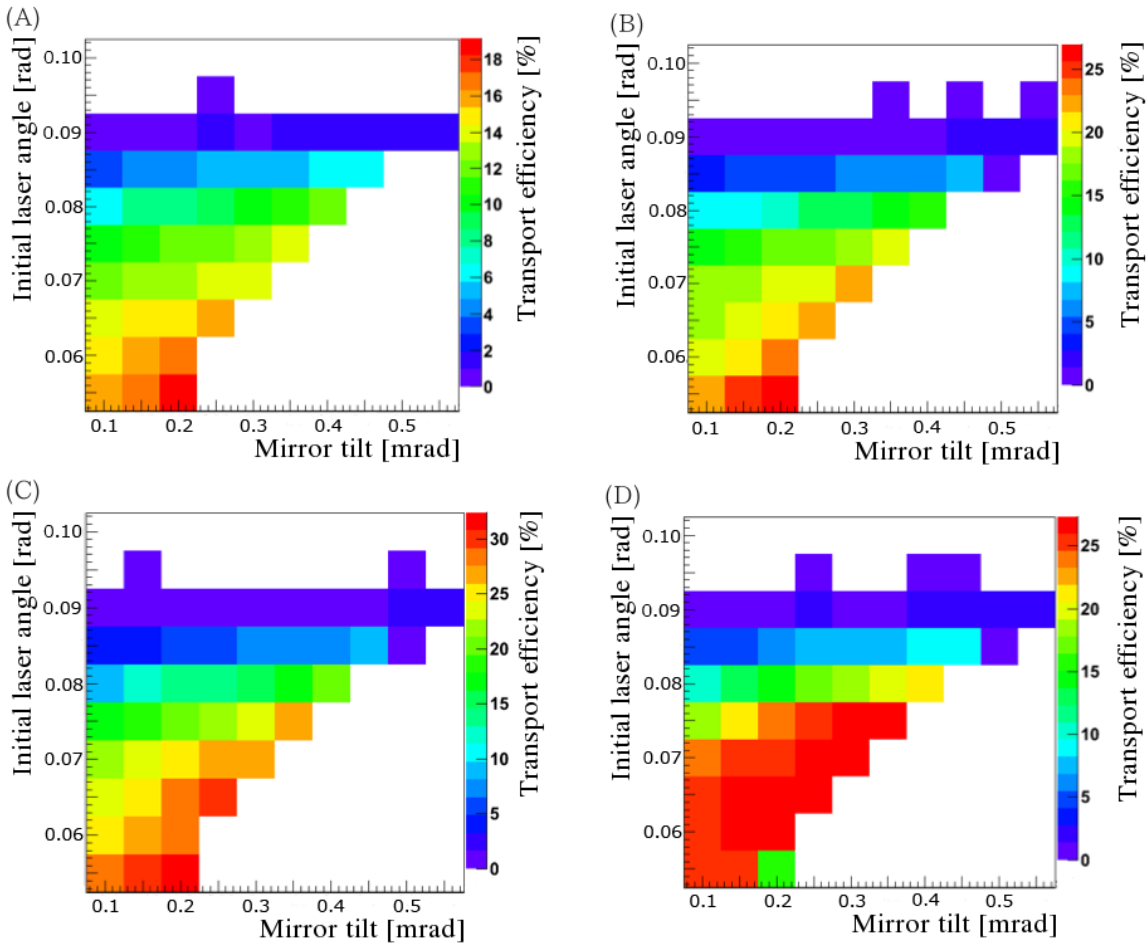

Figure 4. Laser detuning, initial laser angle and mirror tilt dependence of the transport efficiency. (A) -5 MHz, (B) 0 MHz, (C) 5 MHz and (D) 10 MHz detuning.

I. 8. Present Status of the Magneto-Optical Trap System for Trapping Rare Radioactive Francium Atoms

Harada K.[1], Ezure S.[1], Kato K.[1], Hayamizu T.[1], Kawamura H.[1,2], Inoue T.[1,2], Arikawa H.[1], Ishikawa T.[1], Aoki T.[1], Uchiyama A.[1], Itoh M.[1], Ando S.[1], Aoki T.[3], and Sakemi Y.[1]

[1]*Cyclotron and Radioisotope Center, Tohoku University*
[2]*Frontier Research Institute for Interdisciplinary Sciences, Tohoku University*
[3]*Graduate School of Arts and Sciences, University of Tokyo*

It is widely recognized that the nuclear spin independent atomic parity nonconservation (APNC)[1)] provides the signature of parity-reversal (P) violation and the permanent electric dipole moment (EDM)[2)] provides the signature of simultaneous violation of P and time-reversal (T). They are sensitive tools for exploring the new physics beyond the standard model of elementary particles. Although the signals induced by these effects are extremely small, several theories predict that both signals are enhanced by total number of protons Z in an atom due to the large effective electric field and are proportional to Z^3.

The electron EDM (eEDM) measurement using thorium monoxide (ThO) molecules[2)] is well known as the most precise measurement. The upper limit of eEDM obtained from the experiment is 8.7×10^{-29} $e$cm. The interaction time between ThO molecules and the external electric field applied by the plates whose length is about 22 cm is almost 2 ms due to the effect of buffer gas cooling technique. The greatest benefit of the experiments using ThO molecules is that the internal effective electric field E_{eff} can be much higher than that in atoms. However, in the atomic or molecular beam experiment the significant systematic effects are caused by the motional magnetic field and by the geometric phase shifts generated by complicated field gradients. These systematic errors mimic the true EDM signal and limit the accuracy of measurement of atomic EDM.

Neutral francium (Fr), being the heaviest alkali atom (Z = 87), trapped by laser lights is one of the best candidates for investigating the violation of fundamental symmetries. The APNC signal in Fr atom is 18 times larger than that of the cesium atom[3)] and the enhancement factor of Fr atom for eEDM is 895[4)]. Moreover, the velocity of atoms is drastically low when they are laser cooled and trapped. Therefore, the systematic errors

are strongly suppressed and the interaction time is elongated to a few seconds, which is much longer than that of the conventional atomic and molecular beam experiments. Thus, there are several advantages of using optically cooled and trapped Fr atoms for the measurements.

We report the current status of the experimental apparatus for trapping Fr and rubidium (Rb) atoms at Cyclotron and Radioisotope Center (CYRIC), Tohoku University. As Rb has similar chemical properties to that of Fr and is a stable atom, we utilized Rb for the alignment of entire experimental setup. In the laser experimental room (Lab A), we have developed the laser light sources and its frequency stabilization for magneto-optical traps (MOT) of Fr and Rb atoms are performed[5]. We use an external cavity laser diode tuned to the $5S_{1/2} \rightarrow 5P_{3/2}$ D2 transition for the trapping light of ^{87}Rb atom. The frequency stabilization for Rb MOT is performed by the frequency modulation spectroscopy using Rb reference cell. On the other hand, as a trapping light source for ^{210}Fr, we employed a single frequency Ti:Sapphire laser light source, tuned to the $7S_{1/2} \rightarrow 7P_{3/2}$ D2 transition of the Fr atom at 718 nm. We use iodine molecules for the frequency stabilization and monitor of Fr MOT as there are no stable isotopes of Fr. We have also developed the double Rb MOT system to investigate the characteristics of loading and decay of atoms in MOT. The investigation is essential to transport rear radioactive atoms efficiently and rapidly to an ultrahigh vacuum region for the APNC and eEDM measurements. Further, we have observed the fluorescence from a single Rb atom trapped in MOT using the lens system composed by four spherical lenses because the probability of getting large number of Fr atoms for being trapped in MOT is less at first. Also an optical dipole trap (ODT) experiment using Rb atoms for the pilot studies of the measurements has been achieved[6]. A lot of apparatus and techniques described above have been developed.

In the Lab B, which is in the radiation controlled area, we have constructed MOT system with the neutralizer of yttrium (Y) for Fr and Rb ions as they are transported through the beamline as ions from the production area[5]. The detailed setup is shown in Fig. 1. Optical fibers whose length is 150 m are laid between the Lab A and the Lab B, which transports the laser lights. We performed MOT experiment using Rb atoms before trying it out for Fr atoms. The number of Rb ions coming from the production area was 9.4×10^{10} ions/s. The number of atoms trapped was estimated to be 10^6 (inset, Fig. 1). The fluorescence from neutralized Rb atoms trapped in MOT has been successfully observed using this system.

We have developed the laser light sources, the frequency stabilization system and

the MOT system for trapping Fr atoms at the 51 course beamline. We then would like to observe the fluorescence from Fr atoms trapped in MOT. After optimization of Fr MOT, especially the number of atoms, we will perform an ODT experiment, and then APNC and EDM measurements using cold Fr atoms.

References

1) P. A. Vetter, et al., Phys. *Rev. Lett*. **74** (1995) 2658.
2) The ACME Collaboration, J. Baron *et al.*, *Science* **343** (2014) 269.
3) V. A. Dzuba, et al., *Phys. Rev.* A **51** (1995) 3454.
4) D. Mukherjee, et al., *Phys. Chem.* A **113** (2009) 12549.
5) K. Harada, et al., *Proc. Conf.* ARIS2014 (to be submitted).
6) T. Hayamizu, et al., *JPS Conf. Proc.* **1** (2014) 013065.

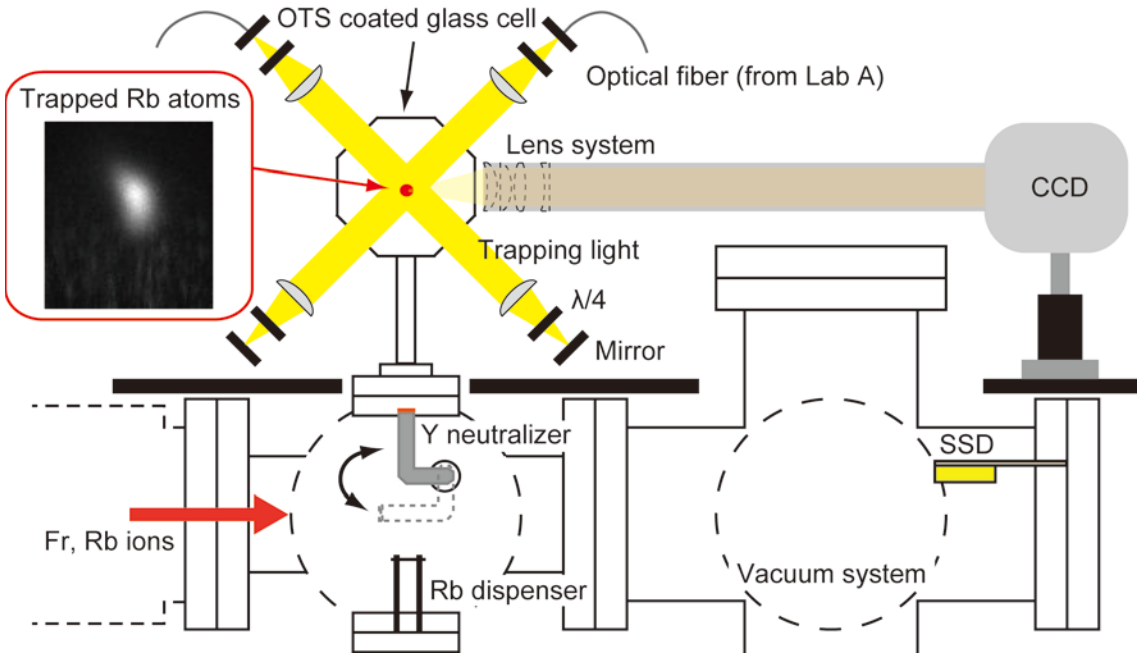

Figure 1. Experimental setup in the lab B. The optical fibers of 150 m length are laid between the labs to carry the laser lights. The laser lights which are exchanged between 718 nm and 780 nm wavelengths by a flipper mirror were transported to the lab B for trapping Fr or Rb atoms. Inset: Photograph of the fluorescence from Rb atoms trapped in MOT.

I. 9. Light Induced Desorption of Alkali Atoms from OTS Coated Cell for the Electron Electric Dipole Moment Search

Kato K.[1], Harada K.[1], Ezure S.[1], Kawamura H.[1,2], Inoue T.[1,2],Hayamizu T.[1], Arikawa H.[1], Ishikawa T.[1], Uchiyama A.[1], Aoki T.[1], Mariotti E.[3], Hatakeyama A.[4], Itoh M.[1], Ando S.[1], and Sakemi Y.[1]

[1]*Cyclotron and Radioisotope Center (CYRIC), Tohoku University*
[2]*Frontier Research Institute for Interdisciplinary Sciences (FRIS), Tohoku University*
[3]*CNISM and Physics Department, University of Siena*
[4]*Department of Applied Physics, Tokyo University of Agriculture and Technology*

The nonzero value of eEDM provides the direct signature for the violation of CP, where C and P represent charge conjugation and parity symmetry, respectively, under CPT conservation. It is an important clue for understanding the mechanism of the matter-antimatter asymmetry in the universe. As the values of eEDM predicted by several theoretical models such as supersymmetry model etc. are quite small, a lot of experimental techniques based on a laser cooling of atoms or a buffer gas cooling of molecules have been proposed and performed for the precise measurement of the signal yielded by eEDM[1)].

Francium (Fr) atom, which is the heaviest alkali atom, is one of the strong candidates for the eEDM search because the large electric filed produced by the nucleus increases the sensitivity of the measurement by a factor of about 895[2)]. The eEDM experiment using laser cooling and trapping techniques of Fr atom has a potential for improving the sensitivity of that performed by ThO[1)]. However, Fr is a radioactive atom, and the cyclotron operation is required for its production. Therefore, it is a major challenge to increase the number of Fr atoms captured by laser lights and to reduce the statistics error.

In the glass cell, most of Fr atoms are adsorbed on the surface of glass and not trapped by laser lights. Light-induced atomic desorption (LIAD) is one of the useful techniques to desorb these atoms. When atoms on the surface are irradiated by lights, these atoms are desorbed from the surface. This is capable of increasing the number of trapped atoms. Inner wall of the Pyrex glass cell is coated with octadecyltrichlorosilane (OTS) which is one of the dryfilms. OTS reduces the strength of the interaction between the alkali vapor and the Pyrex glass[3)]. Test experiment of LIAD using rubidium (Rb) from OTS

coated glass has been performed at CYRIC. Rb is one of the alkali metal atoms, and its chemical property is similar to that of Fr.

The experimental apparatus is depicted in Fig. 1. The Rb dispenser is located under the neutralizer to supply Rb atoms inside the OTS coated glass cell. MOT is formed by three pairs of counterpropagating laser lights and the quadrupole magnetic field. The number of atoms trapped in MOT is detected by a CCD camera. To confirm the effect of LIAD, we use white flash light (430EX II, Canon) which is fixed above the MOT glass cell. The flash light from the device is emitted to the MOT glass cell and the desorbing effect from the OTS coated cell is observed.

The signal of LIAD is shown in Fig. 6. The vertical axis is the intensity of the trap area which is detected by the CCD camera, and the horizontal axis is time. The number of trapped atoms at t = 180 s is 103. The intensities of the steep peaks after t = 180 s gradually decreased. This indicates that the number of desorbed atoms on the surface of OTS coated glass cell reduced due to the LIAD effect.

This result is expected to be applied for increasing the number of trapped Fr atoms. We will investigate the photon energy dependence for the LIAD effects. We will confirm LIAD effect from yttrium surface which neutralizes Fr and Rb ions beam.

References

1) The ACME Collaboration, et al., *Science* **343** (2014) 269.
2) Mukherjee D, et al., *J Phys Chem* **A 113** (2009) 12549.
3) M. Stephens, et al., *J Appl Phys* **76** (1994) 3479.

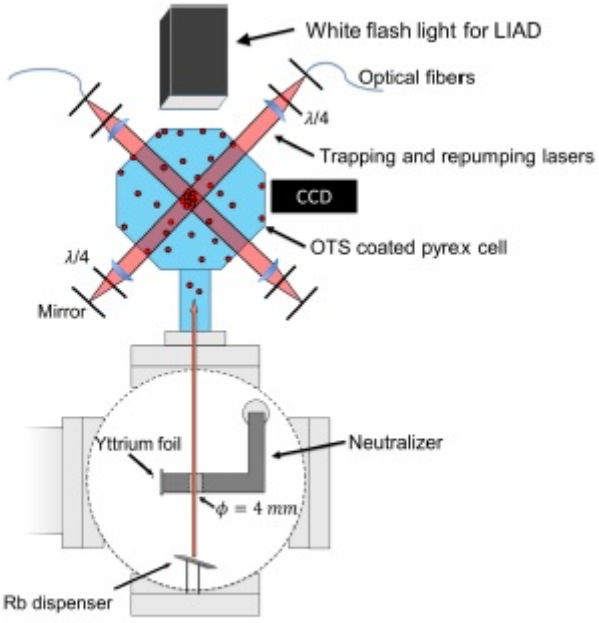

Figure 1. Setup of LIAD experiment.

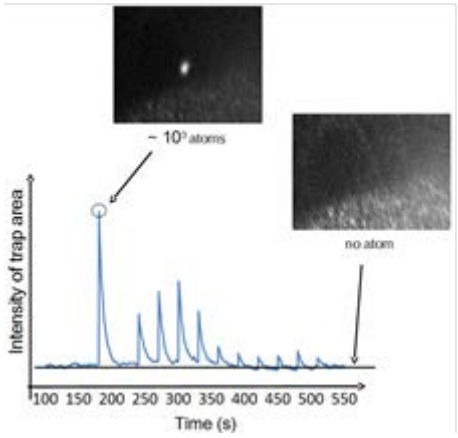

Figure 2. LIAD from OTS coated Pyrex cell.

I. 10. Development of an Optical Dipole Trap System for the Electron Electric Dipole Moment Search

Hayamizu T.[1], Harada K.[1], Ezure S.[1], Kato K.[1], Aoki T.[2], Inoue T.[1,3], Itoh M.[1], Kawamura H.[1,3], Ando S.[1], Aoki T.[1], Arikawa H.[1], Ishikawa T.[1], Uchiyama A.[1], and Sakemi Y.[1],

[1]Cyclotron and Radioisotope Center, Tohoku University
[2]Graduate school of Arts and Sciences, The University of Tokyo
[3]Frontier Research Institute for Interdisciplinary Sciences, Tohoku University

Ultracold atoms captured by laser cooling and trapping techniques are used for optimizing the measurement precision for a permanent electric dipole moment (EDM) in an elementary particle[1,2]. In the case of alkali atoms, the EDM signal from the valence electron is enhanced by the large effective electric field from the nucleus in an atom[3,4]. Francium (Fr, Z = 87), which is the heaviest alkali atom, exhibits a large enhancement factor of 895 for an electron EDM[5], but all isotopes are unstable.

At Cyclotron and Radioisotope Center (CYRIC) at Tohoku University, Fr atoms will be captured in an optical dipole trap (ODT)[6] by laser-cooling and trapping techniques in order to reduce statistical and systematic errors in the EDM measurement. Fr is produced via the nuclear fusion reaction of ^{197}Au(^{18}O, xn)$^{215-x}$Fr with an oxygen beam (E_{18O} = 100 MeV) accelerated from an AVF cyclotron into a gold target. The produced Fr is transported as an ion beam and converted to a neutral atom by a neutralizer. The atom is captured in a magneto-optical trap (MOT)[7], which consists of a 3-dimensional laser cooling and a quadrupole magnetic field, as a cold atomic cloud with a temperature of a few hundred μK. The captured atoms in the MOT are situated in the ODT and moved into a magnetically-shielded area via optical tweezers. The EDM search will be performed by applying electric and magnetic fields to the atomic cloud captured in the ODT. Each apparatus for the EDM measurement has been developed using Fr or rubidium (Rb) atoms.

An ODT is a technique involving a high-intensity, strong-focusing laser light detuned largely from the resonant frequency of the atom. A trap potential depth, as shaped at the focal point, is proportional to the intensity of the trapping laser light. The ODT does

not exert a cooling effect for trapped atoms. The MOT and polarization gradient cooling (PGC)[8] are often used as pre-cooling methods before loading into the ODT. The ODT will be used to hold and transport ultracold atoms into the magnetically-shielded area, and also to keep them during the EDM measurement in the experiment at CYRIC.

We reported a red-detuned ODT experiment with a 1083 nm fiber laser (Keopsys KPSBT2-YFL-1083-50-COL)[9], and the development of an offline double MOT system using ^{87}Rb atoms[10]. The experimental setup for the ODT experiment is shown in Fig. 1. First, Rb atoms were stored in the second MOT chamber. We then applied the PGC technique for pre-cooling by turning off the MOT coil current and detuning the trapping light frequency. After the loading into the ODT for 1 s was performed by overlapping the ODT light in the region of the second MOT, the MOT light was turned off. The ODT laser with a diameter of 1 cm and a wavelength of 1083 nm was focused through an f = 250 mm achromatic spherical focal lens. The trapped atoms in the ODT were finally isolated for 5 ms. The trapped atoms in the ODT were observed as an absorption image by using a CCD camera after the ODT trapping light was turned off.

As a result, the absorption image of the atoms trapped in the ODT was confirmed. The shape of the trapped atoms in the ODT is shown in Fig. 2. The number of atoms was estimated from a transmittance distribution of the imaging light through the atomic cloud. The trapped number was 3×10^3 [9]. The improvement in both the pre-cooling process and the ODT light alignment process are required to increase the number of atoms.

This research was mainly supported by Grant-in-Aid for Scientific Research Nos. 21104005 and 25・10612 from MEXT/JSPS. One of the authors (HT) gratefully acknowledges the support of JSPS Research Fellowships for Young Scientists.

References

1) Parker RH, et al., *Phys Rev* C **86** (2012) 065503.
2) Zhu K, et al., *Phys Rev Lett* **111** (2013) 243006.
3) Sandars PGH, *Phys Lett* **14** (1965) 194.
4) Sandars PGH, *Phys Lett* **22** (1966) 290.
5) Mukherjee D, et al., J *Phys Chem* A **113** (2009) 12549.
6) Chu S, et al., *Phys Rev Lett* **57** (1986) 314.
7) Raab EL, et al., *Phys Rev Lett* **59** (1987) 2631.
8) Dalibard J, Cohen-Tannoudji C, *J Opt Soc Am* B **6** (1989) 2023.
9) Hayamizu T, et al., *Proc of 7th Int Conf Fundament Phys Using Atoms (FPUA2014)*, accepted.
10) Harada K, et al., *CYRIC Annual Report 2010-2011* (2012) 14.

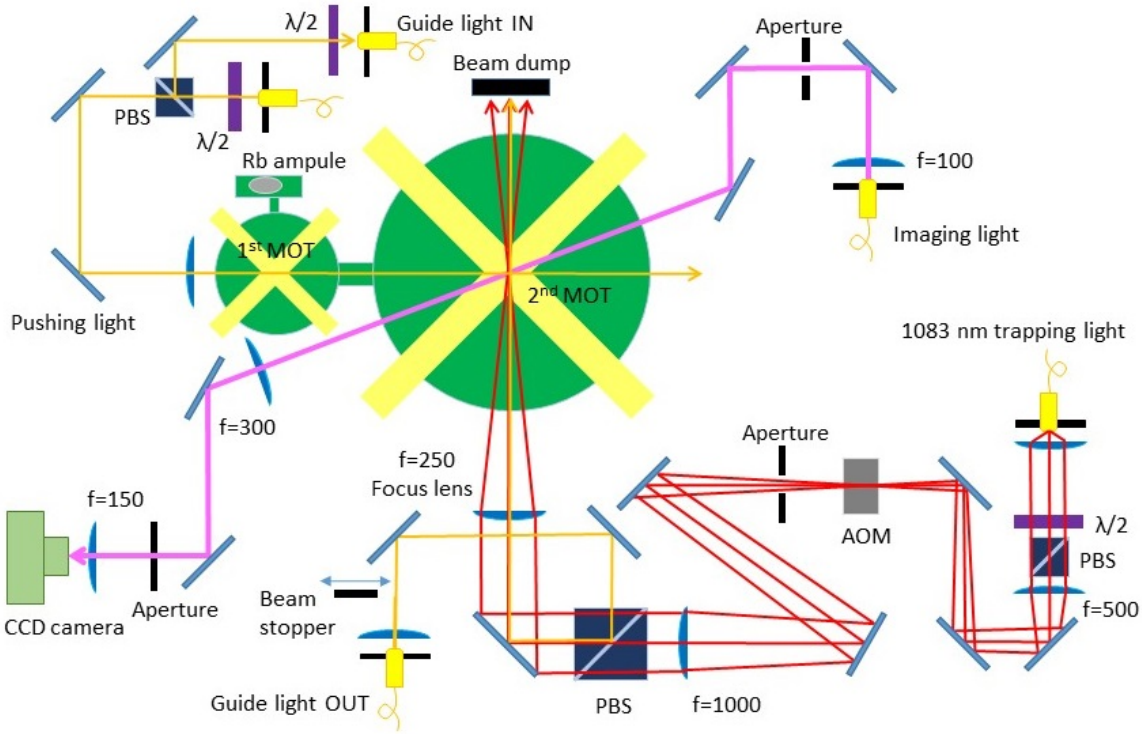

Figure 1. Overview of setup for the ODT experiment around the double-MOT system.

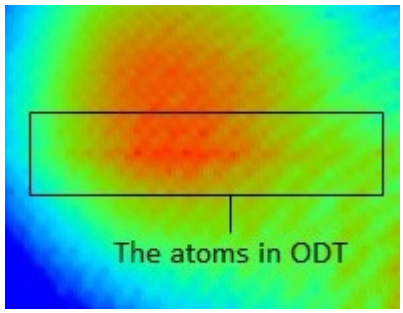

Figure 2. A picture showing an ODT existent. This picture was obtained by comparing two pictures which were taken at the same timing of the differential sequences. One was taken when the ODT trapping light was turned on, and the other was taken when the light was turned off. A different degree of absorption between the two pictures is described as a color distribution. A horizontally long and thin red shape in a black cage is an existence of the trapped atoms in the ODT.

I. 11. Training School on Nuclear and Particle Physics Experiments Using Accelerator Beams

Inoue T.[1], Sakemi Y.[1], Wakui T.[1], Itoh M.[1], Harada K.[1], Shimada K.[1], Kawamura H.[1,2], Hayamizu T.[1], Kato T.[1], Sato T.[1], Takahasi M.[1], Ezure S.[1], Ando S.[1], Arikawa H.[1], Ishikawa T.[1], Kato K.[1], Aoki T.[1], Kaneda M.[3], and Tamura H.[2]

[1]*Cyclotron and Radioisotope Center, Tohoku University*
[2]*Frontier Research Institute for Interdisciplinary Science, Tohoku University*
[3]*Department of Physics, Tohoku University*

1st and 2nd “Training school on nuclear and particle physics experiments using accelerator beams” (SCHOOL) in the Support Program of KEK and Tohoku University were held at CYRIC from February 26th through March 2nd and December 23rd through December 27th in 2013. The purpose of this school is the support of the human resources development for the Japanese accelerator science by training undergraduates, who are interested in accelerator science such as the nuclear, elementary particle physics or the beam physics, and the experiments using the accelerator beam. The participating students came widely from the universities of the whole country, as listed in Table 1.

In SCHOOL, the francium (Fr), which is a radioactive element, was produced through the nuclear reaction with the $^{18}O^{5+}$ primary beam accelerated by an AVF cyclotron and ^{197}Au target, as $^{18}O + {}^{197}Au \rightarrow {}^{215-x}Fr + xn$. The students experienced the processes of the nuclear experiment using the accelerator through the measurement of the decay energy and the life time of the produced Fr nucleus by using the solid state detector (SSD). In addition to this online experiment, the offline experiment by using the americium sealed radioactive source was performed to understand the operating principles of the SSD. When the students toured CYRIC, they asked many questions with strong interests. At the end of SCHOOL, the students had the presentation and discussion of the training contents. Since the students were very active, the bright future of the Japanese accelerator science is expected.

The authors would like to thank the staff of CYRIC machine group. This SCHOOL will be held every year.

Table 1. Distribution of students for 1st and 2nd “Training school on nuclear and particle physics experiments using accelerator beams”.

University	Department	Number	
		1st school	2nd school
Nara Women’s University	Physics	1	0
Kanazawa University	Physics	1	0
Hiroshima University	Physics	1	0
Tohoku University	Medicine	1	0
	Physics	0	1
Saitama University	Physics	1	0
Ritsumeikan University	Physics	1	0
Waseda University	Physics	1	1
International Christian University	Physics	1	0
Rikkyo University	Physics	0	1
Tokyo Institute of Technology	Chemistry	0	1
Kyusyu University	Physics	0	1
Okayama University of Science	Physics	0	1
Tokyo University of Science	Physics	0	1

I. 12. Single Event Gate Rupture Detection Experiment in SiC MOS Capacitors at CYRIC

Makino T.[1], Deki M.[1], Ohshima T.[1], Wakui T.[2], and Sakemi Y.[2]

[1]Japan Atomic Energy Agency
[2]CYRIC Tohoku University

The catastrophic failure in Metal-Oxide-Semiconductor (MOS) devices induced by the ions incidence is known as Single Event Gate Rupture (SEGR). The issue of SEGR arises in MOS power devices for not only space but also terrestrial applications led by neutrons created by cosmic rays even on the ground. Silicon Carbide (SiC) is a promising wide-band-gap semiconductor for electronic devices. However, SEGR in SiC MOS devices has not yet been fully understood. It is expected that the provability of SEGR might increase with the electric field applied to devices. Since the electric field in SiC devices must be higher than Si devices, it is very important for development of radiation hardness SiC devices to understand the responses of SEGR. We investigated Linear Energy Transfer (*LET*) dependence of critical electric field (E_{cr}) at which SEGR occurs in SiC MOS capacitors.

The MOS capacitors used in this study were fabricated on an n-type 4H-SiC epitaxial layer. The gate oxides with two different thicknesses were formed by the pyrogenic oxidation. The thicknesses of the gate oxides were estimated from capacitance-voltage (*C*-*V*) measurements to be 16.8 ± 2.0 nm and 72.5 ± 12.5 nm. Samples were irradiated with nickel ions at 9 and 18 MeV, krypton ions at 322 MeV xenon ions at 454 MeV, and osmium ions at 490 MeV in TIARA/JAEA, and krypton ions at 405 MeV in CYRIC/Tohoku Univ. The *LET* of heavy ions was ranged from 14.6 to 94.2 MeV・cm^2/mg. During the ion irradiation the current through the gate oxide of the MOS capacitors was monitored under direct current (DC) biases. They were biased from 1.0 to 14 MV/cm toward the accumulation condition. Because we observed destruction of the gate oxide when the current density was 1 A/cm^2 using optical microscope, we defined the E_{cr} as the electric field at which the current density exceeded 1 A/cm^2.

The currents density through the gate oxide of the 4H-SiC MOS capacitors with and without ion irradiation is shown in Fig. 1 as a function of the electric field applied to the gate oxides[2]. For no-irradiation samples, the current densities below 8 MV/cm are under 10^{-8} A/cm^2. This indicates that the quality of the gate oxides is sufficient with regard to the current density. After increasing gradually, the current density increases sharply to 1 A/cm^2. Although the electric field dependence of the current density is qualitatively similar to all samples, the E_{cr} for an irradiated sample is smaller than that for a sample without irradiation (E_{cr0}) and decreases with increasing *LETs*. This results indicates that SEGR occurs at a lower electric field when ions with a higher *LET* penetrate SiC MOS devices.

Figure 2 shows the *LET* dependence of the reciprocal of E_{cr} ($1/E_{cr}$) for SiC MOS capacitors with thin and thick gate oxides[2]. The E_{cr} values reported for Si MOS capacitors with 18-nm-thick gate oxide are also plotted in the figure for comparison[1]. For both SiC MOS capacitors with thin and thick oxide, the values of $1/E_{cr}$ increased linearly with increasing *LET*. A linear relation between *LET* and $1/E_{cr}$ has been reported for Si MOS capacitors[1]. However, the slopes of the *LET*-$1/E_{cr}$ lines for Si MOS capacitors was larger than those of the *LET*-$1/E_{cr}$ lines for SiC MOS capacitors. This result suggests that SiC MOS devices are less susceptible to SEGR than Si MOS capacitors, especially in high *LET* regions. For oxide thickness dependence, SiC MOS capacitors with thin oxide showed lower $1/E_{cr}$ values than those with thick oxide at each *LET* value. Thus, this indicate SiC MOS capacitors with thin oxide have higher SEGR resistance than those with thick oxide.

References

1) F. W. Sexton et al., *IEEE Trans. Nucl. Sci.* **44**, (1997) p. 2345.
2) JAEA-Review, *JAEA Takasaki Annual Report* 2013 in press.

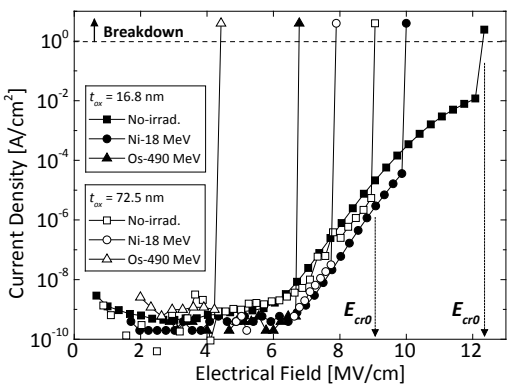

Figure 1. Leakage current densities of SiC MOS capacitors with and without heavy ion irradiation[2].

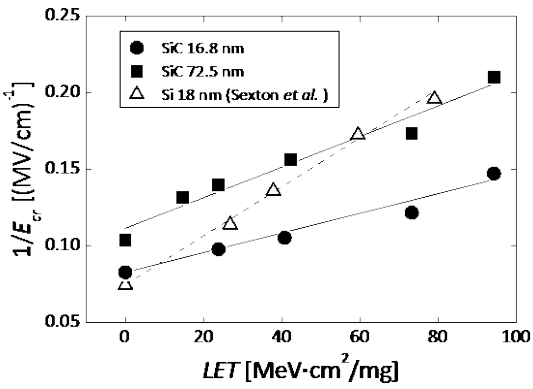

Figure 2. *LET* dependence of SEGR electric field in SiC and Si MOS capactitors[2].

1.

II. NUCLEAR INSTRUMENTATION

II. 1. Present Status of the CYRIC Accelerator Facility

Wakui T.[1], Shinozuka T.[1], Shimada K.[1], Shimbara Y.[1], Sakemi Y.[1], Itoh M.[1], Kawamura H.[1], Inoue T.[1], Ohmiya Y.[2], Takahashi N.[2], Takahashi K.[2], Suzuki J.[2], and Homma T.[2]

[1]Cyclotron and Radioisotope Center, Tohoku University
[2]SHI Accelerator Service

The CYRIC has a 930 cyclotron (*K*=110 MeV) and a HM12 cyclotron. The 930 cyclotron is mainly used in the fields of science and engineering, for the purposes of research, education and university-industry collaboration. In contrast, the HM12 cyclotron is wholly used for the production of radioisotopes for positron emission tomography. Both the cyclotrons were not in operation from March in 2011 to October in 2012, because of the repair work on the accelerator facilities damaged by the Great East Japan Earthquake[1)]. In this report, we describe the operational status and improvements after restarting the joint use in 2012-2013.

The performance of the accelerator facilities is assessed by their availability and reliability. The availability is defined as the ratio of delivered beam time to the scheduled beam time. The reliability is measured according to the average operating time between failures. In 2012, the availability and reliability of the 930 cyclotron were 95.3% and 204 hours, respectively. The reliability was four times worse than that in the usual years. The lower value was due to initial failures occurring for a month after restarting the joint use. In contrast, for the HM12 cyclotron, we attained the availability of 99.9% and set the best record in the history of HM12 operation at CYRIC. The reliability was 155 hours. In 2013, the availability and reliability of the 930 cyclotron were 99.6% and 729 hours, respectively. These values were almost the same as that in the usual years. For the HM12 cyclotron, the availability was 99.8% and the reliability was 167 hours. We could maintain a good performance of the HM12 cyclotron also in 2013.

The 930 cyclotron has provided ion species from hydrogen to argon. Heavy ions delivered for the 930 cyclotron are produced using a 10 GHz electron cyclotron resonance ion source (ECRIS)[2)]. In these few years, improvements in beam intensity and energy and

also new ion species were requested from joint use users. To realize the requests, we have introduced the so-called gas mixing method into the 10 GHz ECRIS[3,4]. In this method, a light gas such as helium for neon or lighter and oxygen for argon or heavier is added to ECR plasma. The light gas increases a confinement time of heavier ions. As a result, the production of high charge state ions can be enhanced. This improves the beam intensity.

Table 1 shows the beam intensities extracted from the ECRIS with and without the gas mixing method. We have successfully increased the beam intensities two to six times. Moreover, the beams of $^{84}Kr^{19+}$ and $^{129}Xe^{23+}$ have newly been observed with the intensities higher than 1 eμA, which is an indication of acceleratable beam current by the 930 cyclotron at CYRIC.

The beam energy accelerated by a cyclotron is proportional to the square of the charge state of ions. Thus, the beam energy can also be increased by increasing the charge state of ions. Table 2 shows the beam energies of ions provided for the join use, before and after introducing the gas mixing method. The range of beam energies has been enhanced two to three times for C and Ar ions. The ions of Kr and Xe have newly been provided for the joint use at CYRIC, owing to the gas mixing method.

For further enhancement of beam intensity, beam energy and variety of ions from the 930 cyclotron, we have some improvement plans for ECRIS including introduction of so-called an accel-decel extraction system and of a metallic sample insertion system.

References

1) Wakui T., Itoh M., Shimada K., Yoshida P. H., Shinozuka T., and Sakemi Y., *Tohoku J. Exp. Med.* **233** (2014) 221.
2) Wakui T., et al., *CYRIC Annual Report* 2010-2011 31.
3) Geller R., Electron Cyclotron Resonance Ion Source and ECR plasmas, Institute of Physics Publishing, Bristol, 1996.
4) Brown G. I., The Physics and Technology of Ion Sources, WILEY-VCH, Weinheim, 2004.

Table 1. Beam intensities from the 10 GHz ECRIS with and without the gas mixing.

Ion species	without gas mixing	with gas mixing
$^{12}C^{4+}$	16 eμA	55 eμA
$^{18}O^{5+}$	60 eμA	125 eμA
$^{40}Ar^{12+}$	1.2 eμA	7 eμA
$^{84}Kr^{19+}$	not observed	3 eμA
$^{129}Xe^{23+}$	not observed	1 eμA

Table 2. Beam energies before and after introducing the gas mixing.

Ion species	Previous	This work
$12C^{4+}$	70 MeV	140 MeV
$^{40}Ar^{12+}$	128 MeV	378 MeV
$^{84}Kr^{19+}$	not provided	451 MeV
$^{129}Xe^{23+}$	not provided	422 MeV

II. 2. Recovering Cyclotrons from the Great East Japan Earthquake

Wakui T.[1], Shinozuka T.[1], Shimada K.[1], Shimbara Y.[1], Sakemi Y.[1], Itoh M.[1], Kawamura H.[1], Inoue T.[1], Ohmiya Y.[2], Takahashi N.[2], Takahashi K.[2], Suzuki J.[2], and Homma T.[2]

[1]Cyclotron and Radioisotope Center, Tohoku University
[2]SHI Accelerator Service

On March 11, 2011, the Great East Japan Earthquake struck the CYRIC[1)]. The accelerator facilities of CYRIC got serious damage. Afterwards, we put all of our effort into recovering the accelerator facilities. After the restoration activity was completed, the joint use of the accelerator facilities was re-started at October 2012. In this report, we describe briefly the damage and restoration activity of two cyclotrons and related equipment.

The shake, which continued for a long time, damaged the 930 cyclotron, the HM12 cyclotron and related equipment. Damage of the 930 cyclotron appeared in the two columns on which the 930 cyclotron is placed, the main coil, the mounting base of the acceleration chamber, the puller electrodes, the dee electrode tip, and the drive component of the deflector. Furthermore, the alignment and horizontal level of all the beam lines was changed; it was necessary to adjust the alignment and level of the beam lines. Fortunately, however, the dee electrodes and earth plates were not damaged. The most serious damage in the above mentioned was the columns. Damage was found not only in the mortar of the column surface but also the internal concrete. This caused a serious tilt of the horizontal plane of the 930 cyclotron.

Damage to the HM12 cyclotron occurred in the lock pins that fix the HM12 cyclotron on the rail, the cooling water pipes, the waveguide of the RF system, the cable bearer, the water supply device for ^{18}F, and the compensator drive system. In addition, shielding door of the target room in which the HM12 cyclotron is placed was severely damaged. The shielding door blocked the entrance to the target room and made it impossible to bring in machinery and materials required for the repair work.

Before the repair work, we have discussed the master plan for recovery. Figure 1

shows the outline process flow of the repair work. We planned to start by removing the beam lines from the cyclotron room to repair the columns of the 930 cyclotron. In parallel, our priority was to repair the shielding doors, because it was difficult to bring machinery in and out for the repair work. The restoration was started at June 2011, after the implementation of the first supplemental budget was enabled.

The repair work on the 930 cyclotron started after the removal of the beam lines from the cyclotron room. We placed four 200-t jacks and lifted the 930 cyclotron without applying weight to the columns. Then the columns were repaired with grout and fixed to the base plate of the 930 cyclotron with epoxy resin. After that, all the equipment including the acceleration chamber was removed, and the position and horizontal level of the 930 cyclotron were adjusted with the accuracy of 0.2 mm. Then we sequentially conducted the vacuum test, current test of coils, and operation test of the drive component. During the tests, we found some new problems such as water leaks, a malfunction of the cryopump, and so on. After dealing with the problems, we completed the repair work of the 930 cyclotron. On July 3, we succeeded in beam acceleration and extraction for the first time after the earthquake.

Before the repair work on the HM12 cyclotron, the shielding door, which blocked the entrance to the target room, was repaired. The shielding door of 15 t fell onto the floor and its drive component was completely destroyed. Since the load capacity of the crane in the target room is only 2.8 t and there was no way to bring in large machinery through the narrow stairway, it seemed impossible to lift the shielding door. Instead the use of crane, we made full use of chain blocks, jacks, and the beam of the crane in order to lift the shielding door. Then, we exchanged the destroyed drive component and adjusted the position precisely by millimeter increments. During the repair of the shielding door, we conducted the earlier repair work on some damaged parts and the fabrication of replacement parts for the HM12 cyclotron. After the shielding door was repaired, we started the repair work on the HM12 cyclotron. Although some problems were newly found while the repair work, the repair of them was easy, fortunately. On May 2012, the repair work on the HM12 cyclotron was completed, and the beam was supplied for production tests of radiopharmaceuticals for PET.

After the repair work was finished, we finally restarted the joint use of the HM12 cyclotron on October 16, 2012, and of the 930 cyclotron on October 25, 2012. The beam parameters such as the beam current and the beam spot size were almost the same as before the earthquake for both cyclotrons. The reliability which is defined as the ratio of scheduled

beam time divided by number of faults was almost returned for both cyclotrons, though there were some minor troubles for a month after restarting the joint use.

Reference

1) Wakui T., Itoh M., Shimada K., Yoshida P. H., Shinozuka T., and Sakemi Y., *Tohoku J. Exp. Med.* **233** (2014) 221.

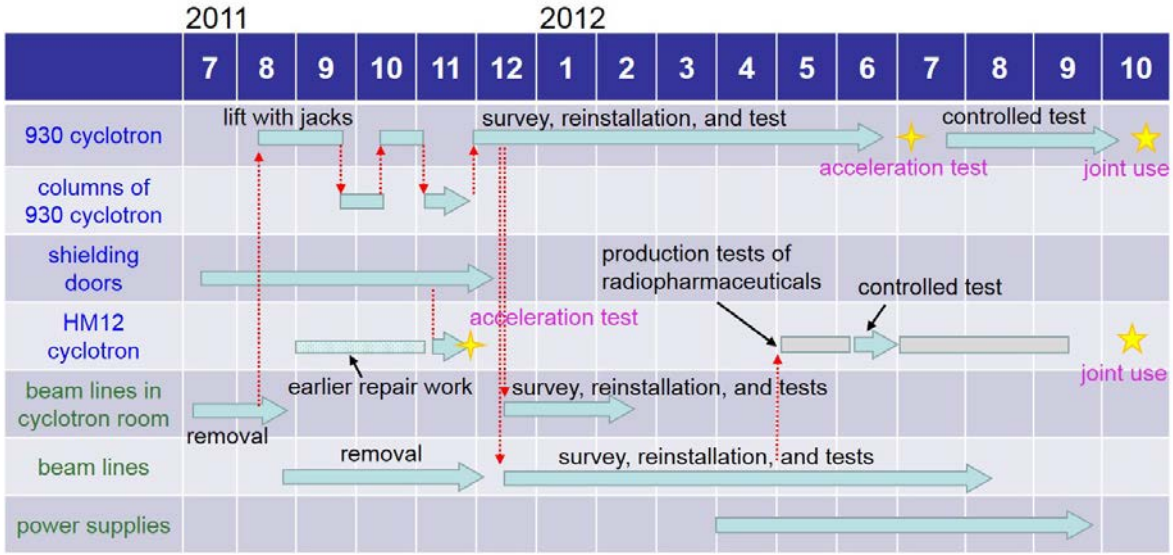

Figure 1. Outline process flow of the repair work.

II. 3. Development of Tetrode Extraction System for 10 GHz Electron Cyclotron Resonance Ion Source

Shimbara, Y.[1], Wakui, T.[1], Ohmiya, Y.[2], Takahashi, N.[2], Takahashi, K.[2], Suzuki, J.[2], and Honma, T.[2]

[1]Cyclotron and Radioisotope Center, Tohoku University
[2]SHI Accelerator Service

High power beam of the 930 cyclotron is requested from many different areas. One promising method to enhance beam power is to increase beam current from ion source. Heavy ions provided for the 930 cyclotron are produced by a 10 GHz electron cyclotron resonance (ECR) ion source[1-3)]. Particles extracted from the ECR ion source have many different charges. If total beam current from the ion source increases, the number of highly charged particles, of which the current is relatively low, also increases. Under the same magnetic field of cyclotron, highly charged particles can be accelerated up to higher energy. In addition, more massive particles can also be accelerated. Therefore, enhancement of total beam current from ion source is important to increase not only beam current but also beam energy and accessible mass.

Present extraction system of the 10 GHz ECR ion source is diode, which consists of plasma electrode and extraction electrode. Since no booster exists between the ion source and the cyclotron, the bias of the extractor becomes initial beam energy of the cyclotron. However, initial beam energy of the cyclotron is determined by the accelerated beam energy. It means that the bias of the extractor of the ion source is determined by the accelerated beam energy.

Figure 1 shows calculated beam current and emittance versus position of extraction electrode in the present extraction system. In the low current region, beam current increases as electric field around the aperture of the plasma electrode becomes strong. If the extraction electrode is placed closer to the plasma electrode, electric field becomes strong and extracted beam current increases. At the same time, however, beam emittance also becomes worse. Therefore, we cannot independently control beam current and emittance. In

order to independently control beam current and emittance, at least two additional electrodes are needed. At present, we made a prototype tetrode extraction system.

The present extraction electrode, the diameter of which is 7 cm, is supported and electrically connected to the ground by the outer shied flange of the ion source (see the left hand of Fig. 2). In order to support the prototype extraction system, we used the same flange as the present extraction electrode. Therefore, the prototype extraction system must have had the diameter of 7 cm.

In order to calculate beam current and emittance, we used ion-source extraction simulation program IGUN[4)]. IGUN automatically calculates electric field, plasma sheath and trajectory of ions. By searching parameters of shapes and biases of electrodes using IGUN, we decided the design of the tetrode extraction system as shown in Fig. 3. The picture of the tetrode extraction system is shown in Fig. 4. As mentioned above, beam current increases by biasing the extraction electrodes more and placing the extraction electrodes closer to the plasma electrode. However, if electric field is too strong, plasma sheath in the aperture of the plasma electrode is concaved into the plasma chamber and the beam current decreases. In addition, beam emittance becomes worse. Figure 5 shows calculated current and emittance versus bias of the extraction electrode. Figure 6 shows calculated current and emittance versus distance between the plasma electrode and the extraction electrode. Figures 5 and 6 suggest that there are appropriate bias and position of the electrode to obtain maximum beam current. In order to effectively extract beam, the aperture of the plasma electrode should have enough size. However, if the aperture size is too large, plasma sheath is concaved, which results in reduction of beam current. In addition, beam emittance becomes worse. Figure 7 indicates that the appropriate diameter is 8 mm. Since particle just emitted from the extraction hole is slow, the trajectory of the particle is easily bent by the distorted electric field, which makes beam emittance large. In order to make homogeneous electric field, appropriate thickness was 1 mm. By searching biases, we found the best biases of plasma, extraction and focusing electrodes, which were 10 kV, -7 kV and 6.5 kV, respectively. Finally, we obtained beam trajectories as show in Fig. 8.

The prototype extraction system was installed as shown in the right hand of Fig. 2 and tested with natural oxygen gas. Beam current of ^{16}O was measured with a Faraday cup placed at the downstream of the first bending magnet from the ion source. During the test, we obtained high beam intensity that has never been achieved before for a few minutes. However, beam intensity rapidly dropped down. We found that beam emitted from the

aperture of the plasma electrode immediately deteriorated the ceramic rods supporting the electrodes and the electrodes were shorted. Therefore, next extraction system should have some mechanism to keep the insulators clean.

References

1) Wakui T, Shinozuka T, Shimada K, Sakemi Y, Itoh M, Yoshida H, Chiba S, Ohmiya Y, Takahashi N, Takahashi K, Yokogawa S, Suzuki J, *CYRIC Annual Repot* 2010-2011, 31.
2) Nakagawa T, *Jpn, J. Appl. Phys.*, **30** (1991) L930.
3) Nakagawa T, Aihara T, Higurashi Y, Kidera M, Kase M, Yano Y, Arai I, Arai H, Imanaka M, Lee SM, Arzumanyan G, Shirkov G, *Rev. Sci. Instrum.* **75** (2004) 1394.
4) Becker R, Herrmannsfeldt WB, *Rev. Sci. Instrum.* **63** (1992) 2756

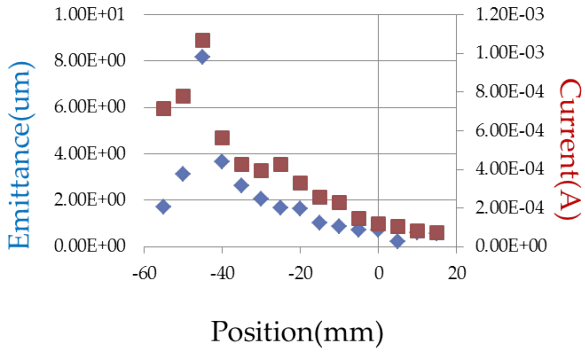

Figure 1. Calculated beam current (squares) and emittance (diamonds) versus position of ground electrode in present extraction system.

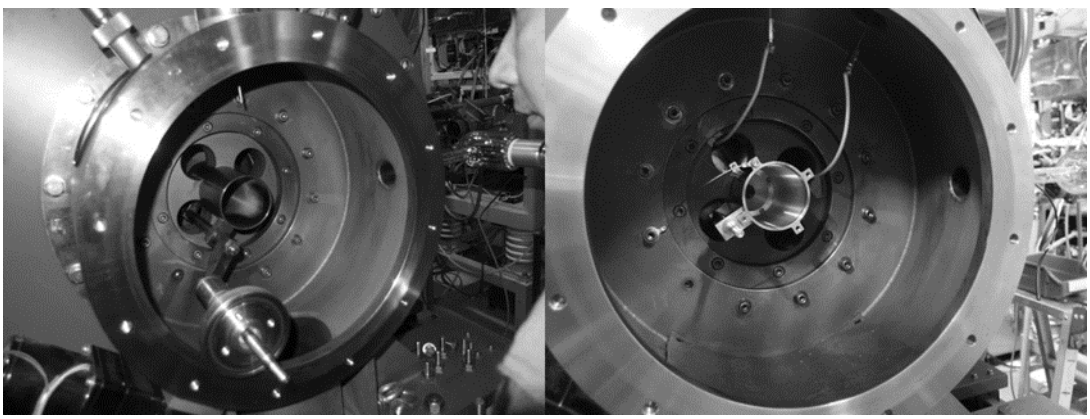

Figure 2. (Left) present and (right) prototype extraction system placed at exit of ion source. Both extractors are supported by the shield flange of the ion source.

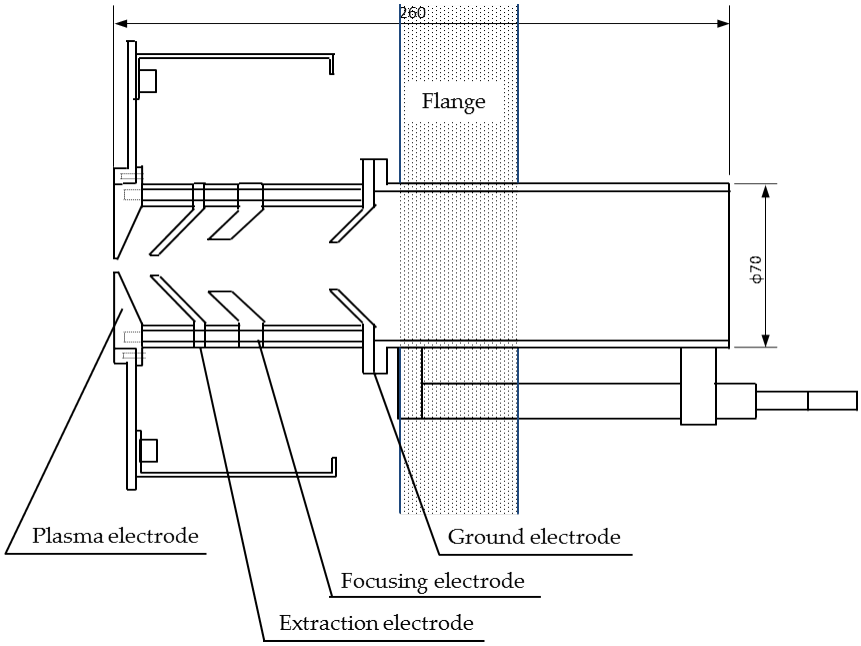

Figure 3. Schematic view of tetrode extraction system. Four electrodes are connected with ceramic rods.

Figure 4. Picture of tetrode extraction system.

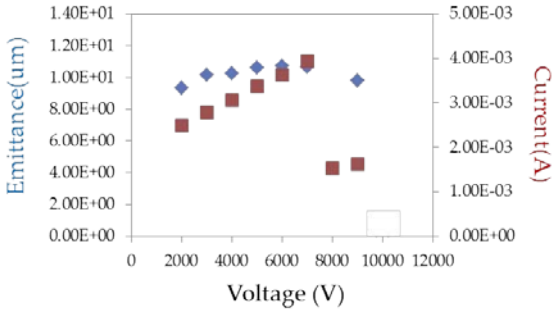

Figure 5. Calculated current (squares) and emittance (diamonds) versus bias of extraction electrode of tetrode extraction system.

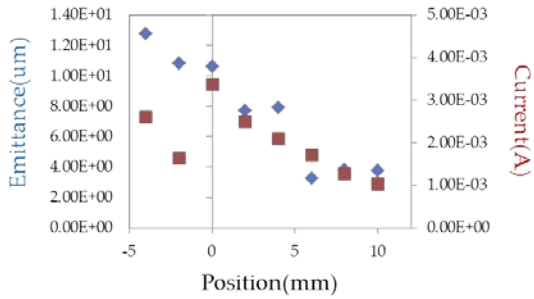

Figure 6. Calculated current (squares) and emittance (diamonds) versus position of extraction electrode of tetrode extraction system.

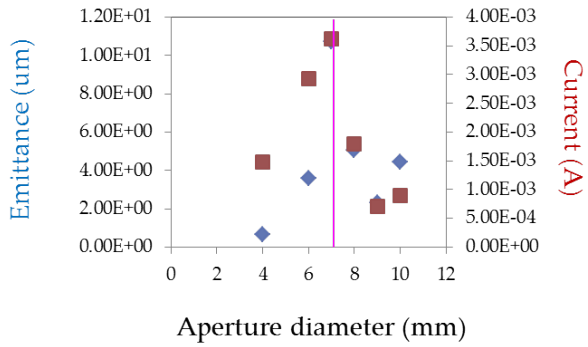

Figure 7. Calculated current (squares) and emittance (diamonds) versus aperture diameter in tetrode extraction system.

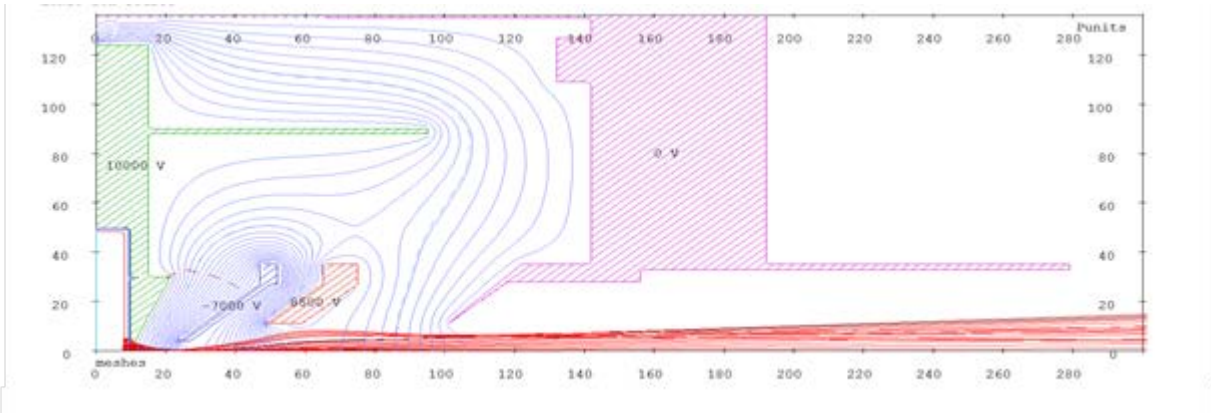

Figure 8. Optimized setting of electrodes and calculated trajectories of particles.

II. 4. Development of Scattered Proton Detector for Σp Scattering Experiment

Miwa K., Akazawa Y., Honda R., and Shiozaki T.

Department of Physics, Tohoku University

We are planning to perform a Σ proton scattering experiment at the K1.8 beam line in J-PARC, which is named as the E40 experiment[1)]. In the E40 experiment we aim to measure the differential cross sections of Σ^+p and Σ^-p elastic scatterings and $\Sigma^-p \rightarrow \Lambda n$ inelastic scattering by detecting more than 10,000 scattering events. Through this experiment, we will reveal the following two physics topics. One purpose is to verify a large repulsive core which is expected in the Σ^+p channel due to the Pauli repulsive principle in the quark level[2,3)]. The other one is to investigate the ΣN interaction systematically by measuring three isospin separating channels. Experimentally, we use a new experimental technique to resolve an experimental difficulty of a hyperon proton scattering experiment. A liquid hydrogen (LH2) target is used as both Σ production and Σp scattering targets. The LH2 target is surrounded by a cylindrical fiber tracker (CFT) and a BGO calorimeter and charged particles from the target are detected by these detectors. Because both the Σ production reaction ($\pi^{\pm}p \rightarrow K^+\Sigma^{\pm}$) and the Σp scattering reaction ($\Sigma p \rightarrow \Sigma p$) are ”two-body reaction”, the Σp scattering events can be identified kinematically by measuring four vectors of $\pi^{\pm}$ beam, K^+ and scattered proton.

In the experiments at CYRIC, we performed several test experiments to evaluate the performance of the detectors which were developed for the E40 experiment. The first one was a BGO calorimeter and second one was a cylindrical fiber tracker (CFT). In this document, we will show the obtained results for these detectors from the CYRIC experiments.

1. BGO calorimeter Test

BGO calorimeter will be placed at the outer side of CFT to measure the total energy

of the scattered protons in the E40 experiment. Now we are testing a large BGO calorimeter which has the same effective length of 40 cm as that of CFT. The size of the BGO calorimeter is 400 × 25 × 32 mm^3 (Fig. 1 (a)). The following performances are required for the BGO calorimeter.

• BGO calorimeter has a stopping power up to 140 MeV proton.

• The energy resolution is required to be better than $\sigma/E = 4\%$ for 80 MeV proton.

In order to evaluate the energy resolution of BGO calorimeter, we at first checked the resolution for 661 keV γ ray from a ^{137}Cs source. The obtained resolution was 11% as shown in Fig. 1 (b). From this result, for the 80 MeV proton, ~1.1% of resolution was expected. In order to measure the energy resolution for this high energy proton, we irradiated a proton beam of 80 MeV to the BGO calorimeter at CYRIC. Figure 1 (c) shows the obtained ADC spectrum for 80 MeV proton. The reasonable resolution of 1.2% was obtained. This was sufficient resolution for us.

2. Development of Cylindrical Fiber Tracker (CFT)

The other key detector for the E40 experiment is the cylindrical fiber tracker (CFT). CFT is used to measure the trajectory from the LH_2 target and to measure the dE/dx of the particle to perform the particle identification. CFT has two different fiber configurations, that is, the ”φ” configuration and the ”U” configuration. In the ”φ” configuration, the fibers are placed in a straight line along the beam direction. On the other hand, in the ”U” configuration, the fibers are placed with a tilt angle. By combining these two layer configurations, three dimensional tracking can be possible by CFT. Now, we have developed a prototype of CFT, which consists of three layers of ”φ” (”φ1”), ”U” and ”φ” (”φ2”) configurations. The radii for the ”φ1”, ”U” and ”φ2” layers are 4 cm, 5 cm and 6 cm from the center, respectively. For the beam direction, these layers have an effective length of 40 cm. As for the fiber size, diameter of 0.75 μm was used by considering both the light yield for minimum ionization particles and the thickness of the fiber material. For the readout of CFT, we used the MPPC PCBs and EASIROC boards[4]. As for MPPCs, we used HAMAMATSU S10362-11-050P whose pixel size was 400 considering the wide dynamic range for the energy deposit by MIP and protons at CFT. Figure 2 shows a photo of the CFT prototype where the three layers are combined to the one prototype detector.

For the E40 experiment, the following points should be studied for CFT.

• We have to check that trajectories can be reconstructed by the CFT prototype. We need angular resolution enough to identify scattering events.

• We have to check that CFT has sufficient light yield for MIP and has enough dynamic range for a large energy deposit by low energy protons.
• We have to check whether particle identification between π and proton can be done by using the information of ΔE-E relation where ΔE is the energy deposit at fibers and E is the total energy deposit at BGO calorimeter which is installed at the outer part of CFT.
These topics were tested in the test experiments at CYRIC where CFT and BGO were used. In the following sections, the obtained results are described.

3. Combined Test with CFT and BGO

In the E40 experiment, scattering events are identified by combining the information of the scattering angle and the proton energy. In order to identify scattering events by using the prototype of CFT and BGO, we performed a test experiment at CYRIC. A proton beam of 80 MeV was irradiated to a polyethylene (CH_2) target, whose thickness was 200 μm. The pp and pC scattering events were detected by the prototype of CFT and BGO. Figure 3 shows the experimental setup and photographs. The CFT and BGO detectors were placed at the left side from the beam axis. By using 6 fiber hits (3 layers × 2 times), trajectory of the scattered proton was reconstructed three dimensionally. In this experiment, we evaluated the particle identification performance by the ΔE-E relation at the CFT and BGO detectors and the identification performance of scattering events from the scattering angle and the total energy.

3. 1 Particle identification by the ΔE-E method

In the E40 experiment, the particle identification between proton and π is performed by the ΔE-E method where ΔE is the energy deposit at the CFT fibers and E is the total energy at BGO. Figure 4 shows the ΔE-E correlation plot obtained in the experiment. The loci corresponding to proton and deuteron can be identified very well. In order to estimate the π contribution, we overwrote the relation obtained for the cosmic ray trigger. We confirmed that proton and π can be separated clearly at this energy region. The PID power between proton and π at 80 MeV energy region was obtained to be 5 σ. The energy resolution of the CFT detector was obtained to be 10% for proton and 16% for π by summing up the 6 fiber layers. By considering these resolutions, particle identification at the higher energy region can be performed.

3. 2 Identification performance of scattering events

In order to identify the pp and pC scattering events, the correlation between the scattering angle and the total energy of the proton was measured as shown in Fig. 5 (a). The

scattering angle was obtained as the crossing angle between the proton trajectory and beam axis where we assumed that the proton beam was straight. The loci corresponding to the pp scattering and the pC elastic and inelastic scatterings can be identified clearly. In order to identify the scattering events, we define the following value,

$$\Delta E = E_{measure} - E_{calculate},$$

where $E_{measure}$ is the measured energy and $E_{calculate}$ is calculated energy from the scattering angle in the specific reaction. For the pp scattering, the $E_{calculate}$ value is represented as a line in Fig. 5 (a). If we consider the pp scattering kinematics, the ΔE value for pp scatterings should be around 0. Figure 5 (b) shows the relationship between the ΔE value and the scattering angle for the pp scattering kinematics. Figure 5 (c) shows the ΔE distribution for the events with scattering angle between 30^o and 32^o. The peak around ΔE = 0 corresponds to pp scattering. In order to evaluate the ΔE resolution, in Fig. 5 (d) we compared the experimental value (black triangle) with the simulation (red box and blue circle) for each scattering angle. The red box represents the ideal resolution obtained in the simulation where fiber position is located correctly and realistic energy resolutions for BGO and fibers are taken into account. Because the CFT angular resolution was worse than the ideal value, the obtained ΔE resolution was also worse than the ideal value. By taking into account the realistic angular resolution for CFT in the simulation, the experimental value could be roughly reproduced as shown in the blue circle in Figure 5 (d). Because the ΔE resolution can be reproduced in the simulation, this means that each resolution is understood well. In the present performance, the ΔE resolution was obtained to be 1.8 MeV (σ). Although this is worse than the ideal value of 1.4 MeV, this resolution is enough to identify the scattering events. For the actual CFT detector, we also aim to improve the ΔE resolution up to the ideal value by improving the fiber alignment at the fabrication of CFT.

4. Summary

We have performed experiments to evaluate performances of detectors developed for Σp scattering experiment (E40). The energy resolution of BGO calorimeter, whose size was 400 × 25 × 32 mm^3, was obtained to be 1.1% for 80 MeV proton. This performance is enough for our requirement. We also performed a combined test using BGO and CFT. The particle identification (PID) using ΔE-E relation was studied. The PID power between proton and π at 80 MeV energy region was obtained to be 5 σ. We also confirmed that identification of elastic scattering events using scattering angle and energy information was

possible with a reasonable resolution. Based on these studies, we will construct the actual detector of CFT and BGO for the E40 experiment.

References

1) K. Miwa et al., J-PARC proposal, http://j-parc.jp/researcher/Hadron/en/pac 1101/pdf/KEK J-PARC-PAC2010-12.pdf
2) M. Oka, K.Shimizu, K. Yazaki, *Nucl. Phys.* **A464** (1987) 700.
3) C. Nakamoto, Y. Suzuki, Y. Fujiwara, *Prog. Theor. Phys.* **94** (1995) 65.
4) Y. Akazawa, *Master's thesis, Tohoku University* (2014).

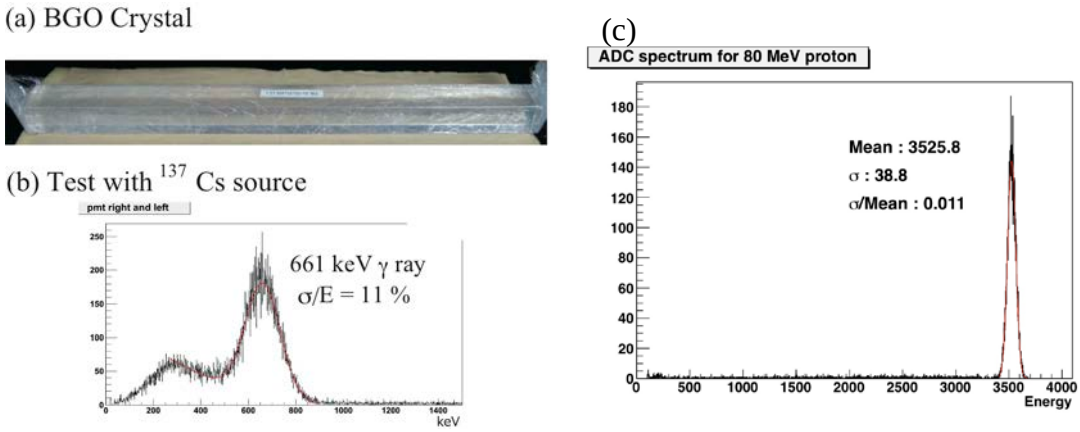

Figure 1. (a) Photograph of a BGO calorimeter which is almost the same size with the actual equipment. The size is 400 × 25 × 35 mm^3. (b) Energy spectrum obtained for γ ray of 661 keV from a ^{137}Cs source. Energy resolution of σ/E = 11% was obtained for 661 keV. (c) ADC spectrum for a 80 MeV proton beam. The energy resolution of 1.2% was obtained.

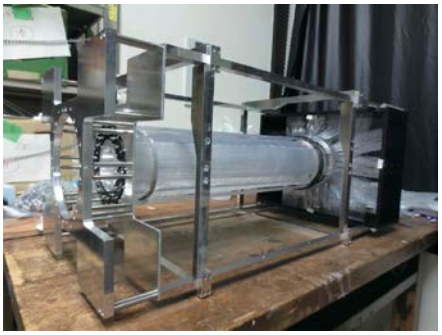

Figure 2. Photograph of the CFT prototype. Three layers are combined together. The readout MPPCs are mounted at the black frame at the downstream.

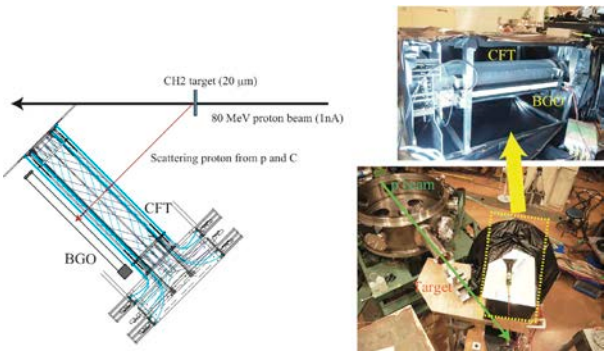

Figure 3. Experimental setup and pictures. The CFT and BGO detectors were placed at the left side from the beam axis. A proton beam of 80 MeV was irradiated to CH2 target of 20 μm thickness and scattered protons were detected by the CFT and BGO detectors.

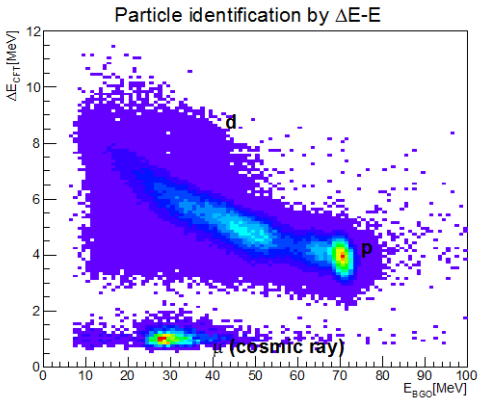

Fig 4. ΔE-E correlation plot. The ΔE is a sum of 6 fiber layers. Loci corresponding to proton can be identified. Cosmic ray data are also overwritten to estimate the π contribution.

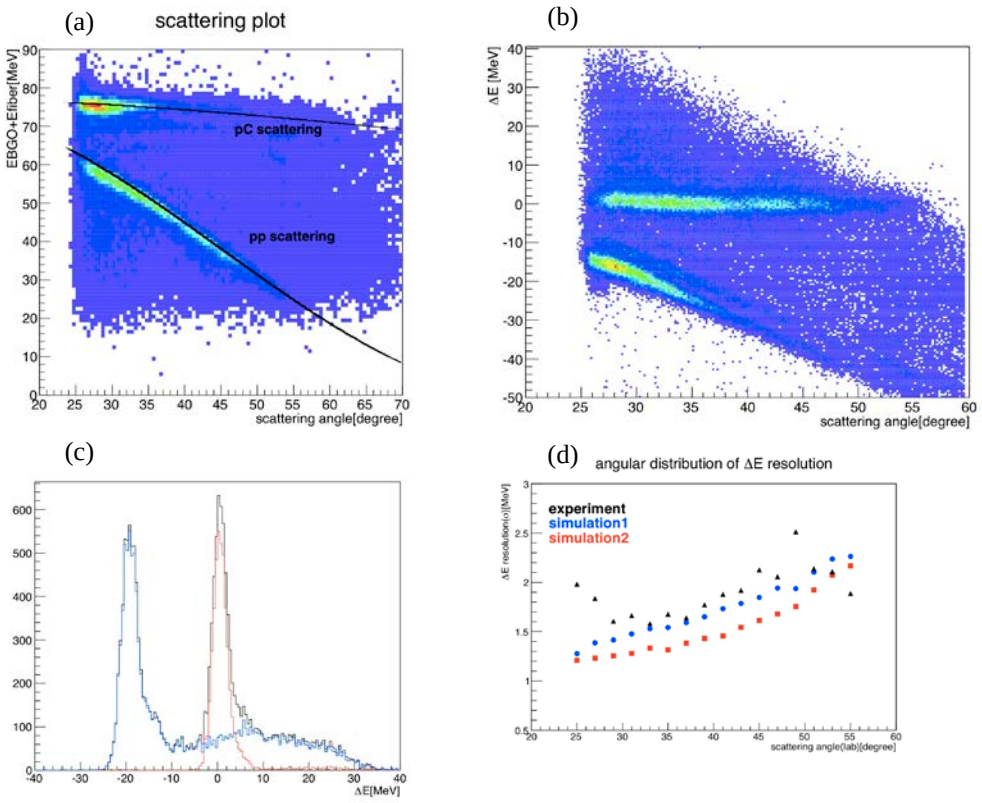

Figure 5. (a) Relation between the scattering angle and the total energy of scattered proton. The loci corresponding to pp scattering and pC elastic scattering can be identified. The lines are kinematical relations between the scattering angle and the kinetic energy for pp and pC scatterings, respectively. (b) Relation between the scattering angle and ΔE for pp kinematics. The locus at the ΔE = 0 corresponds to pp scattering event. (c) ΔE spectrum for pp kinematics. The scattering angle was selected from 30^{o} to 32^{o}. Red and blue histograms correspond to the events with and without hits of pp ID counter, respectively. Therefore the red histogram shows the contribution from pp scattering event. (d) Relation between ΔE resolution and scattering angle for experimental data (black) and simulations (blue, red). In the both simulations, the realistic energy resolutions of fibers and BGO were taken into account. As for the angular resolution of CFT, the obtained angular resolution of 1.0 degree and ideal resolution of 0.77 degree were considered, respectively. In the forward direction which corresponded to 25^{o} scattering angle, there was a BGO support frame and proton had to penetrate this support. Therefore the ΔE resolution deteriorates in the forward angle for the experimental data.

II. 5. Development of the Magnetometer toward the Search for the Electron EDM

Inoue. T.[1, 2], Ando. S.[2], Aoki. T.[2], Arikawa. H.[2], Ezure. S.[2], Harada. K.[2], Hayamizu. H.[2], Ishikawa. T.[2], Itoh. M.[2], Kato. K.[2], Kawamura. H.[1,2], Uchiyama. A.[2], and Sakemi. Y.[2]

[1]*Frontier Research Institute for Interdisciplinary Science, Tohoku University*
[2]*Cyclotron and Radioisotope Center, Tohoku University*

A permanent electric dipole moment (EDM) of a particle, an atom or a molecule directly violates the time reversal symmetry, and hence the CP symmetry because of the CPT theorem. Since the EDM is sensitive to the CP violation in the theories beyond the standard model (SM) of elementary particles[1)], the EDM is a good candidate to probe the physics beyond the SM. We plan to search for the electron EDM using laser cooled francium (Fr) atoms. By using the laser cooled atom, the long coherence time can be realized and some systematic effects, such as a motional magnetic field and a field inhomogeneity, which limit the EDM sensitivity in the previous experiments, can be suppressed[2)]. The laser cooling technique is relatively easily applicable to the Fr atom, since the Fr atom is an alkali atom. Furthermore, the Fr atom has the largest enhancement factor of electron EDM due to the relativistic effect in the alkali atoms. In view of these advantages, we have chosen the Fr atom as the substance where the electron EDM is searched for.

Experimentally, the atomic EDM is deduced from a tiny change in spin precession frequency induced from a reversal of an electric field E applied to the atom along a magnetic field. The electric field couples with the EDM, while the magnetic field defines the quantization axis. A small fluctuation of the magnetic field, however, can easily produce the false EDM effect. In our assumed experimental condition that is E = 100 kV/cm application and the EDM sensitivity of 10^{-29} $e$cm, the frequency change due to the EDM is less than 1 μHz. This tiny frequency change corresponds to the magnetic field fluctuation of about 10 fT. Thus we need to monitor the magnetic field with the sensitivity of 10 fT order. In order to realize this sensitivity we are now developing a rubidium (Rb) atomic magnetometer based on a nonlinear magneto-optical rotation (NMOR) effect[3)].

The principle of the NMOR effect is as follows. The linear polarized light, whose wavelength is tuned to the Rb atomic transition, irradiates the Rb atom along an applied magnetic field. A spin alignment state of the Rb atom is produced by the optical pumping. Then, the produced alignment state precesses around the magnetic field and is probed by the incident light. This probe results in the rotation of the polarization plane of the incident light, which has the dispersive shape as a function of the magnetic field. Thus the magnetic field can be monitored by measuring the rotation angle of the polarization plane. However, the NMOR spectrum is observed only around $B = 0$ T, since the optically pumped alignment relaxes before the full alignment in the high field. In the EDM measurement, the finite field is required to define the quantization axis. We employed the amplitude modulated (AM) NMOR method[4] to monitor the finite field. When the amplitude of the linear polarized light is modulated at a frequency ν_{mod}, the optical pumping rate is also modulated at ν_{mod} (Fig. 1). If the modulation frequency ν_{mod} matches the spin precession frequency $2 \times \nu_{Rb}$ of the Rb atom, the optical pumping efficiency reaches its maximum and hence the spin alignment is produced in the finite field.

The experimental setup for the measurement of the AM NMOR spectrum is shown in Fig. 2. A 4-layer magnetic shield is introduced to suppress the effect of the environmental field. A glass cell, which contains the Rb vapor, is installed inside the shield. The magnetic field is produced by a 3-axis coil, which is also installed inside the shield. The linear polarized light is supplied from a distributed feedback (DFB) laser. The amplitude modulation of the laser light is realized using an acousto-optic modulator (AOM). The laser light transmitted the cell is divided using a polarized beam splitter to measure the rotation angle of the polarization plane. The intensities of the divided lights are detected by photo detectors and these outputs are sensed in a lock-in amplifier to perform a phase sensitive detection.

Figure 3 shows the typical AM NOMR spectrum observed. By using the AM NMOR method, we observed the NMOR spectrum around $B \approx 540$ nT. The line width of the spectrum was about 30 nT. The narrow line width is one of key issues for the highly sensitive magnetometry. Since the line width is limited by the spin decoherence due to the collision between the Rb atom and an inner surface of the glass cell and the residual field of the magnetic shield, we are now preparing a production system of the cell whose inner surface is coated with antirelaxation material, such as a paraffin, and a demagnetization of the shield.

The authors would like to thank A. Yoshimi and K. Asahi for lending the magnetic shield. This work supported by by MEXT/JSPS KAKENHI Grant Numbers 21104005 and 26220705.

References

1) Kriplovich I.B., Lamoreaux S.K., *CP Violation Without Strangeness*, Springer, Heidelberg (1997).
2) Chin C., Leiber V., Vuletic V., Kerman A. J. and Chu S., *Phys. Rev.* A **63** (2001) 033401.
3) Budker D., Kimball D. F., Rochester S. M., Yashchuk V. V. and Zolotorev M., *Phys. Rev.* A **62** (2000) 043403.
4) Pustelny S., Wojciechowski A., Gring M., Kotyrba M., Zachorowski J., and Gawlik W., *J. Appl. Phys.* **103** (2008) 063108.

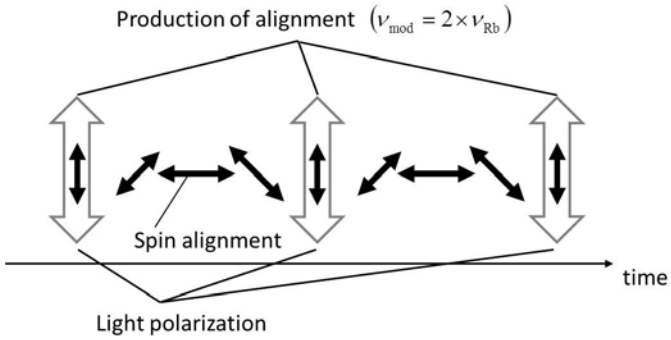

Figure 1. Production of the spin alignment by using the amplitude modulated.

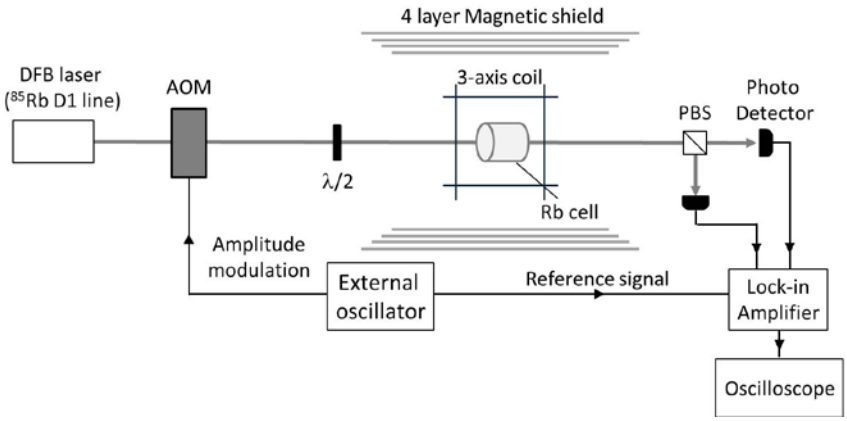

Figure 2. Experimental setup for the measurement of the AM NMOR effect.

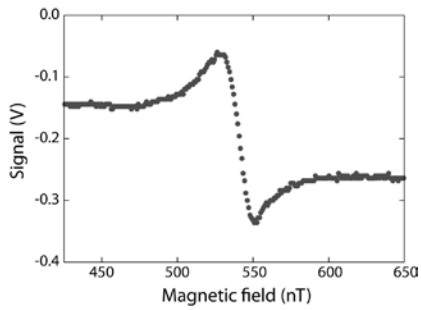

Figure 3. Observed AM NMOR spectrum.

II. 6. A Beam Transportation of Radioactive Francium for Magneto-Optical Trapping Experiments*

Arikawa H.[1], Ando S.[1], Aoki T.[1], Ezure S.[1], Harada K.[1], Hayamizu T.[1], Inoue T.[1,2], Ishikawa T.[1], Itoh M.[1], Kato K.[1], Kawamura H.[1,2], Uchiyama A.[1], and Sakemi Y.[1]

[1]*Cyclotron and Radioisotope Center, Tohoku University*
[2]*Frontier Research Institute of Interdisciplinary Sciences, Tohoku University*

To perform the experiment trapping of a large amount of Fr atoms, we have been constructing a factory of laser-cooled radioactive Fr atoms at Cyclotron and Radioisotope Center (CYRIC) at Tohoku University[1)]. A non-zero electric dipole moment (EDM) shows the violation of the time reversal symmetry. Francium (Fr) is a promising candidate for a high precision measurement of the electron EDM, because it possesses a large enhancement factor of 895[2)]. A factory of laser-cooled radioactive Fr atoms consists of a thermal ionizer, Fr beamline, neutralizer, and magneto-optical trapping system. Recent developments of this factory are focusing on an ion beam transportation.

Fr atoms are produced by the nuclear fusion reaction $^{18}O + {}^{197}Au \rightarrow {}^{215-x}Fr + xn$. The 100 MeV $^{18}O^{5+}$ beam supplied from an AVF cyclotron through a primary beamline is incident on the ^{197}Au target installed in a thermal ionizer (TI). Figure 1 shows a schematic view of the TI. This TI consists of the ^{197}Au target, extraction electrode and the first and second einzel lenses. The first solid state detector (SSD1) is installed immediately above the second einzel lens to measure extracted Fr ions. A gold is heated by a tungsten heater surrounding a target holder. Fr atoms produced inside the target move to its surface by thermal diffusion. Then, Fr atoms are ionized at the surface. Fr ions are extracted to the secondary beamline by an electrostatic potential of typically 1.5 kV. Recently, we observed an extraction 2.4×10^5 ions/s of ^{210}Fr isotopes when the temperature and the primary beam current were 718°C and 2 eμA, respectively. Figure 2 shows the α decay spectrum of the

*Condensed from the article in Proceedings of 7th International workshop on Fundamental Physics Using Atoms (FPUA2014)

extracted Fr isotopes at SSD1.

A beamline is designed to transport the Fr ions from the TI to the region of magneto-optical trap (MOT) as shown in Fig. 3. The main components of the beamline are an electrostatic deflector, three electrostatic quadrupole triplets, and several steerer electrodes. The beamline is entirely constructed by electrostatic optics. The ion optics has also been optimizing with the aid of a computer code SIMION 3D[3)].

We performed two things to improve the transportation since the efficiency from SSD1 to SSD4 was approximately 2% at the beginning of the beamline development. Firstly, we optimized the parameters of electrostatic optics to transport ions to the yttrium target. The parameters were modified to maximize the beam current on the target. In addition, we installed new steerer electrodes. Consequently, 18% of the transport efficiency for ^{210}Fr was achieved. At present, 4.3×10^4 pps of ^{210}Fr could be delivered at the yttrium target.

To increase even the efficiency of trapping in MOT, we also need to focus on the process of the Fr ion extraction. As the gold temperature increases, the thermal diffusion of Fr atoms is promoted. Therefore, the more the temperature rises, the higher the extraction efficiency becomes. However, in fact, a background beam current is drastically increased in the case of our apparatus at the higher target temperature. When the temperature of the gold is 1000°C, a typical background current is on the order of 10 enA in contrast with Fr ions of 10^{-5} enA. The amount of the background ion is not reproducible with respect to the temperature. The background component emitted from the yttrium is transferred to the trapping cell in the same process as Fr atoms. Thus, the collision of Fr atoms with background component must deteriorate the trapping efficiency. To realize a high extraction without degrading the trapping efficiency, we plan to install a Wien filter. If the velocity of a certain ion satisfies the condition $v = \frac{E}{B}$, the ion is not deflected by the filter. In other words, this filter is in principle a velocity filter. In our experiment, every ion possesses almost the same kinetic energy. Thus, we can operate a Wien filter as a mass separator. The ion transportation parameters must be optimized again when the Wien filter is installed.

Fr trapping experiment for the precise EDM measurement has been prepared at CYRIC. We achieved Fr transportation in the efficiency of 18%. In the next step, we will install a Wien filter to remove the background current. To increase the efficiency of Fr trapping in MOT, a pure Fr ion beam is desired. A Wien filter will improve the purity of the ion beam.

The authors would like to thank the staffs of CYRIC machine group for their generous cooperation during our experiments. This experiment was mostly supported by Grants-in-Aid for Scientific Research (Nos. 21104005 and 21244026).

References

1) Kawamura H. *et al.*, *Nucl. Instrum. Methods Phys. Res.* B **317** (2013) 582.
2) Mukherjee D., Sahoo B. K., Nataraj H. S., Das B. P., *J. Phys. Chem.* A **113** (2009) 12549.
3) Manura D. J., and Dahl D. A., *SIMION 8.0 User Manual. Scientific Instrument Services*, USA 2007.

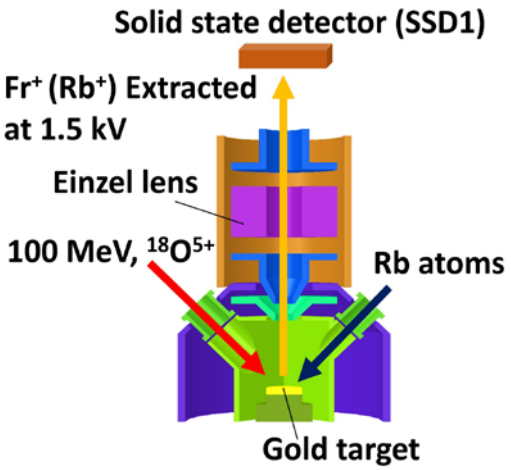

Figure 1. Thermal ionizer.

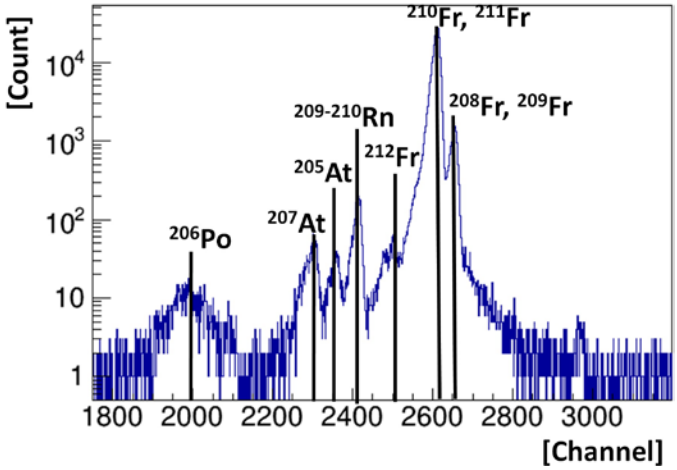

Figure 2. Typical α decay spectrum detected by SSD1.

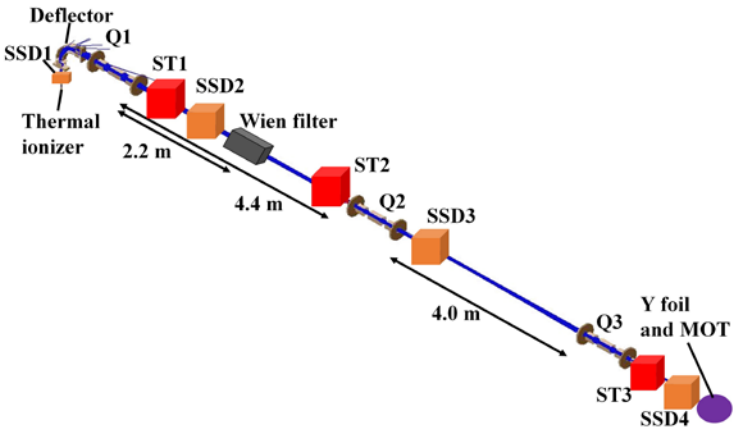

Figure 3. Fr beamline designed by SIMION including a deflector, quadrupole triplets (Q1, Q2, and Q3), steerers (ST1, ST2 and ST3). Solid state detectors are installed at 4 places in the beamline (SSD1-SSD4). We plan to install a Wien filter at the middle of Q1 and Q2.

II. 7. The Upgrade of the Ion and Neutron Irradiation System to Investigate the Soft Error of Integrated Circuit Systems

Sakemi Y.[1], Itoh M.[1], Ando T.[1], Aoki T.[1], Arikawa H.[1], Ezure S.[1], Harada K.[1], Hayamizu T.[1], Inoue T.[1,2], Ishikawa T.[1], Kato K.[1], Kawamura H.[1,2], and Uchiyama A.[1]

[1]*Cyclotron and Radioisotope Center, Tohoku University*
[2]*Frontier Research Institute for Interdisciplinary Sciences, Tohoku University*

A high-intensity fast neutron beam facility in CYRIC has been developed at the straight beam line (32 course) from the K = 110 MeV AVF cyclotron since 2004. This course is used for the cross section measurement of the nuclear physics, testing of semiconductors for single-event effects, and dosimetry development (Fig. 1). The AVF cyclotron can provide the proton beam with an energy range from 14 to 80 MeV at present. Figure 1 shows the schematic view of the neutron source. The quasi-monoenergetic neutron beam is produced by using the ^{7}Li(p,n)^{7}Be reaction. The primary proton beam is bombarded to the water-cooled production (Li) target. After penetrating the target, the proton beam is bent in the clearing magnet by 25° and stopped in the water-cooled beam dump which consists of a carbon block shielded by copper and iron blocks. The typical neutron beam intensity is about 10^{10} n/sr/sec/uA with a beam spread of about 5% for the beam energy and ± 2° for the horizontal and vertical directions. The neutron beam is collimated by iron blocks of 595 mm thick and sufficiently low background at the off-axis position. The available flux of the neutron beam is about 10^{6} n/cm^{2}/sec/uA at the sample position which is located at about 1.2 m downstream of the production target. The thermal neutron flux at the sample position is about 2×10^{4} n/cm^{2}/s, which was measured by a foil activation method combined with imaging plate.

The samples which are irradiated by the neutron to study the radiation damage of the integrated circuit system and many kinds of memory and CPU devices are set in front of the flange to extract the neuron beam. The integrated circuit system has many components which have each functions such as the SRAM, DRAM, FPGA, and many other functioned ICs, and we need to irradiate the neutron beam to each component to check which device

has effect again the radiation, and we can know the radiation damage mechanism in more detail by studying the position dependence of the soft error or radiation damage. Then, to realize the efficient experiment for the radiation damage, we developed the remote movable table to control the sample position by the support from Ministry of Economy, Trade and Industry. We can control the irradiation positions remotely and can monitor the soft error rate with any combination of the experimental parameters such as the beam position, beam intensity etc. The installation is ready now, and will be operated from next year.

Figure 2 shows a typical energy spectrum of the neutron beam at 65 MeV which was produced by 70 MeV protons. The thickness of the Li target was 9.1 mm. The energy spectrum was measured by the time of flight (TOF) method at 7.37 m downstream of the Li target. The energy spread of the neutron beam was 4 MeV which was included the time spread of the primary beam of 1.6 ns, the energy loss difference due to the thick Li target, and so on. The ratio of peak area to the total fast-neutron flux is about 0.4. The detection system of the fast neutron consists of a liquid scintillator of NE213 type with the size of 140 mm (diameter) × 100 mm (thickness), a 5 inch photomultiplier tube, HAMAMATSU H6527, which were assembled by OHYO-KOKEN cooperation, and a CAMAC data acquisition (DAQ) system. The irradiation room is a narrow room which size is 1.8 m (W) × 10 m (L) × 5 m (H). The irradiation sample can be placed at 1.2 m downstream of the Li target, as shown in Fig. 1. The spot size of the neutron beam is about 84 mm (horizontal) ×84 mm (vertical) at that point. The flux of the neutron beam can be varied from about a few hundreds n/sec to 3×10^{10} n/sr/sec. The largest amount of the accumulated flux in one experiment was about 5×10^{11} n/cm^2 for the practical irradiation time of 50 hours. The flux of the neutron beam is monitored by a primary beam current in the beam dump and a NE102A plastic scintillator with the size of 100 mm (diameter) × 1 mm (thickness) during the irradiation experiment. This facility has been listed as one of the high intensity fast neutron field facility with quasi-monoenergetic beam at EURADOS[1)].

Reference

1) EURADOS (European Radiation Dosimetry) Report 2013-02 “High-energy quasi-monoenergetic neutron fields”

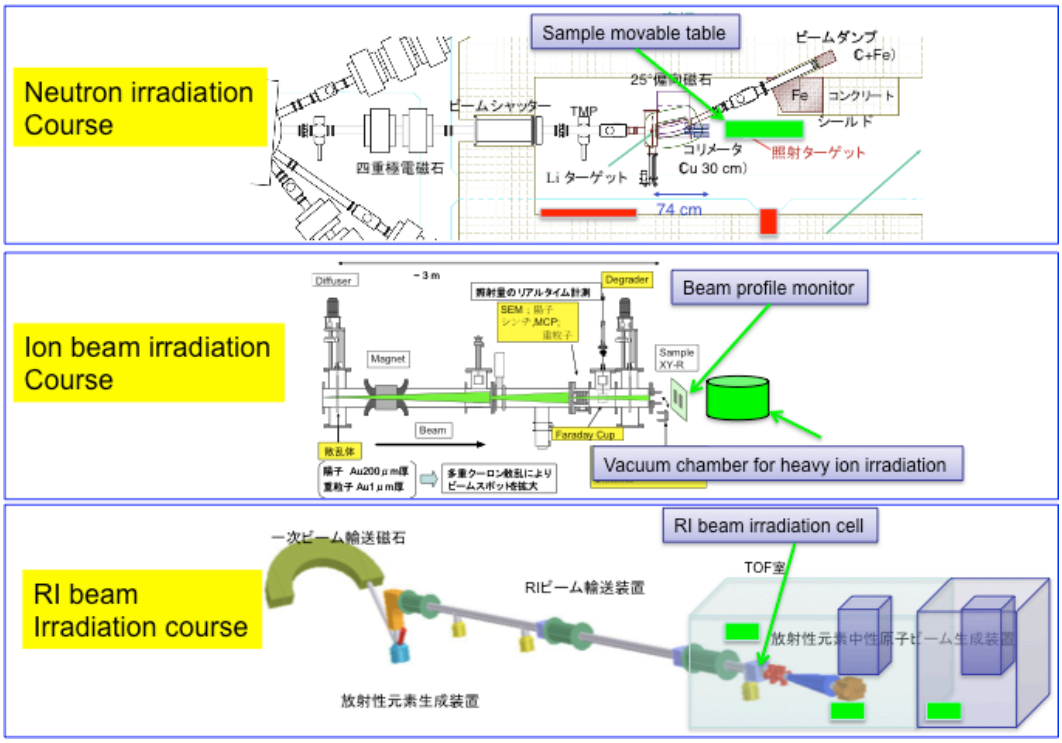

Figure 1. Overview of the setups of irradiation system of neutron (up) at 32 course, ion (middle) at 33 course, and RI beam (down) at 51 course.

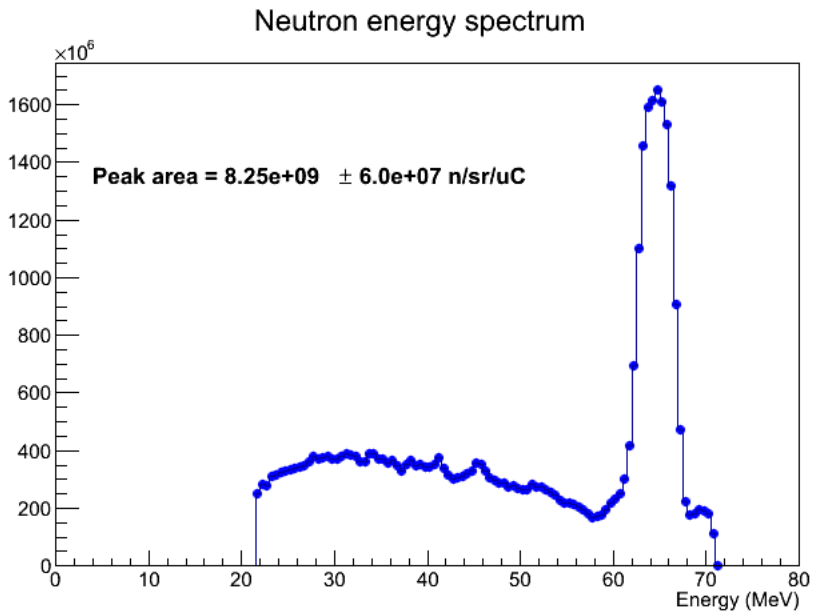

Figure 2. A typical energy spectrum of the neutron beam at 65 MeV. The neutron flux of a peak area from 58 to 68 MeV is 8.25×10^{9} neutrons/sr/μC. The ratio of the peak area to the total fast neutrons is about 0.4. The tail at around 70 MeV is attributed to the flame overlap due to the cyclotron RF cycle.

III. NUCLEAR ENGINEERING

III. 1. Evaluation of Long-Term Stability of TlBr Detectors for the Nuclear Spent Fuel Reprocessing Plant

Kimura N.[1,2], Hitomi K.[2], Kim S.-Y.[1], and Ishii K.[1]

[1]Graduate School of Engineering, Tohoku University
[2]Japan Nuclear Fuel Limited.

Introduction

The nuclear spent fuel reprocessing facilities in Rokkasyo, Aomori are the facilities which separate reusable uranium and plutonium from nuclear spent fuels coming from the nuclear power plants of the whole country. The extracted uranium and plutonium are reused as nuclear fuels at nuclear power plants. The remaining wastes including hulls of spent fuels and fission products are kept with drums and are vitrified, respectively[1)].

In order to extract uranium and plutonium from nuclear spent fuels, they are sheared about 3 cm in length by the shearing machine, then dissolved with hot nitric acid about 90 ºC in the dissolver. The fuel pellets dissolve in nitric acid. However, the hulls do not dissolve. Therefore, the hulls are evacuated from the dissolver and are filled in the solid waste drums. In order to confirm that all pellets are dissolved, measurements of gamma-ray spectra of the hulls are performed. The amount of undissolved fuels is determined by measuring gamma-rays (662 keV) from ^{137}Cs.

Currently, a germanium (Ge) semiconductor detector is used to measure the gamma-rays of hulls in the Rokkasyo reprocessing plants. The Ge semiconductor detector exhibits excellent energy resolutions (0.25% FWHM at 662 keV). However cooling by liquid nitrogen is needed during the operation of the detector because its energy band gap is narrow (0.67 eV). Since reduction of the operation cost and the size of detector systems are required, there is a need for developing semiconductor detectors without cooling by liquid nitrogen. It is possible to install gamma-ray detectors in various places of the reprocessing process by using compact gamma-ray detector systems without cooling by liquid nitrogen.

Thallium bromide (TlBr) is a promising material for fabrication of radiation detectors without cooling by liquid nitrogen. Average atomic number of TlBr is high (Tl :

81, Br : 35) and the density is also high (7.56 g/cm^3). The energy band gap is wide (2.68 eV). Studies of TlBr detector fabrication were described by numerous researchers[2-5]. Table 1 summarizes the properties of radiation detector materials.

Fabrication of TlBr radiation detectors

The TlBr crystal used for detector fabrication was 5 mm×5 mm×5 mm. The detector had 4 pixelated anodes and a planar cathode. The cathode and one of the pixelated anode were connected to charge sensitive preamplifiers (Amptek A250). In order to improve the stability of the detector, the TlBr crystal was cooled to -10 ºC by a Peltier element. The fabricated TlBr detector is shown in Figs. 1 and 2.

Evaluation of TlBr radiation detectors

Energy spectra for ^{137}Cs (about 1 MBq) were obtained by the fabricated TlBr detector. An ORTEC 462 spectroscopy amplifier was used for the measurement. The bias voltage for the TlBr detector was 500 V. A measured spectrum is shown in the Fig. 3. The FWHM of the peak at 662 keV was 3.0%. The peak to Compton ratio was 5.2.

In consideration of the use of the detector in the plants, a long-term stability test was performed. Polarization phenomena have been the most serious problem for TlBr detectors. However, the polarization phenomena have been overcome by using Tl electrodes[6,7]. The detector was operated continuously for approximately one month. As shown in Figs. 4 and 5, the detector operated stably with no significant change in the peak position and the energy resolution.

Conclusion

A TlBr detector system was fabricated in this study. The detector exhibited good energy resolutions without liquid nitrogen cooling. The detector showed stable performance for more than one month.

References

1) Japan Nuclear Fuel Limited., Designation for Application of Reprocessing Business (2007).
2) Rahman I.U., Fisher W.A., Hofstadter R., Jing S., *Nucl. Instr. and Meth.* **A261** (1987) 427.
3) Shah K.S, Lund J.C., Olschner F., Moy L., Squillante M.R., *IEEE Trans. Nucl. Sci.* **36** (1989) 199.
4) Hitomi K., Muroi O., Shoji T., Suehiro T., Hiratate Y., *Nucl. Instr. and Meth.* **A436** (1999) 160.
5) Churilov A.V., Ciampi G., Kim H., Cirignano L.J., Higgins W.M., Olschner F., Shah K.S., *IEEE Trans. Nucl. Sci.* **56** (2009) 1875.
6) Hitomi K., Shoji T., Niizeki Y., *Nucl. Instr. and Meth.* **A585** (2008) 102.

7) Hitomi K., Kikuchi Y., Shoji T., Ishii K., *IEEE Trans. Nucl. Sci.* **56** (2009).
8) Knoll G.F., *Radiation Detection and Measurement Fourth Edition* (2010).

Table 1. Materials for radiation detectors[8].

Materials	Atomic Number	Density [g/cm^3]	Band gap [eV]
Si	12	2.33	1.12
Ge	32	5.33 (77[K])	0.72 (77 [K])
CdTe	48/52	6.06	1.52
TlBr	81/35	7.56	2.68

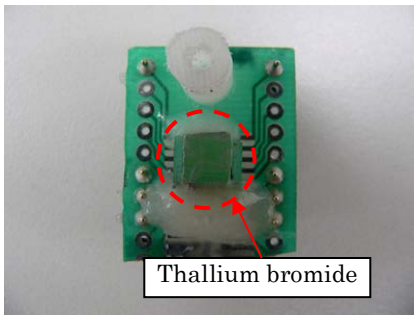

Figure 1. TlBr detector.

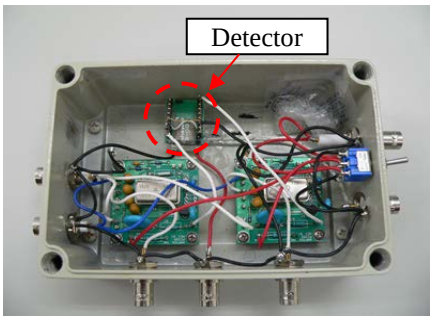

Figure 2. Fabricated TlBr detector system.

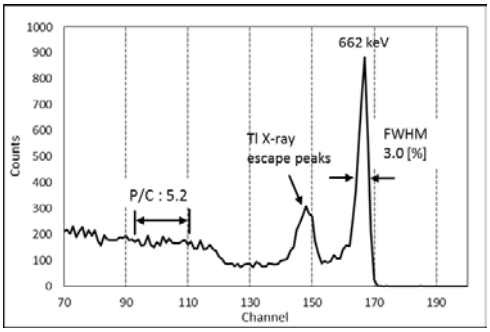

Figure 3. Measured spectrum of ^{137}Cs.

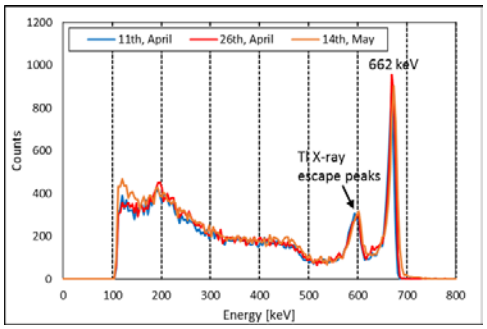

Figure 4. ^{137}Cs spectra obtained from a TlBr detector.

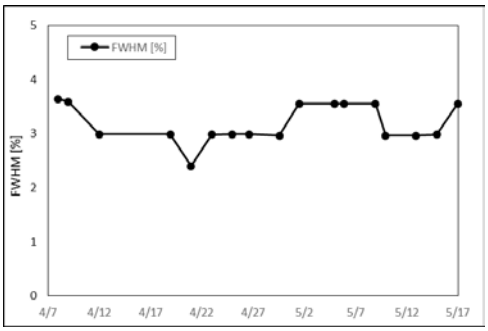

Figure 5. Time variation of FWHM for the 662 keV peak obtained from a TlBr detector.

IV. NUCLEAR MEDICAL ENGINEERING

IV. 1. A Proton Beam Monitor Based on a Micro Pattern Gaseous Detector Using Glass-GEM

Terakawa A.[1], Ishii K.[1], Matsuyama S.[1], Masuyama M.[1], Kaneta S.[1], Kubo R.[1], Matsuyama T.[1], Sato T.[1], Sakemi Y.[2], and Fujiwara T.[3]

[1]Department of Quantum Science and Energy Engineering, Tohoku University
[2]Cyclotron and Radioisotope Center, Tohoku University
[3]Graduate School of Engineering, The University of Tokyo

Recently, gas electron multiplier (GEM) technology[1)] has been studied in various fields to develop a new type of a gas detector system and shown significant advantages over a multi-wire proportional chamber such as the excellent special resolution and stable operation at higher counting rate. It is expected that GEM technology meets requirements for monitoring of the scanned-beam parameters in the charged particle therapy.

The aims of this study were to develop a micro-pattern gaseous detector based on GEM technology (GEM detector) as a new transmission beam monitor for charged particle therapy and to assess its feasibility on the basis of a performance test using a proton beam by evaluating two dimensional intensity distribution of the beam.

Figure 1 shows the GEM detector developed in this work. The GEM detector consists of a cathode plate, a glass-GEM plate, and two window foils, and filled with a gas mixture (Ne 90% + CF_4 10%). The advantage of the glass-GEM is higher gas gain compared to conventional GEM using organic substance as a insulator. In this work we used the glass-GEM plate (Hoya CO. LTD., Japan) made of a 680 μm thick glass sandwiched between 9 μm thick cupper electrodes, and has holes in 140 μm in diameter with 280 μm distance. When electrons induced by an incident proton beam are multiplied by the GEM, scintillation is generated from the Ne-CF_4 gas and detected with a CCD camera. It is possible to evaluate a two-dimensional (2D) beam-intensity distribution using the scintillation. The GEM used in this work has an active area of 100×100 mm. The gas gain of the glass-GEM has been checked with X-ray (^{55}Fe) and alpha (^{241}Am) sources (Fig. 2).

In order to evaluate characteristics of the GEM detector for beam monitoring, the experiment was performed using an 80-MeV proton beam provided from the K=110-MeV

AVF cyclotron at CYRIC. The GEM detector was placed in the horizontal irradiation system[2]. The proton beam from the cyclotron was delivered to the GEM detector. The 2D intensity distribution of the incident beam at the GEM monitor was also measured using an Imagine Plate (IP) (Fuji Photo Film Co., Ltd) for comparison.

Figure 3 shows the comparison of the lateral bean intensity distributions between the GEM detector and IP. The beam intensity distribution measured with the GEM detector is in good agreement with those of IP. The experimental result has demonstrated that the GEM-based detector can measure the beam position and the lateral beam-profile simultaneously. Therefore, if we replace the conventional multiple-detectors for monitoring beam parameters with a single GEM-based transmission monitor, it is possible to reduce the multiple scattering and struggling effects caused by the multiple-detectors.

References

1) Sauli F., *Nucl. Instrm and Meth.* A **386** (1997) 531.
2) Terakawa A., et al., *Proc. of the 16th Pacific Basin Nuclear Conference (16PBNC), Oct. 13-18, 2008, Aomori, Japan*, PapaerID P16P1378, 1.

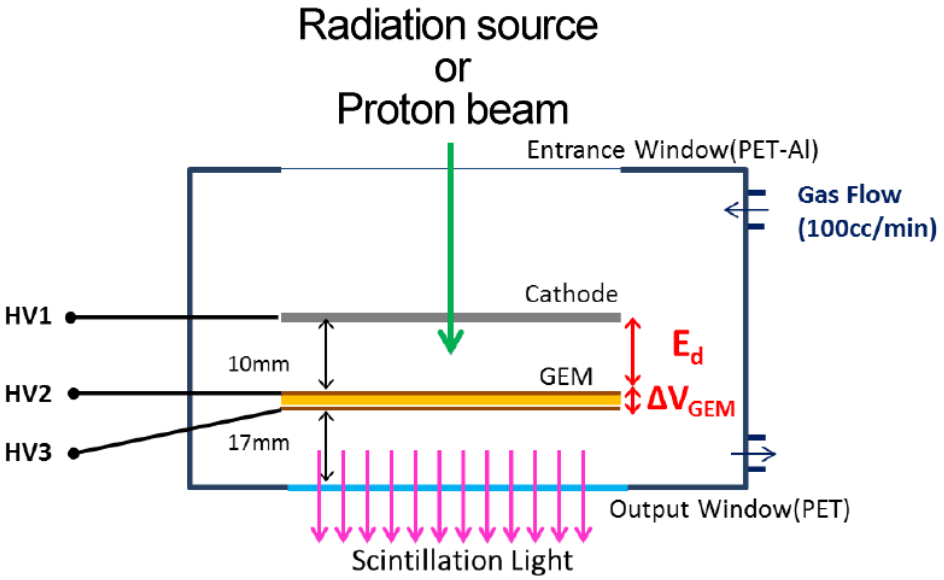

Figure 1. Micro-pattern gaseous detector based on gas electron multiplier technology developed as a prototype transmission beam monitor for charged particle therapy. ^{55}Fe and ^{241}Am were used as radiation sources to measure the gas gain (The ^{241}Am source was placed between the cathode and GEM.).

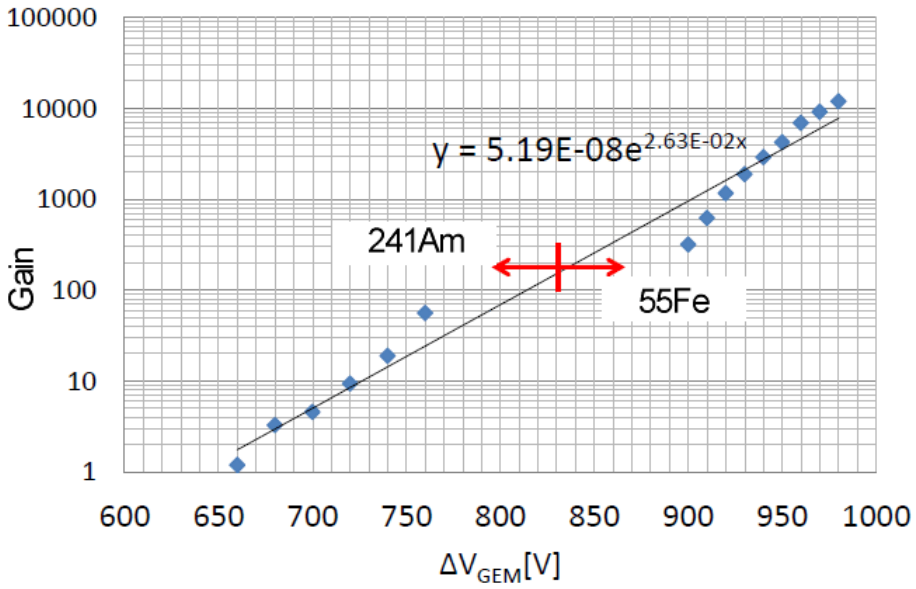

Figure 2. Gas gain of the single glass-GEM as a function of ΔV_{GEM} evaluated with ^{55}Fe (5.9 keV-X-ray) and ^{241}Am alpha sources.

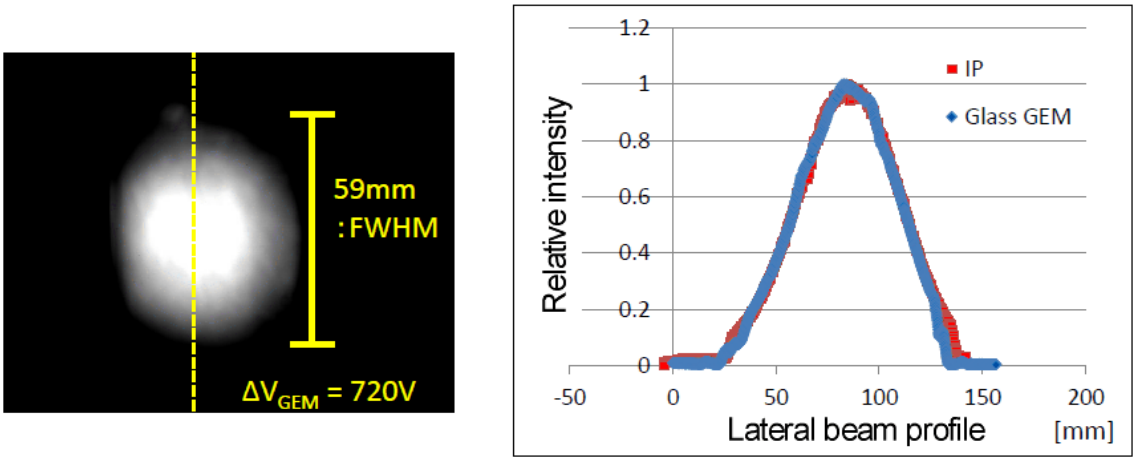

Figure 3. Scintillation due to proton beam irradiation from the glass-GEM and comparison of the lateral beam profile between the GEM monitor and IP.

V. PIXE AND ENVIRONMENTAL ANALYSIS

V. 1. Improvement of Energy Stability of the Tohoku Dynamitron Accelerator

Matsuyama S., Ishii K., Fujisawa M., Nagaya T., Watanabe K., Terakawa A., Kikuchi Y., Fujiwara M., Sugai H., Karahashi M., Nozawa Y., Yamauchi S., and Ishiya M.

Department of Quantum Science and Energy Engineering, Tohoku University

Introduction

The microbeam system at Tohoku University has been applied to various fields[1-7]. Recently, higher spatial resolution down to several hundred nm and higher beam current with a several μm resolution is required and a triplet lens system was newly installed. While the triplet system has larger demagnification, chromatic aberration is much larger than the doublet system. To get best performance of the high demagnification system, improvement of energy resolution of the accelerator is required. In the previous studies, adjusting the feed back system was carried out and the voltage ripple decreased to ±1 keV. While this adjustment improved the beam current stability at the microbeam target, energy resolution is not sufficient for the larger magnification system. In this study, various source of the voltage ripple of the accelerator was investigated and reduction of voltage ripple was carried out.

High Voltage System of the Tohoku Dynamitron Accelerator

High voltage generator of the Dynamitron accelerator is a parallel-fed, series-cascaded rectifier system (Shenkel type high voltage generator)[8]. Figure 1 shows schematic diagram of the high voltage generator and control system of the Tohoku Dynamitron Accelerator. The L-C tank circuit consists of transformer (toroidal coil) and capacitances between corona rings, tank vessel and RF electrodes (upper and lower dees). The oscillator is a tuned anode and untuned grid circuit. RF voltage from the dees is capacitively coupled into the cascade rectifier stages. Ninety six stages are used in our accelerator. Positive grid feedback to maintain oscillation of ca. 120 kHz is provided by a voltage pick-up from the grid feedback plate located between the upper dee and accelerator tank vessel. The maximum voltage of the accelerator is 4.5 MV and the maximum beam

current is 3 mA. Voltage stability is better than 2 kV_{p-p}. Vacuum rectifier tubes (Kenetron) had been used as rectifier and were replaced by diodes made by Origin Electric Corporation. High voltage of the terminal is controlled by varying the RF voltage which is varied by adjusting a plate voltage of the triodes (5771s). The plate voltage was controlled by a high voltage DC power supply. High voltage DC power supply for the RF oscillator is stabilized by a fast feed back loop and a precise DC amplifier (inner loop amplifier). The high voltage is further stabilized by a feedback system (auto regulator). A proportional integration (PI) circuit is used to stabilize the high voltage. The PI controller acts on the error signal from the comparison of the set reference voltage and the voltage generated on the precise register connected to the resister network (high voltage divider, HVD) which is connected from the high voltage terminal and ground. The third feed back loop is efficient for low frequency fluctuation less than several Hz. In the previous study, feedback response was adjusted by measuring the beam fluctuation on target[9]. However, higher frequency ripple could not be measured. In this study, a capacitive pick-off (CPO) unit is newly installed to measure the voltage ripple. The Dynamitron accelerator has unpowered dee (grounded dee) which consists of two semicircular plates and circular flat plate at the end and covers high voltage terminal as shown in Fig. 1. The CPO plate of 355 mm in diameter is mounted on the center of the plate at the end. Distance between the CPO plate and the high voltage terminal is 685 mm. Cascade generator like Dynamitron has many ripple components. Therefore CPO has to measure wide frequency region, at least up to oscillation frequency. If CPO output is directly measure by an oscilloscope, frequency higher than 100Hz can be measured with a sensitivity of 150 mV/kV. If CPO output is measured with amplifier, frequency less than 1 kHz can be measured with a sensitivity of 8 V/kV. Frequency less than 1Hz, we can measure the ripple with HVD current.

Improvement of Voltage Stability

Voltage ripple of the Dynamitron accelerator was measured with CPO with and without an amplifier. Main components of the ripple are 120 kHz and 50 Hz. Peak to Peak voltages (V_{p-p}) of 120 kHz and 50 Hz components were ca. 2 kV and 1.5 kV at a terminal voltage of 2 MV with no beam load. Loading current without beam is a sum of HVD current and beam tube divider resister current which determines voltage of the acceleration tube and is more than 100 μA. Since beam current in many application is in an order of several tenth μA, voltage ripple was not increase drastically with beam loading. RF

modulation of the oscillator is superposed on the high voltage. The terminal ripple of the oscillation frequency has two origins, one is the inherent ripple of the cascade rectifier and the other is related to asymmetry in the L-C circuit composed of the toroidal coils and dees[8,10]. The inherent voltage ripple is estimated to be 20 V_{p-p}, this larger ripple stems from asymmetry of L-C circuit. The asymmetry comes from the unbalance of the capacitances related to the upper dee and the lower dee. The grid feedback signal is picked up from the grid feedback plate located between the upper dee and the vessel. To compensate the difference of capacitance[8,10], a balance plate with same shape and size is installed between the lower dee and the tank. The balance plate can be moved from outside and adjust the capacitance of the lower dee. CPO output of 120 kHz component decreases corresponding to lowering the balance plate, but not eliminated. It is apparent that the capacitance of the upper dee is too small to compensate the capacitance by the balance plate motion. To increase the capacitance of the upper dee, additional balance plates were attached on the upper dee. Figure 2 shows the voltage ripple at a terminal voltage of 2 MV. By adding the additional capacitance on the upper dee, voltage ripple was reduced down to 1 kV_{p-p} even at a balance plate position of upper limit. The ripple voltage was further reduced down to 200 V_{p-p} at the lowest balance plate position. Since the lowest value was obtained in the lowest balance plate position, the asymmetry is still remaining. We are planning to add more capacitance to the upper dee.

The 50 Hz component is apparently related to the power line frequency. The 50 Hz component increased with feedback gain and decreased without feedback. It is apparent that power line noise mixes with HVD current. In the previous study, we reported that the increase of feedback gain improved stability of target beam currents[9]. While the increase of ripple improves target current stability, beam intensity might decrease. To reduce the 50 Hz component, a notch filter was installed between the auto regulator and the inner loop amplifier. After the modification, voltage ripple of the low frequency components less than 1 kHz were reduced down to 400 V_{p-p}. While peak to peak voltage is 400 V, averaged voltage ripple distribution is 150 V FWHM as shown in Fig. 3. Since CPO signal is affected by the noise from cooling fans in the vessel and is around 300 V equivalent voltage, ripple of terminal voltage for lower frequency is much less.

Conclusions

The microbeam analysis system installed at Dynamitron laboratory has applied to various fields. To obtain higher spatial resolution down to several hundred nm and higher

beam current with a several μm resolution, update to a triplet lens system which has larger demagnification by adding a quadrupole lens was carried out. Since the system has higher demagnification, effect on chromatic aberration is larger and energy resolution should be improved. To get higher energy resolution, various source of the voltage ripple of the accelerator was investigated and minimization of voltage ripple was carried out. Voltage ripple of the accelerator for low frequency components were reduced less than 150 V. However, voltage ripple of 120 kHz components was 200 V_{p-p} since the perfect symmetrization was not achieved yet. It will be achieved by adding the additional capacitance on the upper dee.

Acknowledgement

The authors would like to thank Prof. Art Haberal, University at Albany-SUNY, for his valuable suggestion and advice in reducing high voltage ripple. This study was partly supported by Grant-in-Aid for Scientific Research, (B) No. 23360419, 13852017, Ministry of Education, Culture, Sports, Science and Technology (MEXT) and Grant-in-Aid for Challenging Exploratory Research Grant No. 23656583, Japan Society for the Promotion of Science (JSPS). This study was also supported Japan-France Integrated Action Program (SAKURA).

References

1) Matsuyama S, Ishii K, Yamazaki H, et al., *Nucl Instr Meth* B **210** (2003) 59.
2) Matsuyama S, Ishii K, Yamazaki H, et al., *Int J PIXE* **14** (2004) 1.
3) Matsuyama S, Ishii K, Abe S, et al., *Int J. PIXE* **15** (2005) 41.
4) Ishii K, Matsuyama S, Yamazaki H, *Int J PIXE* **15** (2005) 111.
5) Ishii K, Matsuyama S, Yamazaki H, et al., *Nucl Instr Meth* B **249** (2006) 726.
6) Ishii K, Matsuyama S, Watanabe Y, et al., *Nucl. Instr. and Meth* A **571** (2007) 64.
7) Matsuyama S, Ishii K, Yamazaki H, et al., *Nucl Instr Meth* B **260** (2007) 55.
8) Tompson CC, Clerand MR, *IEEE Trans Nucl Sci NS-16* (1969) 113.
9) Matsuyama S, Ishii K, Fujisawa, M et al., *Nucl Instr Meth* B **267** (2009) 2060.
10) Wustenbecker S, Becker HW, Rolfs C, et al., *Nucl Instr Meth* A **256** (1987) 9.

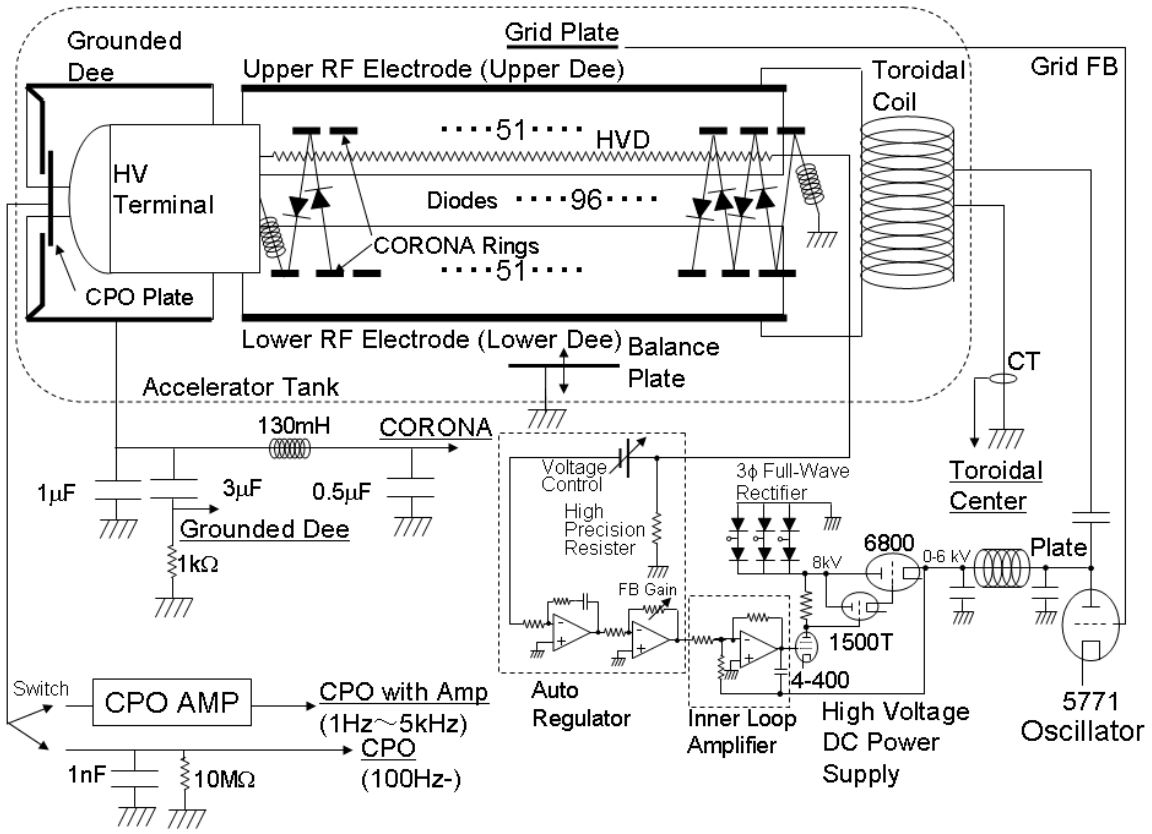

Figure 1. Schematic Diagram of the High Voltage Generator and Control System.

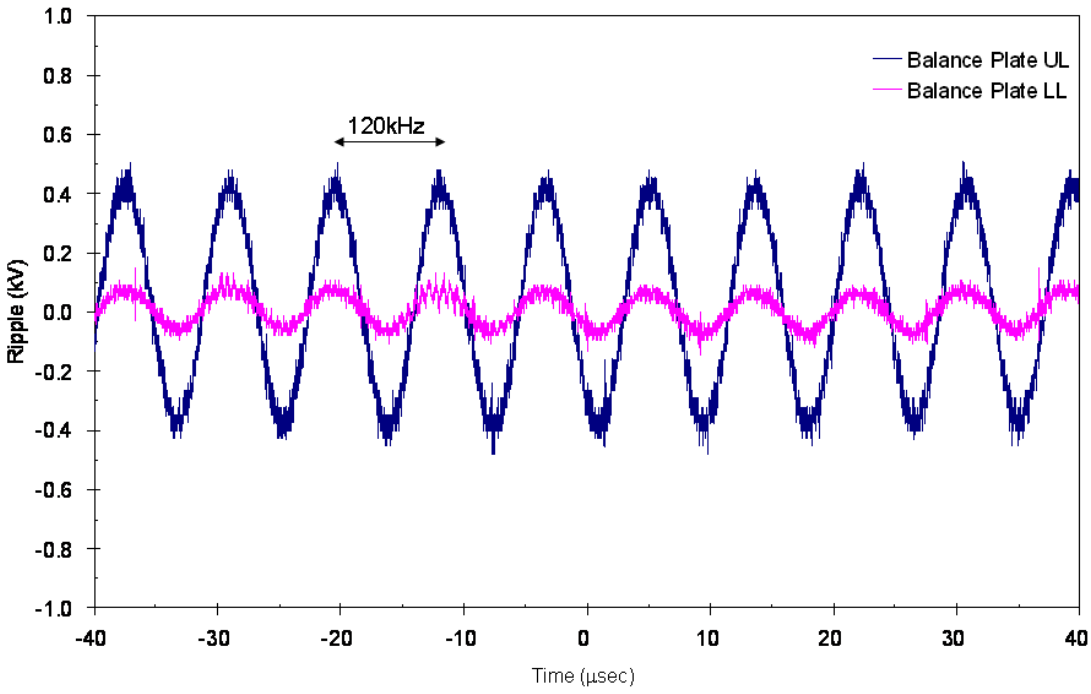

Fig. 2. Measured Voltage ripple at a Terminal Voltage of 2MV for Balance Plate Position of Upper Limit and Lower limit.

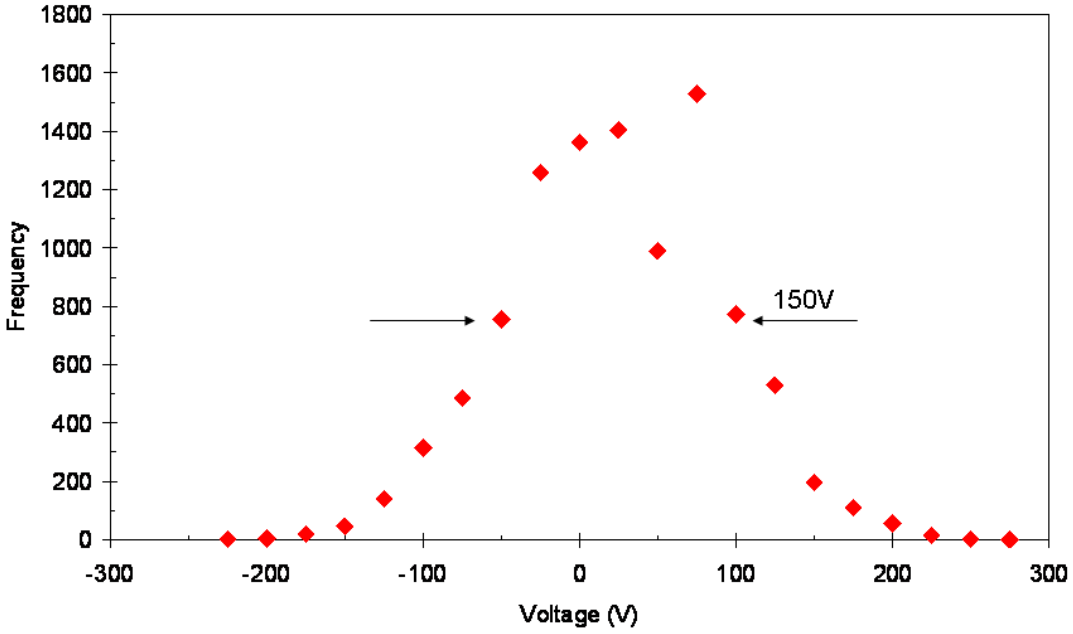

Figure 3. Voltage Ripple Distribution for the ripple frequency less than 5 kHz.

V. 2. Improvement of the Tohoku Microbeam System

Matsuyama S., Ishii K., Watanabe K., Terakawa A., Kikuchi Y., Fujiwara M., Sugai H., Karahashi M., Nozawa Y., Yamauchi S., Fujisawa M., Ishiya M., and Nagaya T.

Department of Quantum Science and Energy Engineering, Tohoku University

Introduction

The microbeam system installed at Tohoku University for biological application has been operated for more than ten years[1)] and has been applied to simultaneous in-air/in-vacuum PIXE, RBS, SE, and STIM analyses[2-4)], and 3D PIXE-μ-CT[5-7)]. The Tohoku microbeam system comprises a quadrupole doublet and three slit systems. A beam spot of 0.4 × 0.4 μm^2 at a beam current of several tens of pA has been produced[8)]. In our set-up, μ-PIXE/RBS analyses demand beam currents of ca. 100 pA, which restricts the spatial resolution to around 1 × 1 μm^2. Recently, higher spatial resolution down to several hundred nm is required in e.g., aerosol studies. In *in-vivo* 3D imaging using 3D PIXE-μ-CT, the long measurement time of several hours weakened the specimen. Thus beam currents higher than ca. 1 nA with a several μm resolution are required in 3D PIXE-μ-CT applications.

To meet these requirements, update to a triplet lens system which has larger demagnification by adding a quadrupole lens was planned and designed. The triplet system can arrange both standard and separated triplet configuration. In the separate geometry, demagnification factors are more than 220 and 70 for horizontal and vertical planes, respectively, which are seven times higher than those of the previous doublet system.

Microbeam System

The Tohoku microbeam system was designed to achieve sub-micrometer beam sizes and was developed in collaboration with Tokin Machinery Corp.[1)]. Main components of the Tohoku microbeam system are mounted on the rigid support. Since the microbeam system was designed considering extensibility, introducing of triplet lens system could be done with minimum modification. The lens is almost the same deign as the previously used lenses

except for the cancellation of excitation current[4,8]. While contamination fields of the previous lenses were less than 0.05%, the new lenses were designed to cancel the excitation current even in the upper part to reduce the contamination field as low as possible. The new lenses are mounted on the fine linear stage as shown in Fig. 1. The total length of the fine linear stage is ca. 1 m. Spacing between lenses can be adjusted between 700 mm to 50 mm. Once lens is aligned at one position, the lens can move without another alignment.

Beam properties were calculated using the raytracing software package "WinTRAX"[9]. In the triplet arrangement, the 1st quadrupole lens (Q1) and the 3rd lens (Q3) focus the beam on the same plane and the 2nd lens (Q2) focuses on the perpendicular plane (divergence-convergence-divergence; DCD or convergence- divergence-divergence; CDC). The demagnification factors are 25.4 and 65.7 for horizontal and vertical planes, respectively, with the 1st and 3rd lenses coupled in excitation. Calculated beam spot size is $0.7 \times 0.5\ \mu m^2$. Chromatic aberration coefficients are 846 and 422 μm/mrad/%ΔP/P. Spherical aberration coefficients of $\langle x|\theta^3\rangle$, $\langle x|\theta^2\phi\rangle$, $\langle y|\phi^3\rangle$ and $\langle x|\theta\phi^2\rangle$ calculated using the rectangular model are 362 126, 325 and 155 μm/ $mrad^3$, respectively. Due to larger spherical and chromatic coefficients than those of the doublet system, beam size will be $4 \times 1.9\ \mu m^2$ at beam divergence of ± 0.2mrad. Beam broadening calculated from chromatic aberration coefficients is estimated to be 0.8 and 0.4 μm with a beam divergence of 0.2 mrad and it is reported that intensity of the beam which has larger divergence and large energy spread was very low[9]. It is apparent that beam spot size is mainly restricted by the effect of spherical aberration. Since the actual spherical aberration cross terms is smaller than those by rectangular model[9], measured beam spot size will be smaller than that by the calculation. Actually, in our previous doublet system, a beam spot size of $0.4 \times 0.4\ \mu m^2$ was obtained at an object size of $30 \times 10\ \mu m^2$, beam divergence of ±0.2mrad and $\Delta E/E=10^{-4}$. Calculated beam spot size using the rectangular model is $0.5 \times 0.7\ \mu m^2$ and is large than the measured one. Therefore, better result will be obtained.

In the separated triplet configuration, the demagnification factors are further improved to 74.4 and 228 for horizontal and vertical planes, respectively. Chromatic aberration coefficients are 1381 and 856 μm/mrad/%ΔP/P. The spherical aberration coefficients of $\langle x|\theta^3\rangle$, $\langle x|\theta^2\phi\rangle$, $\langle y|\phi^3\rangle$ and $\langle x|\theta\phi^2\rangle$ are 2772, 945, 2946 and 2148 μm/ $mrad^3$, respectively. These values are ten times larger than those of standard triplet system. Calculated beam spot size was $4.2 \times 2.5\ \mu m^2$ at an object size of $120 \times 30\ \mu m^2$, beam divergence of ±0.1 mrad and $\Delta E/E=10^{-4}$, due to larger spherical aberration. To get better

resolution, beam divergence into the quadrupole should be reduced. By reducing the divergence to ±0.05 mrad, beam spot size could be reduced down to 0.7 × 0.5 μm^2.

Preliminary Result of the Microbeam System

The beam spot size was measured by beam scanning across mesh samples, and measuring X-rays. Figure 2 (a) shows elemental maps of Ni mesh (2000lines / inch) using standard triplet configuration. This image was obtained with an object size of 15 × 30 μm^2 and divergence of ±0.2 mrad. Estimated beam size was ca. 4 × 2 μm^2 and was consistent with calculated one. The images was getting better by reducing with the beam divergence of ±0.1 mrad as shown in Fig. 2 (b). Estimated beam size was ca. 2 x 1 μm^2, which is worse than calculated one and than that obtained by the doublet system. While effect of spherical aberration is the largest component of beam broadening by the calculation, effect on chromatic aberration is also affects beam size. Both aberration of the triplet system are larger than those of the doublet system. We are now readjusting the whole system including the energy stability of the Dynamitron accelerator. After adjustment of the standard triplet configuration, separated configuration will be tested.

Conclusion

The microbeam analysis system installed at Tohoku University has applied to simultaneous in-air/in-vacuum PIXE, RBS, SE, and STIM analyses, and 3D PIXE-μ-CT for ten years. Update to a triplet lens system which has larger demagnification by adding a quadrupole lens was carried out to get higher spatial resolution down to several hundred nm and higher beam current with a several μm resolution. The system can arrange both standard and separate triplet configurations. The new triplet system did not achieve design goal. We are now readjusting the whole system including the energy stability of the Dynamitron accelerator.

Acknowledgements

This study was partly supported by Grant-in-Aid for Scientific Research, (B) No. 23360419, 13852017, Ministry of Education, Culture, Sports, Science and Technology (MEXT) and Grant-in-Aid for Challenging Exploratory Research Grant No. 23656583, Japan Society for the Promotion of Science (JSPS). This study was also supported Japan-France Integrated Action Program (SAKURA). The authors would like to thank Prof. G.W. Grime University of Surrey, for his valuable suggestion and advice in introducing WinTRAX.

References

1) Matsuyama S, Ishii K, Yamazaki H, et al., *Nucl Instr Meth* B **210** (2003) 59.
2) Matsuyama S, Ishii K, Yamazaki H, et al., *Int J PIXE* **14** (2004) 1.
3) Matsuyama S, Ishii K, Abe S, et al, *Int J PIXE* (2005) 41.
4) Matsuyama S, Ishii K, Tsuboi S, et al., *Int J PIXE* **21** (2011) 87.
5) Ishii K, Matsuyama S, Yamazaki H, et al., *Int J PIXE* **15** (2005) 111.
6) Ishii K, Matsuyama S, Yamazaki H, et al., *Nucl Instr Meth* B **249** (2006) 726.
7) Ishii K, Matsuyama S, Watanabe Y, et al., *Nucl Instr Meth* A **571** (2007) 64.
8) Matsuyama S, Ishii K, Yamazaki H, et al., *Nucl Instr Meth* B **260** (2007) 55.
9) Grime GW, *Nucl Instr Meth* B, to be published.

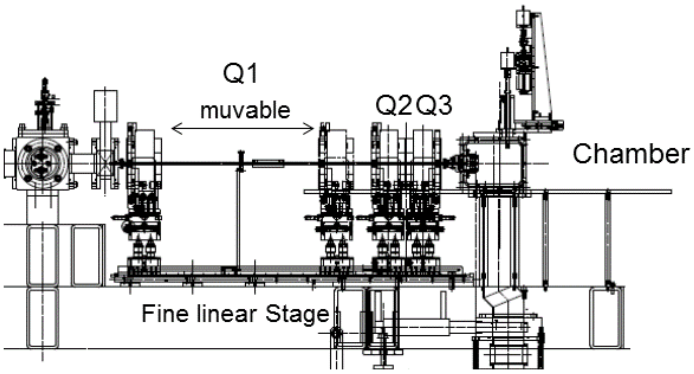

Figure 1. Layout of the triplet lens system.

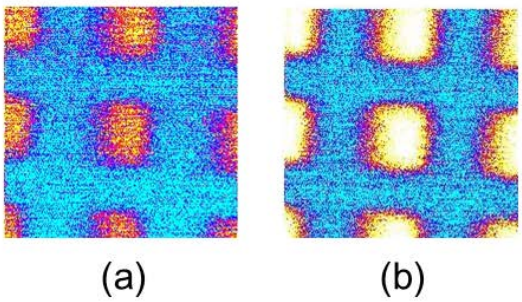

Figure 2. Elemental map of fine mesh grid (2000 lines/inch). (a) Ni mesh using standard triplet system for beam divergence of 0.2 mrad, and (b) Ni mesh using triplet system for beam divergence of 0.1 mrad.

V. 3. PIXE Analysis of Lentinula Edodes (Shiitake Mushroom)

Terakawa A., Ishii K., Matsuyama S., Kubo R., Matsuyama T., Hirakata H., Sato T., Inano K., Toyama S., Ito S., and Kasahara K.

Department of Quantum Science and Energy Engineering, Tohoku University

Mushrooms have the capability to accumulate radioactive cesium[1-4] because mushrooms collect a large amount of potassium as an essential element and also take the other alkali elements during uptake of potassium. Since the Fukushima nuclear accident, radioactive contaminated shiitake mushrooms (Lentinula edodes) have been found in Fukushima prefecture and its surrounding areas in east Japan because of uptake of radioactive cesiums from the logs exposed to the radioactive plume released at the nuclear accident. In this work we aimed to study relationships between concentrations of alkali elements in shiitake mushrooms and their radioactive cesium contamination based on particle-induced X-ray emission (PIXE) analysis.

Shiitake mushrooms were cultivated at Tohoku University with radio-contaminated hardwood logs used for shiitake cultivation in Iitate Village located about 30 km northwest of the nuclear power plant. Before shiitake mushroom cultivation, aqueous solutions of stable cesium carbonate and rubidium carbonate were sprayed onto the logs to evaluate concentration of alkali elements in shiitake mushrooms using PIXE analysis. The applied spray volume was determined so that the each concentration of cesium and rubidum in the bark (the surface of the hardwood logs) was approximately 300 μg/g. Two shiitake mushrooms were grown and gathered. In order to measure spatial distribution of radioactivity in the shiitake mushroom, an autoradiographic method was employed. We cut the raw mushroom samples and attached their cutting surface on an imaging plate (IP) (Fuji film Co., Ltd.). Exposure time was 36 h.

Spatial distribution in the sample was investigated by means of submilli-PIXE analysis at Fast Neutron Laboratory, Tohoku University. The sections of the samples were obtained by cutting the frozen tumors in a cryostat (-20^{o}C), and mounted on thick polycarbonate films. Thickness of the section was 250 μm. Elemental maps of the samples

were obtained from beam scanning with a 3-MeV proton pencil beam. X-rays from the sample were measured with two Si(Li) detectors to obtain low and high energy spectra separately. In addition, a Ge detector was used at just behind the target to increase X-ray yields so that elemental maps for rubidium in the sample can be obtained. The spot size of the proton beam was about 0.5 mm × 0.5 mm. The beam intensity was 2 nA on target.

Figure 1 shows cross sections of the shiitake mushroom indicating spatial distributions of radioactivity measured with the IP. It is found that radioactive cesium is not uniformly distributed and concentrates in the peripheral region of pileus of shiitake. Figure 2 shows shiitake samples for submilli-PIXE analysis. The shiitake mushroom was divided into five portions. The results of submilli-PIXE analysis was shown in Fig. 3. Elemental concentrations of potassium and rubidium in the peripheral region of pileus was higher than those in other parts. Although the spatial distribution of cesium could not be measured due to the low concentration, those of potassium and rubidium showed the same tendency as that of radioactive cesium measured with the IP. The experimental results suggest that shiitake mushrooms accumulate radioactive cesium in the same manner as potassium and rubidium, and rubidium can be used as an elemental tracer for radioactive cesium.

References

1) Battiston G. A., et al., *J. Environ. Radioactivity* **9** (1989) 53.
2) Kammerer L., et al., *J. Environ. Radioactivity* **23** (1994) 135.
3) Bem H., et al., *J. Radioanal. Nucl. Chem.*, 145 (1990) 39.
4) Shimizu M, Anzai I., *Journal of Oral Science* **43** (2001) 145.

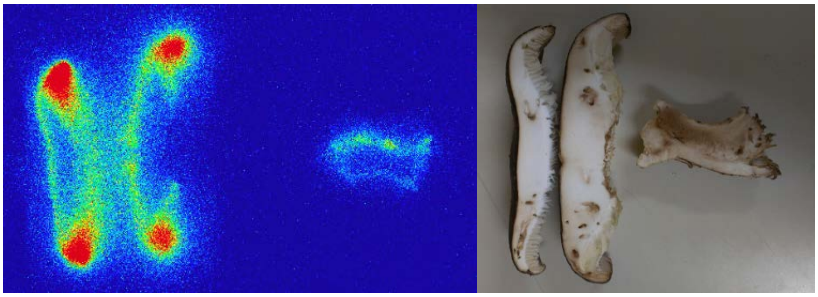

Figure 1. Spatial distribution of radioactive cesium in the shiitake mushroom measured with an imaging plate.

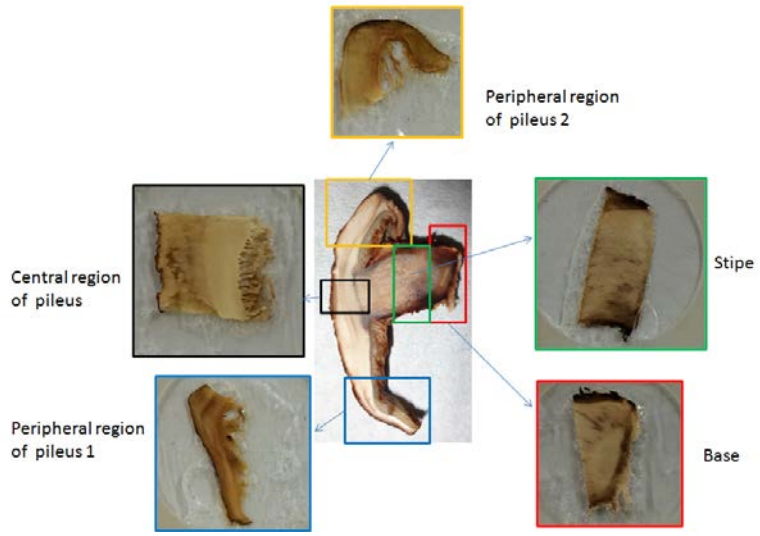

Figure 2. Shiitake samples for submilli-PIXE analysis. The shiitake samples was divided into five portions. Each thickness was 250 μm.

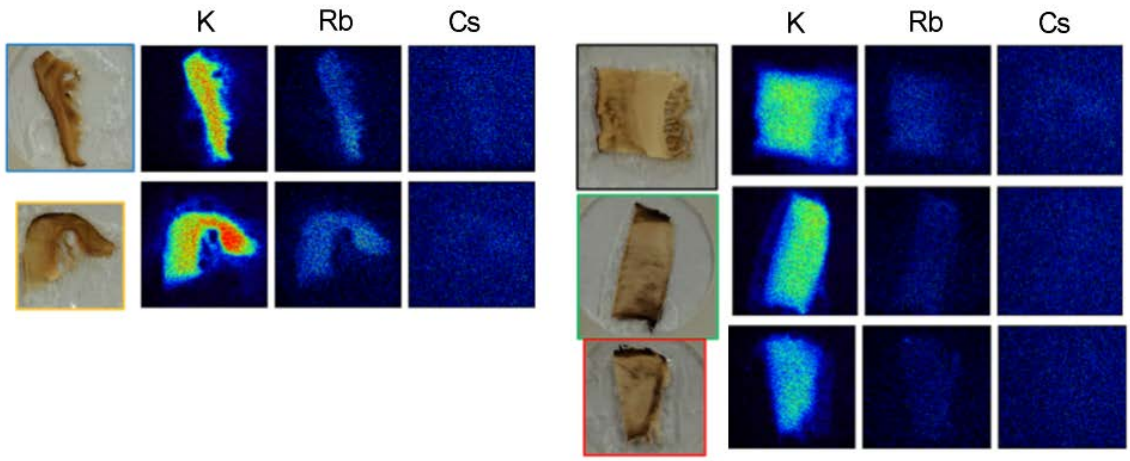

Figure 3. Spatial distributions of potassium, rubidium and cesium in the shiitake samples measured by submilli-PIXE analysis.

VI. RADIOCHEMISRTY AND NUCLEAR CHEMISTRY

VI. 1. Study on Solvent Extraction Behavior of Zirconium and Hafnium as Homologs of Rutherfordium (Element 104) with Chelate Extractant

Ooe K.[1], Tanaka A.[1], Kikunaga H.[2], Goto S.[1], and Kudo H.[3]

[1]Graduate School of Science and Technology, Niigata University
[2]Research Center for Electron Photon Science, Tohoku University
[3]Faculty of Science, Niigata University

Introduction

The elements with atomic numbers $Z \geq 104$ are called superheavy elements (SHEs). The SHEs can be produced only in the heavy-ion induced nuclear reactions. Because of short half-lives and low production rates of SHEs, chemical investigation of SHEs must be performed on atom-at-a-time scale. For these experimental restrictions, the chemical properties of SHEs are poorly known. In the region of SHEs, it is predicted that relativistic effects on orbital electrons may induce deviations from the periodicity of the chemical properties based on extrapolations from lighter homologs in the Periodic Table[1,2]. Therefore, the chemical studies of SHEs are extremely fascinating and challenging subjects.

We are planning to investigate the aqueous chemical behavior of element 104, rutherfordium (Rf). So far, aqueous chemical studies on Rf have been carried out mainly with inorganic ligands such as halide ions[3,4]. However, little has been reported on chemical experiments of Rf with organic ligands. In this study, as model experiments of Rf, we carried out the solvent extraction of zirconium (Zr) and hafnium (Hf), which are lighter homologs of Rf, using 2-thenoyltrifluoroacetone (TTA) as a chelate extractant.

Experimental

Radiotracers

Radiotracers of ^{88}Zr ($T_{1/2}$ = 83.4 d) and ^{175}Hf ($T_{1/2}$ = 70 d) were separately produced in the ^{89}Y (p, 2n) and ^{175}Lu (p, n) reactions, respectively, using the AVF cyclotron at Tohoku University. A pellet of Y_2O_3 (190 mg/cm^2) and a Lu metal foil (125 μm thickness) were used as targets. The incident energy of the proton beam was 16 MeV. The produced

radiotracers were chemically separated from the target materials through anion exchange separations and were stored in 1 M HNO_3 solution.

Solvent extraction procedure

Aqueous solution of 1 M HNO_3 (600 μL) containing ^{88}Zr and ^{175}Hf tracers was mixed with an equal volume of TTA in toluene solution in a polypropylene tube, and the mixture was mechanically shaken at 25 ºC. After equilibration, the mixture was centrifuged for 30 seconds, and 420 μL aliquots of each phase were transferred to separate polypropylene tubes. The radioactivity of each phase was measured by a Ge detector, and the distribution ratio (*D*) was calculated as the ratio of radioactivity of organic phase to that of aqueous phase.

Results and Discussion

Figure 1 shows the dependences of *D* values of ^{88}Zr and ^{175}Hf in 1 M HNO_3 solution as a function of shaking time with TTA in toluene solution (0.01 M TTA for Zr and 0.025 M TTA for Hf). It seems that the *D* values of ^{88}Zr and ^{175}Hf become constant in shaking time of 5 hours. Therefore, we selected shaking time of 5 hours in the following experiments.

Figure 2 shows the log *D* vs. log [TTA] plot in 1 M HNO_3-TTA in toluene system. It is well-known that the chemical behavior of Zr is remarkably similar to that of Hf. However, the results showed that the *D* value of ^{88}Zr was approximately 10 times greater than that of ^{175}Hf. Therefore, it is very interesting to compare extraction behavior of Rf in this extraction system with that for Zr and Hf. A weighted least-squares fit to the data showed straight line with slopes of 3.3 for both Zr and Hf. The slope of this plot indicates the number of TTA molecules involved in the extraction reaction. Therefore, this result suggests that the main extracted TTA complexes of Zr and Hf possibly contains three TTA molecules and one OH^- or NO_3^- ion as ligand in this experimental condition. This would be confirmed through extraction experiments in 1 M $HClO_4$ solution because the formation of perchlorate complexes of metal ions may be neglected.

For solvent extraction experiments of Rf, rapid chemical operations are required because of its short half-life of around 1 min. For this purpose, we are developing rapid solvent extraction apparatus using flow injection analysis (FIA) technique[5)]. In the near future, extraction experiments of Zr and Hf with the FIA system will be performed for Rf experiment.

Acknowledgments

We would like to thank the operating staff of AVF cyclotron at Tohoku University for providing the stable proton beam.

References

1) Schädel M, *Angew Chem. Int. Ed.* **45** (2006) 368.
2) Schädel M, *Radiochim. Acta* **100** (2012) 579.
3) Haba H, et al., *J. Nucl. Radiochem. Sci.* **3** (2002) 143.
4) Haba H, et al., *J. Am. Chem. Soc.* **126** (2004) 5219.
5) Koyama T, et al., *5th Asia-Pacific Symp. Radiochem.13 (APSORC 13)*, 25-NCP-05.

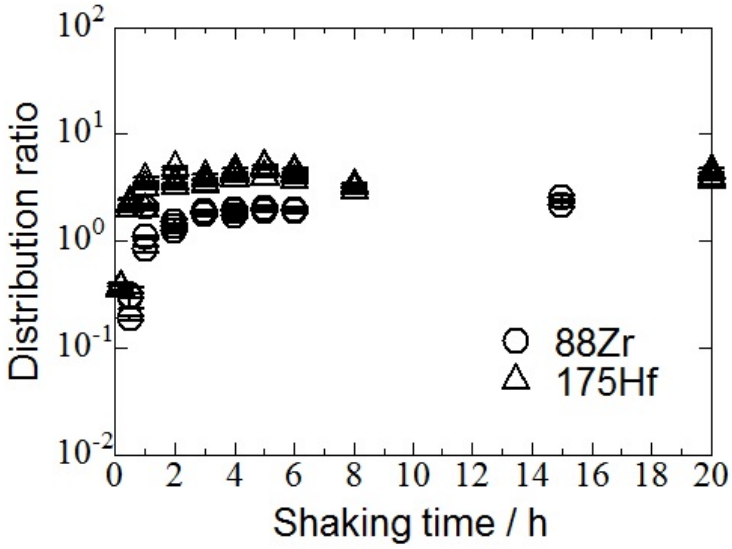

Figure 1. The dependence of distribution ratios of ^{88}Zr and ^{175}Hf as a function of shaking time. Aqueous phase is 1 M HNO_3 solution, and organic phase is TTA in toluene solution (0.01 M TTA for Zr and 0.025 M TTA for Hf).

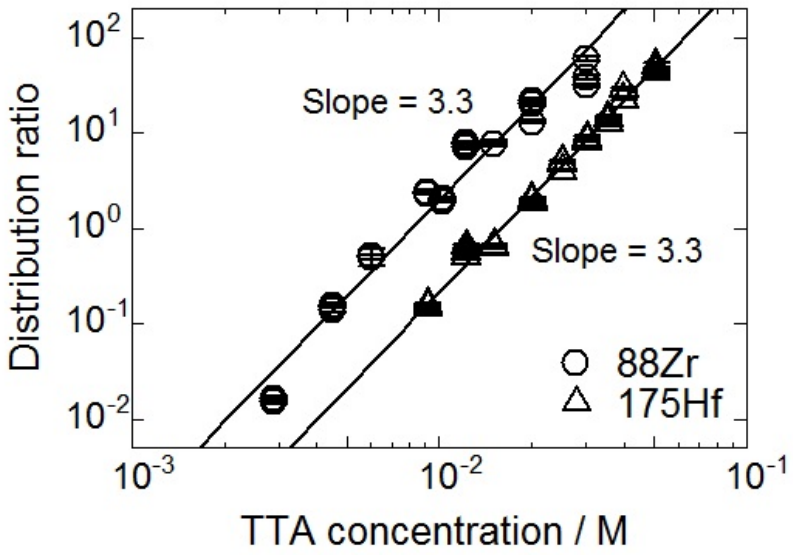

Figure 2. The log *D* vs. log [TTA] plot in 1 M HNO_3-TTA in toluene system.

VI. 2. Attempt for Preparation of an Thin Source for Low-Energy Particle Spectrometry

Kikunaga H.[1], Haba H.[2], and Kanaya J.[2]

[1]Research Center for Electron Photon Science, Tohoku University
[2]RIKEN Nishina Center

Introduction

Generally, internal conversion electrons originate from the K shell. If the decay energy of a nuclear isomer is less than the binding energy of an inner-shell electron, the emission of an electron from the shell is forbidden, in which case the isomer interacts with outer-shell electrons. As a result, the probability of internal conversion is affected by the outer-shell electron state, namely the chemical state. Examples of this type of nuclides are ^{99m}Tc (2.17 keV) and ^{229m}Th (7.6 eV). The goal of our research is to measure such low energy internal conversion electrons of various chemical states. For high-resolution energy spectrometry, it is necessary to prepare radionuclides as a thin source. In this report, we attempt to prepare an ultra-thin source using the Self-Assembled Molecular (SAM) technique. The performance of the SAM substrate was investigated through radio-tracer experiments.

Experimental

Single isotope tracers and RIKEN Ag-based multi-isotope tracers were used for the experiments. Single-isotope tracers of ^{88}Y and ^{88}Zr were produced from $SrCl_2$ and Y metal targets, respectively, using the AVF cyclotron at CYRIC, Tohoku University. The $SrCl_2$ target was dissolved in 0.1 M HNO_3 and the solution passed through an Eichrom Ln resin column, which adsorbs Y isotopes. The resin was washed with 0.1 M HNO_3 to remove target materials. Then Y isotopes were eluted from the column with 6 M HNO_3. The Y metal target was dissolved in 12 M HCl and the solution passed through an anion exchange column to separate Zr isotopes from target materials. The Zr isotopes were eluted from the column with 4 M HCl. The multi-tracers were produced by irradiation of a Ag metal plate

with a ^{14}N ion beam accelerated by the RIKEN Ring Cyclotron. Ag target material was removed by a precipitation method with the use of hydrochloric acid.

The procedure for the preparation of SAM substrates was similar to that described in Ref. 1. An Al plate 25 mm in diameter was polished and rinsed with distilled water. After drying, the Al plate was treated with 1 vol.% 3-aminopropyltriethoxysilane (APTES) in absolute toluene through chemical vapor deposition in a self-made PTFE cell at 100 ^{o}C for 2 h; subsequently, it was rinsed with methanol and absolute toluene. Phosphonation of the terminal amino groups of APTES was performed with phosphoryl chloride and γ-collidine in absolute acetonitrile, and the sample was then rinsed with absolute acetonitrile and distilled water. The coupling of the SAM substrate and radionuclides was carried out in an aqueous solution or an isopropyl alcohol solution.

Results

The bound radionuclides were assayed by γ-ray spectrometry with an HPGe semiconductor detector. A γ-ray spectrum of a multitracer-SAM sample is shown in Fig. 1. The γ-peaks of ^{46}Sc, ^{54}Mn, ^{65}Zn, ^{75}Se, ^{83}Rb, ^{85}Sr, ^{88}Zr, ^{88}Y, ^{101}Rh, and ^{102m}Rh are observed in the spectrum. By comparison of γ-peak counts of each nuclide, we found that the yield of nuclides with oxidation states +3 and +4 is relatively high. On the other hand, ^{22}Na and ^{57}Co were not detected, although these nuclides were included in the multi-tracer solution. This tendency was found regardless of the reaction solvent to be combined with radionuclides.

To confirm the uniformity of the SAM source, the α source was prepared with ^{241}Am tracer and subjected to autoradiography. A photograph taken using an imaging plate is shown in Fig. 2. The deviation of α activity is observed at the upper-left part of the image. This deviation probably originates from fine scratches on the Al plate. With the exception of this part, the α activity is spread uniformly over the entire SAM substrate. Although there are still some problems, the present method will provide us with a reliable ultrathin source after some improvements.

Reference

1) A. Shida et al., *Surf. Coat. Technol*. **169-170** (2003) 686.

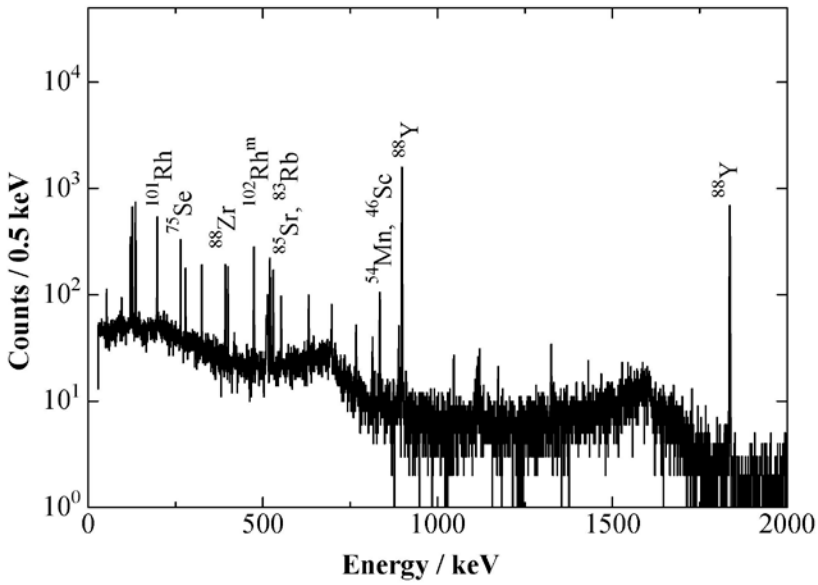

Figure 1. An example of a γ-ray spectrum of a multitracer SAM sample.

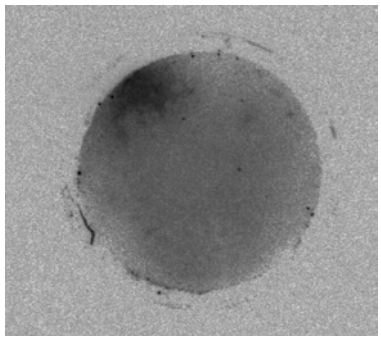

Figure 2. Photographic image of a ^{241}Am-SAM sample taken using an imaging plate.

VI. 3. Study on Separation of Platinum Group Metals from High Level Radioactive Waste Using Solid State Adsorbent

Ito T.[1], Kim S.-Y.[1], Xu Y.[1], Hitomi K.[1], Ishii K.[1], Nagaishi R.[2], and Kimura T.[2]

[1]Department of Quantum Science and Energy Engineering, Tohoku University
[2]Japan Atomic Energy Agency

Introduction

Platinum group metals (PGMs), namely Ru, Rh and Pd, are contained in high level liquid waste (HLLW) released from PUREX reprocessing of spent nuclear fuel (~ 5.6 kg/1tHU, PWR, UO_2 fuel, 45 GWd/t, 5 years cooling)[1)], and separation and recovery of the PGMs has been studied to achieve effective utilization of the valuable elements[2,3)]. The reuse of the recovered PGMs could be considered to be a reasonable way to secure the resources of PGMs as semi-domestic resources because most nuclides of PGMs in HLLW are stable and the other nuclides are short-lived or weak radioactive isotopes. On the other hand, Ru, Rh and Pd are known to obstruct producing of vitrified HLLW[4)]. Therefore, the selective separation of PGMs from HLLW was considered to improve the process of vitrification.

Several methods such as precipitation[5)], active carbon adsorption[6)] and solvent extraction[2,7,8)] have been reported for separation of PGMs from HLLW. In contrast with above all, separation of PGMs using solid state adsorbent has many attractive advantages, such as minimum use of organic diluents, compact equipment, easy phase separation and less waste accumulation. Ion exchange resin is one of the most easily available solid state adsorbent because the resin could be purchased from many suppliers. On the other hand, macroporous silica-based adsorbent used in extraction chromatography technique is one of the most efficient solid state adsorbents because the adsorbent was made by immobilizing the highly selective extractant into the macroporous silica/polymer composite support (SiO_2-P) which has advantages such as strong acid and radiation resistance when compared with organic polymer beads[9)].

In this study, we examined three kinds of adsorbent, primary amine type anion

exchange resin, quaternary ammonium type anion exchange resin and macroporous silica-based adsorbent of (MOTDGA-TOA)/SiO_2-P, to separate PGMs from HLLW. The anion exchange resins were expected to separate PGMs of anionic complex form and the extractants of MOTDGA and TOA impregnated into the SiO_2-P were determined from the literature of solvent extraction with expectation of excellent separation of Pd(II)[7,8].

Experimental

Materials

The anion exchange resin, LEWATIT® VPOC1065 with primary amine and LEWATIT® MonoPlus MP800 with quaternary ammonium, were purchased from LANXESS K.K. The extractant, *N*,*N*'-dimethyl-*N*,*N*'-di-*n*-octyl-thiodiglycolamide (MOTDGA, $[C_8H_{17}N(CH_3)C(O)CH_2]_2S$, Fig. 1) was synthesized from thiodiglycolic acid purchased from Wako Pure Chemical Industries, Ltd[7]. Other materials for synthesis such as thionyl chloride, trietylamine, *N*,*N*-dimethylformamide were obtained from Kanto Chemical Co, and *N*-methyloctylamine from ACROS ORGANICS. Tri-*n*-octylamine (TOA, $(C_8H_{17})_3N$) was procured from Wako Pure Chemical Industries, Ltd. and used without any further purification. Macroporous silica-based (MOTDGA-TOA)/SiO_2-P adsorbent was also prepared by impregnation of MOTDGA and TOA into the pore of the SiO_2-P support[9].

Ruthenium nitrosyl nitrate solution (1.5 wt%), rhodium nitrate solution (10 wt%) and palladium nitrate solution (4.5 wt%) were purchased from Sigma-Aldrich Chemical Co. Other chemicals such as $RE(NO_3)_3 \cdot 6H_2O$ (RE = La, Ce, Nd, Sm and Gd), $ZrO(NO_3)_2 \cdot 2H_2O$, $(NH_4)_6Mo_7O_{24} \cdot 4H_2O$ and Re_2O_7 were supplied by Kanto Chemical Co. The simulated HLLW was made by adding the metal reagents to HNO_3 solution and distilled water to the desired concentration.

Batch adsorption experiment

The effect of contact time and HNO_3 concentration on adsorption of Ru(III), Rh(III) and Pd(II) were examined by batch method with a thermostatic shaking bath. The liquid phase which was separated from solid phase by 0.20 μm filter was analyzed by Inductively Coupled Plasma Atomic Emission Spectrometry to determine the concentration of metal ions. Uptake percentage and distribution coefficient K_d were calculated as follows:

$$\text{Uptake} = (C_0 - C_t) / C_0 \times 100\ (\%) \quad (1)$$

$$K_d = (C_0 - C_e) / C_e \times V/m\ (\text{cm}^3/\text{g}) \quad (2)$$

where C_0, C_t and C_e are the concentration (mmol/dm^3) of metal ions in the solution at

beginning, at time of *t*, and at equilibrium, respectively. *V* (cm^3) is the volume of liquid phase and *m* (g) is the weight of the solid state adsorbent.

Column separation experiment

The chromatographic separation behavior of metal ions was demonstrated by the (MOTDGA-TOA)/SiO_2-P packed glass column with thermostatic water jacket at 25 ºC. The simulated HLLW was passed through the column at the flow rate of 0.3 cm^3/min, and then the given volumes of washing and elution solutions were subsequently pumped through the column, respectively.

Results and Discussion

Effect of Contact Time on Adsorption of PGMs

Figures 2 and 3 illustrate uptake rate of Ru(III) and Pd(II) onto the primary amine type anion exchanger and the quaternary ammonium type anion exchanger in 3.0 mol/dm^3 HNO_3 solution at 25 ºC, respectively. Low adsorption affinity of Rh(III) for the both anion exchanger were obtained. The primary amine type adsorbed Pd(II) at slow rate from 2 hr after. The other adsorption achieved equilibrium within 2 hr. All observed uptake percentage was smaller than 50 %. On the other hand, the uptake of Pd(II) onto the (MOTDGA-TOA)/SiO_2-P adsorbent was fairly fast, and about 80 % of Pd(II) was taken up within 1 hr (Fig. 4). The adsorption of Ru(III) and Rh(III) also showed higher affinity for the adsorbent than the both anion exchanger although the uptake rate of Ru(III) and Rh(III) were slow.

From the results, it was thought that the (MOTDGA-TOA)/SiO_2-P was suitable adsorbent for partitioning operation of HLLW using column method.

Effect of HNO_3 Concentration on Adsorption of PGMs

Figure 5 indicates adsorption capability of the (MOTDGA-TOA)/SiO_2-P for Ru(III), Rh(III), Pd(II), Zr(IV), Mo(VI) and RE(III) in the HNO_3 concentration range of 0.10-5.0 mol/dm^3 at 25ºC. RE(III) ions showed almost no adsorption affinity for the adsorbent under the condition. This implied that RE(III) and minor actinide (MA(III)) contained in HLLW had noaffinity for the adsorbent due to the similar chemical properties. In contrast, relatively large K_d of Pd(II) was obtained. The K_d value decreased with increasing HNO_3 concentration up to 1.0 mol/dm^3. The decrease was also observed for the primary amine type up to 5.0 mol/dm^3 of HNO_3 concentration. N atom contained in N donor extractant

such as TOA and weak-base anion-exchanger acted as a Lewis base and a soft-donor which has affinity for soft metal ion such as Pd(II). Therefore, it was thought that the adsorption of Pd(II) with large K_d value were caused by its direct bonding to the N atom possessing lone-pair electrons, and then competing adsorption of H^+ with Pd(II) resulted in the decrease of K_d with increasing concentration of HNO_3. In the (MOTDGA-TOA)/SiO_2-P using MOTDGA and TOA simultaneously, not only Pd(II) but also Ru(III) and Rh(III) showed adsorption affinity for the adsorbent because S donor extractant such as MOTDGA was softer than N donor and synergetic effect occurred by the two kinds of extractants[10]. Experimental results indicated that the (MOTDGA-TOA)/SiO_2-P have a potential to separate PGMs from RE(III) in HNO_3 solution which was same medium of HLLW.

Chromatographic separation

Figure 6 displays the chromatogram of Ru(III), Rh(III), Pd(II), Zr(IV), Mo(VI), La(III), Ce(III), Nd(III), Sm(III), Gd(III) and Re(VII), which was alternate element of Tc, using (MOTDGA-TOA)/SiO_2-P packed column. Pd(II) which showed large K_d and fast uptake rate for the adsorbent was isolated from the other metal ions by using a complexing agent, 0.20 mol/dm^3 thiourea - 0.10 mol/dm^3 HNO_3 solution as eluent. Mo(IV) and Re(VII) weekly adsorbed and they were washed out with 3.0 mol/dm^3 HNO_3 solution. This indicated no influence of Re(VII) in the separation of Pd(II). On the other hand, Ru(III) and Rh(III) were quickly leaked from the column because they showed slow uptake rate onto the adsorbent.

From the result, the (MOTDGA-TOA)/SiO_2-P was considered to be a promising adsorbent for separation of Pd(II) from HLLW. Ru(III) and Rh(III) were thought to be separated from RE(III) by using TODGA/SiO_2-P which had no adsorption ability for Ru(III) and Rh(III)[11].

Conclusion

To separate PGMs from HLLW, primary amine type anion exchange resin, quaternary ammonium type anion exchange resin and macroporous silica-based adsorbent of (MOTDGA-TOA)/SiO_2-P were prepared and then the adsorption and separation behavior of the solid state adsorbents were examined by batch and column experiment, respectively.

Both of the anion exchangers showed smaller uptake percentage of Ru(III) and Pd(II) than 50% and few adsorption affinity for Rh(III). On the other hand, the (MOTDGA-TOA)/SiO_2-P showed higher adsorption capability and faster uptake rate for

Pd(II) than the both of anion exchangers. In addition, a possibility of separation of Ru(III) and Rh(III) in HNO_3 solution was observed.

Excellent isolation behavior of Pd(II) from Ru(III), Rh(III), Zr(IV), Mo(VI), La(III), Ce(III), Nd(III), Sm(III), Gd(III) and Re(VII) in 3.0 mol/dm^3 HNO_3 solution was obtained in chromatographic separation using the (MOTDGA-TOA)/SiO_2-P packed column.

The result suggested that the (MOTDGA-TOA)/SiO_2-P can be proposed as a promising adsorbent for separation of Pd(II) from HLLW.

References

1) Ando Y., Takano H., *JAERI-Research* 99-004 (1999).
2) Kondo Y., Kubota M., Abe T., Nagato K., *JAERI-M* 91-147 (1991).
3) Bush P R., *Platinum Metals Rev.* **35** (1991) 202.
4) Krause Ch., Luchscheiter B. J., *Mater. Res.* **6** (1991) 2535.
5) Kondo Y., Kubota M., *J. Nucl. Sci. Technol.* **29** (1992) 140.
6) Kononova N O., et al., *J. Porous. Mater.* **15** (2008) 61.
7) Narita H., et al., *Miner Eng.* **21** (2008) 483.
8) Ruhela R., et al., *Sep. Sci. Technol.* **46** (2011) 965.
9) Wei Y-Z., et al., *Nucl. Technol.* **132** (2000) 413.
10) Sasaki. Y. and Tsuge. S., *Complex Chemistry*, Shoukabo, (2009).
11) Hoshi. H., et al., *J. Alloys Comp.* **374** (2004) 451.

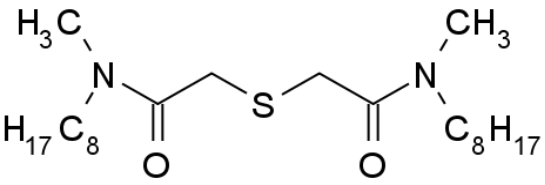

Figure 1. Molecular structure of MOTDGA.

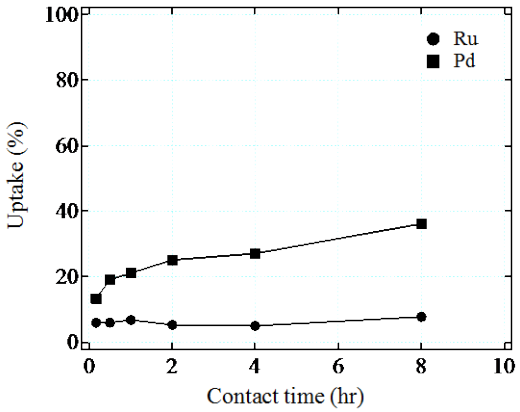

Figure 2. Effect of contact time on uptake of PGMs by primary amine type anion exchanger.
V/*m*: 50 cm^3/g; [HNO_3]: 3.0 mol/dm^3; [Metal]: 1 mmol/dm^3; Temperature: 25 ^{o}C.

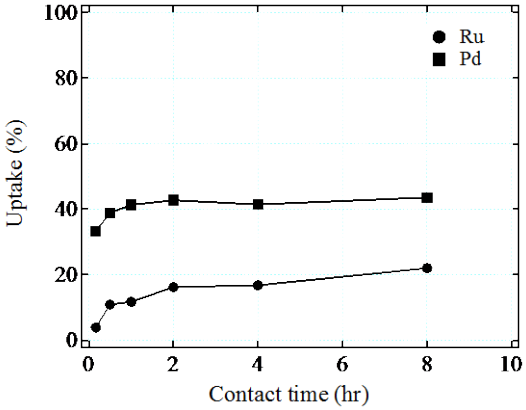

Figure 3. Effect of contact time on uptake of PGMs by quaternary ammonium type anion exchanger. *V*/*m*: 50 cm^3/g; [HNO_3]: 3.0 mol/dm^3; [Metal]: 1 mmol/dm^3; Temperature: 25 ºC.

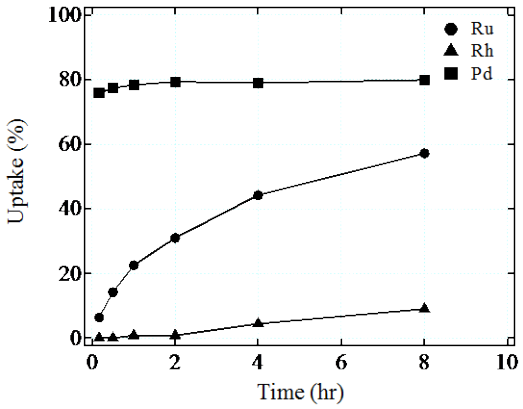

Figure 4. Effect of contact time on uptake of PGMs ions by (MOTDGA-TOA)/SiO_2-P. *V*/*m*: 20 cm^3/g; [HNO_3]: 3.0 mol/dm^3; [Metal]: 5 mmol/dm^3; Temperature: 25 ºC; Contact time: 8 hr.

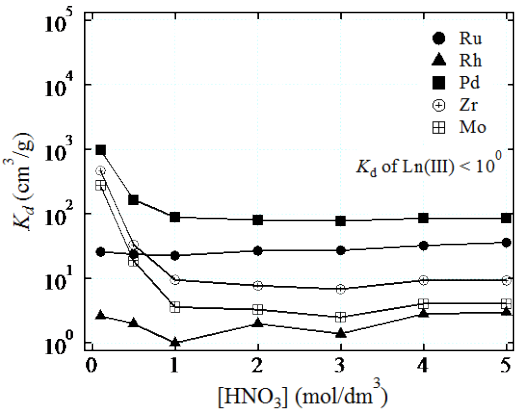

Figure 5. Effect of HNO_3 concentration on uptake of PGMs by (MOTDGA-TOA)/SiO_2-P. *V*/*m*: 20 cm^3/g; [Metal]: 5 mmol/dm^3; Temperature: 25 ºC; Contact time: 8 hr.

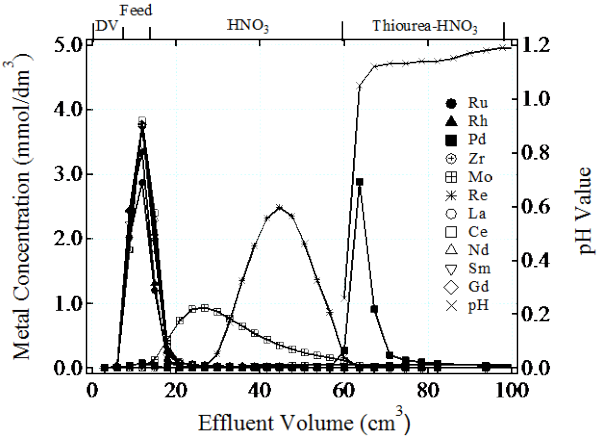

Figure 6. Chromatographic separation of simulated HLLW using (MOTDGA-TOA)/SiO_2-P column. Column: 8 mm × 120 mm; Adsorbent: 4 g; flow rate: 0.3 cm^3/min; Temperature: 25 ºC.

VI. 4. Electrochemical Properties of Austenitic Stainless Steel (R-SUS304ULC) in Nitric Acid Solution

Hasegawa S.[1,3], Kim S. -Y.[1], Ebina T.[1,3], Tokuda H.[2,3], Hitomi K.[1], and Ishii K.[1]

[1]*Department of Quantum Science and Energy Engineering, Tohoku University*
[2]*Cyclotron and Radioisotope Center, Tohoku University*
[3]*Japan Nuclear Fuel Limited*

Introduction

Nuclear fuel reprocessing of PUREX (Plutonium and Uranium Recovery by Extraction) process uses nitric acid as the dissolution reaction medium. In this process, severe corrosive environment to the equipment material is caused by heating operation of the nitric acid solution. An austenitic stainless steel is one of important materials used in the reprocessing plant. R-SUS304ULC is the ultra-low-carbon austenitic stainless steel for the reprocessing plant developed in Japan (R: Reprocessing, ULC: Ultra Low Carbon) based on the corrosion problem in Tokai reprocessing plant[1-3]. This stainless steel has high corrosion resistance because the carbon content is specified to be less than 0.020 wt% in order to avoid sensitization associated with chromium depletion along grain boundaries during the welding process, and it has been used in Rokkasho reprocessing plant[4].

On the other hand, the corrosion of stainless steel in nitric acid solution is affected by the redox potential increases with concentrations in NO_3^- and H^+, temperature increases and decreases with HNO_2 concentration[5]. Also, the gaseous species of NO and NO_2 affects the redox potential in nitric acid solution[6]. In addition, ions having high oxidizability such as Ru, Pu, Np and Cr accelerate the corrosion of stainless steel, and these show the complex redox behavior in nitric acid solution[7-12]. In the reprocessing plant, the nitric acid solution handled wide range nitric acid concentration and temperature. Therefore, to understand these changes in solution environment gives the useful information for grasping of the redox reaction of oxidation ions and corrosion behavior of the stainless steel.

In this study, we investigated relationship between the corrosion behavior of R-SUS304ULC steel and the environment change of nitric acid solution by temperature

increases using electrochemical measurements and thermodynamic calculations.

Experimental

Materials

Solutions used for electrochemical tests were 3 M (M=mol·L^{-1}) and 8 M nitric acid. The concentration of 3 M nitric acid is equivalent of the nuclear spent fuel solution, and 8 M nitric acid is equivalent to use of the environment of HLLW (High Level Liquid Waste) evaporator and acid recovery evaporator in Rokkasho Reprocessing Plant[4]. The nitric acid concentration of the test solution was determined by potentiometric titration with 0.1 M NaOH solution. The test solution (100 mL) was introduced into a 300-mL Pyrex flask. Table 1 shows the chemical composition of R-SUS304ULC of the test specimen. The specimen is flag type (measurement part: $20\times15\times2^{t}$ mm, cross-section of lead part: 1×1 mm). This surface was wet polished with emery papers down to #800, and rinsed with pure water and acetone under sonication. The ratio of the test solution volume and surface area of the specimen were about 40 mL·cm^{-2}.

Electrochemical tests

Figure 1 shows the apparatus for electrochemical tests. The potentiostat was an ALS/CH Instruments Model 611DT electrochemical analyzer. A three electrode system was utilized, *i.e.*, R-SUS304ULC working electrode (surface area: 2.5 cm^{-2}), a Hokuto Denko Corp. HX-C7 Pt counter electrode, and a BAS RE-1C reference electrode (SSE: Ag/AgCl, sat. KCl). The lead part of working electrode was coated with Teflon tube. The reference electrode connected by a salt bridge having a porous ceramic. The polarization measurement was performed after the rest potential was stable (about 1 hour after reaching the measurement temperature), and measured in order of cathode and anode in each temperature from the room temperature to the boiling point. The scan rate was performed by 0.01 V·s^{-1}.

Thermodynamic calculations using the SOLGASMIX program

The thermodynamic calculation was performed by SOLGASMIX program. SOLGASMIX calculation code and thermodynamic constants were obtained from the HSC Chemistry version 7.1 software (Outokumpu Research, Finland). The calculation method was performed using the model calculation of boiling nitric acid devised by Kato *et al*[5].

Results and discussion

Electrochemical tests

Figure 2 shows the results of polarization measurement. Corrosion potentials were shifted to the noble direction with temperature increases in either case. Also, we see from Figure 2 that the corrosion reaction of R-SUS304ULC is dominated by cathode reaction because the current density of cathode side was increased with temperature increases. Now, the equation of redox reaction of nitric acid is expressed as follows[13]:

$$NO_3^- + 3H^+ + 2e^- = HNO_2 + H_2O \ (E^0 = 0.934\ \text{V}\ \textit{vs.}\ \text{SHE}) \quad (1)$$

$$HNO_3 + 2H^+ + 2e^- = HNO_2 + H_2O \ (E^0 = 0.934\ \text{V}\ \textit{vs.}\ \text{SHE}) \quad (2)$$

Nernst equation corresponding to equations (1) and (2) are as follows[13]:

$$E = E^0 - \frac{2.303 \times 3 \times RT}{2F}\text{pH} + \frac{RT}{2F}\ln\frac{[NO_3^-]}{[HNO_2]} \quad (3)$$

$$E = E^0 - \frac{2.303 \times 2 \times RT}{2F}\text{pH} + \frac{RT}{2F}\ln\frac{[HNO_3]}{[HNO_2]} \quad (4)$$

where R is the gas constant (=8.3145 J mol^{-1} K^{-1}), T is the temperature (K), F is the faraday constant (=9.6485×10^4 C mol^{-1}). We see from the equation (1) and (2) that the reduction reaction of nitric acid on the corrosion of stainless steel is reduction reaction of NO_3^- and HNO_3, and the redox potential of nitric acid is dominated by concentration of NO_3^-, HNO_3, and HNO_2 from the equation (3) and (4). Also, we consider that the reduction reaction on the surface of stainless steel is likely to proceed with increasing temperature in either case 3 M and 8 M nitric acid solution, because the cathode current density is increased with temperature increases. However, in the case of 8 M nitric acid, increases of current density with temperature increases were smaller than 3 M nitric acid. We consider that the factor is related to the composition change of nitric acid solution such as dissociated nitric acid, undissociated nitric acid, and nitrous acid. Figure 3 shows the change of degree of nitric acid dissociation (α), stoichiometric activity coefficient of nitric acid (y_s) (a product of a mean ionic activity coefficient, $y_\pm$, and a degree of dissociation, α, $y_s = y_\pm\alpha$), and activity coefficient of undissociated nitric acid (y_u) with nitric acid concentration change[14]. The degree of dissociation is about 0.9 in the case of 3 M nitric acid. On the other hand, it decreases with increasing nitric acid concentration, and it is about 0.6 in the case of 8 M nitric acid. In addition, stoichiometric activity coefficient of nitric acid (y_s) and activity coefficient of undissociated nitric acid (y_u) are changed remarkably with more than 3 M nitric acid. Therefore, there is a possibility that the cathode reaction rate is changed by the shift of the equilibrium due to the composition change of the nitric acid solution.

Thermodynamic calculation using the SOLGASMIX program

In order to investigate the composition change of the nitric acid solution, we evaluated the equilibrium state of nitric acid solution at each conditions of 3 M and 8 M nitric acid using the SOLGASMIX calculation code. Table 2 shows the initial values used in the calculation. Nitrogen oxides for the calculation were used NO_3^-, HNO_3, HNO_2, NO_2, and NO. These species are significant nitrogen oxides involved in the determination of the redox potential of nitric acid solution[5]. The initial concentration of nitrous acid was 1 mM which is close to the measured redox potential[5]. Figure 4 shows the calculation results of each condition. While the boiling point was deviated from the calculation results of the temperature at gas generation, it is considered that the calculation code does not accurately calculate the vapor-liquid equilibrium. Kato *et al*. also reported that a similar deviation occurs[5]. In the case of 8 M nitric acid, the ratio of the undissociated nitric acid for the dissociated nitric acid is larger than the 3 M nitric acid. For example, in the case of 3 M nitric acid, the ratio of NO_3^-/ HNO_2 changed to 1.8×10^3 from 2.5×10^3 (0.72 times) when the temperature increased to 373 K from 300 K, and the ratio of HNO_3/ HNO_2 changed to 1.3×10^3 from 4.9×10^2 (2.65 times). On the other hand, in the case of 8 M nitric acid, the ratio of NO_3^-/ HNO_2 changed to 3.8×10^3 from 6.0×10^3 (0.63 times) when the temperature increased to 373 K from 300 K, and the ratio of HNO_3/ HNO_2 changed to 4.3×10^3 from 2.0×10^3 (2.15 times). We see from these calculation results that the decrease in NO_3^-/ HNO_2 ratio and the increase in HNO_3/ HNO_2 ratio in the case of 8 M nitric acid are smaller than the 3 M nitric acid. Therefore, we consider that the redox potential of nitric acid solution is dominated by redox reaction of undissociated nitric acid with increasing of temperature and nitric acid concentration.

Conclusions

In polarization measurements, the corrosion potential of R-SUS304ULC was shifted to the noble direction with temperature increases, and it is dominated by the cathode reaction of nitric acid solution. In the thermodynamic calculation, the ratio of the undissociated nitric acid for the dissociated nitric acid in the case of 8 M nitric acid was larger than the 3 M nitric acid, and it is increased with temperature increases.

Therefore, the results suggested that the corrosion reaction of R-SUS304ULC is dominated by the concentration of undissociated nitric acid and nitrous acid with the increasing of temperature and nitric acid concentration.

References

1) Maki A., *JNC Technical review* **14** (2002) 39.
2) Hyakubu T., et al., *Proc. Int. Symp. on Plant Aging and Life Prediction of Corrodible Structures* Sapporo (Japan) (1995) 15.
3) Inazumi T., et al., *NKK Tech. Rev.*. **144** (1993) 20.
4) Wada F., *Zairyo-to-Kankyo* **48** (1999) 771.
5) Kato C., et al., *Zairyo-to-Kankyo* **52** (2003) 44.
6) Armstrong R D., et al., *J. Appl. Chem.* **28** (1998) 1205.
7) Okubo M., et al., P*roc. RECOD 87*. Paris (France) (1987) 1181.
8) McIntosh A B., et al., *Proc. 2nd Int. Conf. on peaceful users of atomic energy*. Geneva (Switzerland) (1958) 206.
9) Hirose Y., et al., *Proc. RECOD 87* Paris (France) (1987) 501.
10) Arai Y., et al., *Zairyo-to-Kankyo* **48** (1999) 235.
11) Takeuchi M., et al., *Trans. At. Energy Soc. Jpn.* **5** (2005) 32.
12) Motooka T., et al., *J. Nucl. Sci. Technol. Suppl.* **3** (2002) 367.
13) Pourbaix M., *Atras of electrochemical equilibria in aqueous solutions* 2nd ed. NACE, Texas (1974) 493.
14) Davis W Jr., et al., *J. Inorg. Nucl. Chem.* **26** (1964) 1069.

Table 1. Chemical composition of R-SUS304ULC (mass %).

C	Si	Mn	P	S	Cr	Ni	Fe
0.019	0.39	0.88	0.028	0.002	18.1	9.11	Bal.

Table 2. Initial conditions for thermodynamic calculations.

Total volume	Pressure	H_2O	H^+	NO_3^-	HNO_3	HNO_2	NO_x
L	MPa	mol/L					
1	0.101	41 51	8 3	8 3	0	1×10^{-3}	0

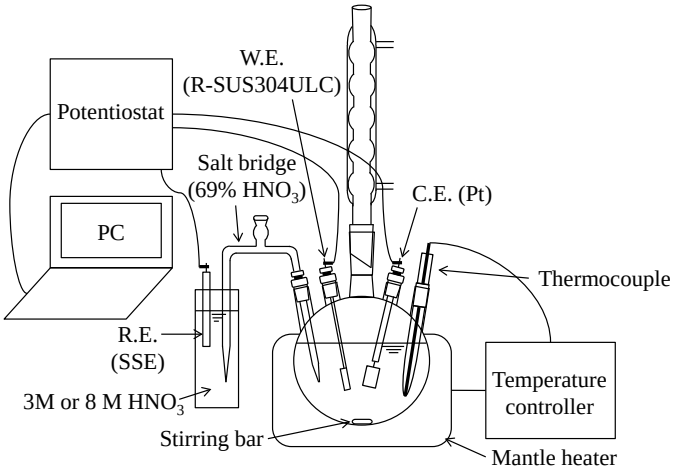

Figure 1. A schematic diagram of electrochemical tests.

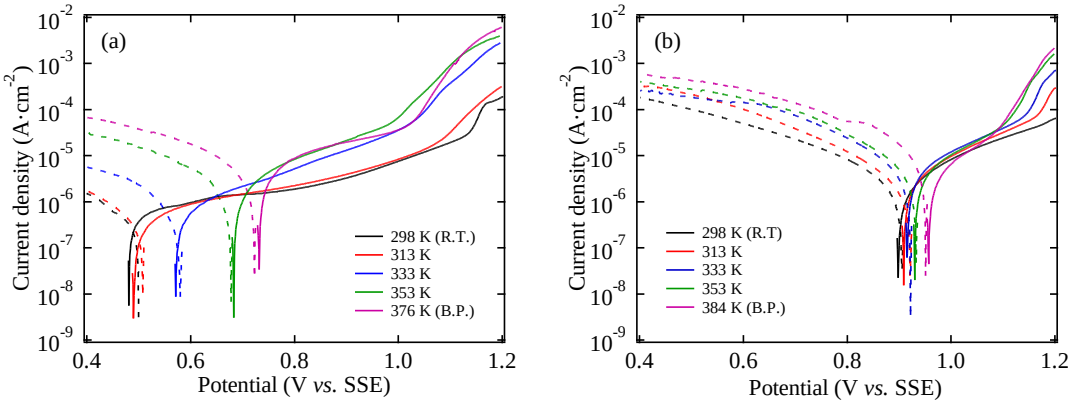

Figure 2. Polarization curves of R-SUS304ULC in nitric acid solution, broken line: cathodic, solid line: anodic, (a) 3 M HNO_3, (b) 8 M HNO_3.

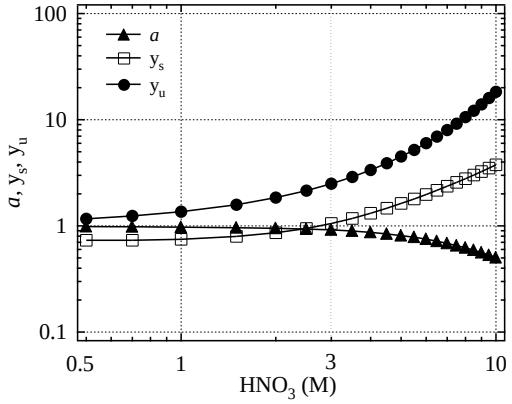

Figure 3. Degree of dissociation and activity coefficients in nitric acid solution at 298 K[14].

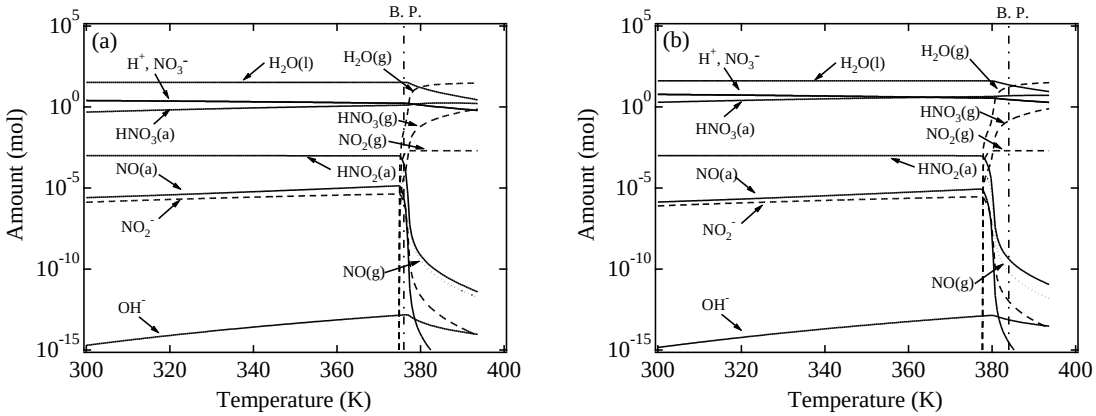

Figure 4. Relationship between temperature and amount of compounds in nitric acid solution calculated by SOLGASMIX program, state: g=gas, l=liquid, a=ion for aqueous species, (a) 3 M HNO_3, (b) 8 M HNO_3.

VI. 5. Extraction of Cesium and Strontium from Nitric Solutions Using 18-Crown-6 in Ionic Liquids

Takahashi T.[1,3], Kim S.-Y.[1], Tokuda H.[2,3], Hitomi K.[1], and Ishii K.[1]

[1]Department of Quantum Science and Energy Engineering, Tohoku University
[2]Cyclotron and Radioisotope Center, Tohoku University
[3]Japan Nuclear Fuel Limited

Introduction

Recently, much attention has been given to the selective separation and recovery of ^{137}Cs and ^{90}Sr from high level liquid waste (HLLW) in relation to the partitioning of radioactive nuclides and their effective utilization. The heat-generated nuclides are hazardous fission products (FP) and an increasing attention is paid to their efficient removal from HLLW[1)]. ^{137}Cs and ^{90}Sr, having relatively long half-life of about 30 years, exhibit high radioactivity and heat generation, and large amounts of Cs group (3.6 kg/1tHU, 45 GWd/t) and Sr group (1.1 kg/1tHU, 45 GWd/t) are contained in HLLW. These resulted in the lowering of mechanic strength of the glass product and its long term storage. Therefore, selective separation of ^{137}Cs and ^{90}Sr in HLLW is an important environmental issue for nuclear waste management. In addition, the purified ^{137}Cs and ^{90}Sr are also expected for the reuse as radiation and geat sources in the field of medicine and industry. Many methods for the separation of ^{137}Cs and ^{90}Sr such as ceramic solidification method has been studied[2-4)] .

While many investigations have been carried out on the extraction of Cs(I) and Sr(II) by ionic liquids, it is still worthwhile to perform systematic analysis of the extraction behaviors under various conditions, especially those related with the specialty of HLLW. Chen[5)] reported the extraction of Cs(I) and Sr(II) from aqueous solutions using the ionophores calix[4]arene-bis(tert-octylbenzo-crown-6) and dicyclohexano-18-crown-6, respectively, ionic liquid, $Bu_3MeNNTf_2$. The extraction of Sr(II) by adopting 1-ethyl-3-methyl-imidazolium bis(trifluoromethyl-sulfonyl)imide as solvent and dicyclohexane-18-crown-6 as extractant by Dai et al.[6)].

Based on this background, the present work deals with the extraction behavior of

Cs(I) and Sr(II) from aqueous solutions using the organic phase containing the crown ether as extractant in ionic liquids, [$C_n$mim][Tf_2N] (n = 2, 4, 6).

Experimental

Materials

All chemicals and reagents used for experiments and analyses were of analytical grade. Benzo-18-crown-6 (B18C6), Dibenzo-18-crown-6 (DB18C6), 1-ethyl-3-methyl-imidazolium bis[(trifluoromethyl)sulfonyl]imide ([C_2mim][Tf_2N]), 1-butyl-3-methyl-imidazolium bis[(trifluoromethyl)sulfonyl]imide ([C_4mim][Tf_2N]) and 1-hexyl-3-methyl-imidazolium bis[(trifluoromethyl)sulfonyl]imide ([C_6mim][Tf_2N]) were purchased from Merck KGaA and Sigma-Aldrich Chemical Co., respectively.

Methods

In batch extraction experiment, effects of HNO_3 concentrationon on the extraction of Cs(I) and Sr(II) using B18C6 and DB18C6 as extractant and three ionic liquids as solvent were examined, respectively. A 2 mL portion of ionic liquids(ILs)containing B18C6 and DB18C6 with different concentration was thoroughly mixed with a 2 mL aqueous solution of Cs(I) and Sr(II) in a voltex mixer for 15 min, followed by centrifuging to ensure fully phase separation. Then, a suitable volume of the aqueous phase was removed into 25 mL measuring flask and diluted with ultra-pure water. The concentrations of Cs(I) and Sr(II) in aqueous phase were determined by atomic absorption spectrophotometer (AAS, Shimadzu AA-6200). The concentration of H^+ ions in solution was measured by potentiometric titration (Metrohm TitrinoPlus848) with 0.1 M NaOH solution. The extraction efficiency (E) and distribution ratio (D) for extraction of Cs(I) and Sr(II) were calculated as follows

$$E = \frac{100 \times D}{D + \frac{V_{Aq}}{V_{IL}}} \quad , \quad D \equiv \frac{C_{IL}}{C_{Aq}} = \frac{C_{0Aq} \times \frac{V_{0Aq}}{V_{IL}} - C_{Aq} \times \frac{V_{Aq}}{V_{IL}}}{C_{Aq}}$$

where $C_{0\mathrm{Aq}}$ and C_{Aq} represent the initial and final concentrations of Cs(I) and Sr(II) in the aqueous phase; $V_{0\mathrm{Aq}}$ and V_{Aq} (mL) indicate the volume of the aqueous phase before and after extraction, V_{IL} (mL) the volume of the ionic liquid phase after extraction.

Results and Discussion

Extraction capability of Ionic liquids

The comparison of Cs(I) and Sr(II) extraction with three ILs is shown in Table 1. As

shown in Table 1, the extraction capability keeps an order of C_2mimNTf$_2$ > C_4mimNTf$_2$ > C_6mimNTf$_2$. The data show that extraction capability of Cs(I) and Sr(II) decreased with the length of the alkyl carbon chain on the imidazolium ion under same conditions. This result shows that the extraction capability for the metal ions indicates a strong preference for the aqueous phase.

Effect to extraction capability using crown ethers

The extraction results of Cs(I) and Sr(II) by B18C16, DB18C6 in three ILs under same conditions is shown in Table 2. As shown in table 2, the high extraction performance was observed for the Cs(I) and Sr(II) ions when ILs had shorter alkyl chains in the imidazolium cation. Moreover, the extraction capability with B18C6 was higher than DB18C6. It can be presumed that this reason is difference in the solubility in the metal ion / 18C6 complex. In addition, Xu et al. reported extraction capability of $C_n$mim-NTf$_2$/ dicyclohexano-18-crown-6 (DCH18C6) system[7]. The extraction ratio of Sr in $C_n$mim-NTf$_2$/ B18C6 is lower than $C_n$mim-NTf$_2$/DCH18C6.

Effect of HNO_3 concentrations

HLLW can be employed over a wide range of HNO_3 concentrations, with high salt content and radioactivity. Therefore, it is quite necessary to study the effects of HNO_3 concentration on the extraction of Cs(I) and Sr(II). Figures 1 and 2 show the dependence of the extraction efficiency of Cs(I) and Sr(II) on the initial HNO_3 concentrations in aqueous phase of D18C6 and DB18C6/$C_n$mimNTf$_2$. E_{Cs} in all three systems decreases with the increase of the HNO_3 concentration. However, E_{Sr} in three systems increases when HNO_3 concentration exceeds 0.5 M. Within the acidity range studied, the extraction efficiency of Cs(I) and Sr(II) keeps an order of C_2mimNTf$_2$ > C_4mimNTf$_2$ > C_6mimNTf$_2$. Similar results were found in a study done by Visser et al.[8]. It was found that distribution ratio indicated a minimum value at 1 M-HNO_3, followed by a sharp increase at higher acid concentrations in C_4mim-PF$_4$/DtBuCH18C6 system. Moreover, they explained distribution ratios decrease as the water content of the IL phase decreases. This result is consistent with the finding reported by Visser's investigation[8]. In this study, the IL used for extraction was not saturated with nitric acid. Therefore, it is quite likely that the increase in E_{Sr} is due to increasing aqueous concentrations of IL phase. On the other hand, several studies have reported that extraction ratio (or distribution ratio) decreases with the increase of the HNO_3 concentration. Xu et al. have shown that the competition of H^+ might be the leading factor

which causes an overall decrease in the extraction efficiency[7]. In the same manner, it is possible that competition of H^+ is accounted for the decrease in E_{Cs} with the increase of the HNO_3 concentration.

Conclusions

The extraction of Cs(I) and Sr(II) ions using B18C6 and DB18C6 as the extractant and three $C_n$mimNTf_2 ionic liquids as solvents has been investigated. Detailed work on the influences of HNO_3 solution showed that the results were significantly different from those of solvent extraction. With the present system, a special low acidity extraction behavior has been revealed, which may provide an alternative way for extraction of Cs(I) and Sr(II) ions under low acidity HLLW conditions, avoiding the use of a high concentration of HNO_3 when conventional solvents are used.

References

1) Suzuki A., et al., *JAEA-Rev.* 2008-037 (2008).
2) Mimura H., et al., *J. Nucl. Sci. Technol.* **22** (1985) 284.
3) Mimura H., et al., J. *Nucl. Sci. Technol.* **27** (1990) 835.
4) Luo M., et al., *Energy Procedia* **39** (2013) 434.
5) Chen P. Y., et al., Electrochim. Acta, 49 (2004) 5125.
6) Dai.S., et al., *J. Chem., Dalton Trans.* **8** (1999) 1201.
7) Xu C., et al., *Sci. China. Ser. B Chem.* **52** (2009) 1858.
8) Visser A.E., et al., *Ind. Eng. Chem. Res.* **39** (2000) 3596.

Table 1. Extraction efficiency of Cs(I) and Sr(II) in ILs (Not use crown ether).

		C_2mimNTf_2	C_4mimNTf_2	C_6mimNTf_2
0.1M-HNO_3	E_{Cs} (%)	44.2	19.2	4.4
	E_{Sr} (%)	4.9	4.5	1.9

[Cs^+]=5mM, [Sr^{2+}]=5mM

Table 2. Extraction efficiency of Cs(I) and Sr(II) achieved by using 18C6 in ILs.

		C_2mimNTf$_2$	C_4mimNTf$_2$	C_6mimNTf$_2$
B18C6	E_{Cs}(%)	70.4 (+26.2)	60.4 (+41.2)	49.6 (+45.2)
	E_{Sr}(%)	72.0 (+67.1)	32.9 (+28.4)	9.4 (+5.0)
DB18C6	E_{Cs}(%)	57.6 (13.4)	36.6 (+17.4)	17.3 (+12.9)
	E_{Sr}(%)	8.6 (+3.7)	4.5 (0)	2.4 (+0.5)

[Cs^+] = 5mM, [Sr^{2+}] = 5mM, [H^+] = 0.1M, [18C6] = 10mM

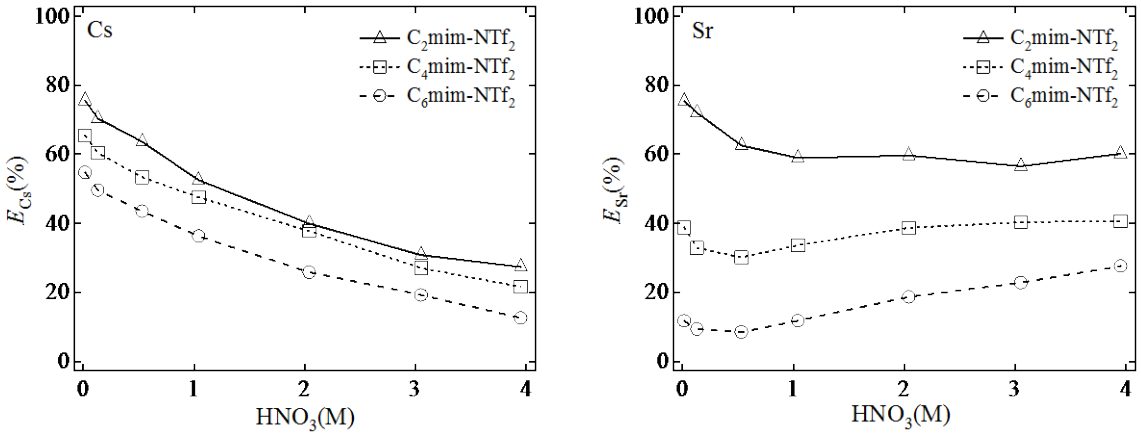

Figure 1. Dependence of E_{Cs} and E_{Sr} on HNO_3 concentration. aqueous phase: 5mM Cs(I) and Sr(II) in 0.01M to 4M HNO_3. Organic phase: 10mM B18C6/$C_n$mimNTf$_2$.

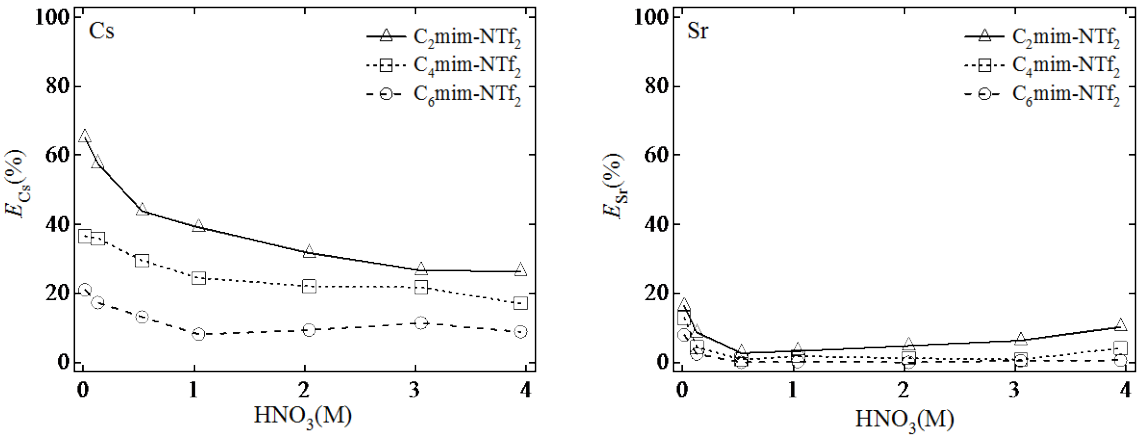

Figure 2. Dependence of E_{Cs} and E_{Sr} on HNO_3 concentration. aqueous phase: 5mM Cs(I) and Sr(II) in 0.01M to 4M HNO_3. Organic phase: 10mM DB18C6/$C_n$mimNTf$_2$.

VI. 6. Development of Measurement Systems Using an Aqueous Solution of *N,N*-Dimethylformamide for Gaseous Radioactive Methyl Iodide in Nuclear Power Plant Accidents

Tokuda H.[1,3], Kim S.-Y.[2], Takahashi T.[2,3], Hasegawa S.[2,3], Hitomi K.[2], and Ishii K.[2]

[1]Cyclotron and Radioisotope Center, Tohoku University
[2]Department of Quantum Science and Energy Engineering, Tohoku University
[3]Japan Nuclear Fuel Limited

Introduction

Radioactive methyl iodide (CH_3I) mainly comes into the gaseous phase during meltdown in nuclear power plant accidents[1,2]. Radioactive iodine isotopes of ^{131}I and ^{133}I having half-lives of about 8 days and 20 hours exhibit high radioactivity, respectively. These are concern in the public exposure particularly, if an accident occurs during operations in nuclear power plant. Therefore, the measurement of gaseous radioactive methyl iodide is an important for the radiation exposure control.

Generally, triethylenediamine (TEDA) impregnated activated carbon filter cartridge is used for sampling of the radioactive methyl iodide in the air[3-5]. Recently, the cartridge is known to have decreased sampling efficiency by the passage quantity of water[6]. When the passage quantity of water exceeds 4,000 g/cartridge, it lowers the sampling efficiency and then the rate of decrease reaches approximately 40% in 12,000 g/cartridge. The measurement of the gaseous radioactive methyl iodide might become difficult because a large quantity of water is released by a steam vent in nuclear power plant accidents.

The methods of gas phase capture of iodine include solid adsorbents of the dry process and wet scrubbing methods[7-14]. Table 1 summarizes the solid absorbents and wet scrubbing techniques available for iodine capture. It is difficult to maintain the sampling efficiency of the adsorbent of the dry process for a large quantity of water in gas. As for the wet scrubbing methods using the aqueous solution, the sampling efficiency is more likely to be maintained. However, the wet methods put to practical use are only alkali scrub, and the decontamination factor of alkali scrub for organic iodine is less than 1. Therefore, the choice of suitable liquid absorber that is practical and useful easily is necessary.

We have been focusing on the method that it is easy to decompose CH_3I into an iodide ion by S_N2 reaction known widely. DMF (*N*,*N*-dimethylformamide) that is a polar aprotic solvent can dissolve gaseous methyl iodide. In DMF and the aqueous mixture of the nucleophile (OH^-), CH_3I is decomposed into an iodide ion by nucleophilic substitution and then iodide ions are fixed in the aqueous solution as a leaving group[15,16]. We want to propose a new measurement system using its mechanism for gaseous radioactive methyl iodide in nuclear power plant accidents.

In this study, we have attempted to capture CH_3I using the DMF/NaOH solution and to recovery iodine from it with ion-exchange resin, and then by combining them to examine the measurement system of radioactive methyl iodide in the accident.

Experimental

Materials

CH_3I was purchased from Kanto Chemical Co. Other chemicals such as DMF and NaOH were of reagent grade supplied by Wako Pure chemical Industries, Ltd. Ion-exchange resin (IRA910CT) was purchased from Organo Co.

Absorber and Gas Sampler

The production of iodide ion that is a degradation product of CH_3I was estimated by batch method in the absorber. An aqueous solution (5 cm^3) containing 500 mM NaOH, 100 mM CH_3I and 5 vol% to 90 vol% DMF was stirred at 25°C during 30 min. The concentration of iodide ion in the solution was measured by ion chromatography.

The vapors of CH_3I were produced from an evaporation of liquid methyl iodide. Gas-phase concentration was adjusted by air flow rate to methyl iodide generator including 0.02 cm^3 of liquid methyl iodide (0.32 mmol). Room air was used as a carrier gas at 100 cm^3/min. The absorber contained 100 cm^3 of the DMF/NaOH solution. In the gas sampler, methyl iodide contained in the gas-phase reacted completely with the DMF/ NaOH solution in the absorber to form iodide ions. The amount ratio (Q/Q_0) was calculated as the ratio for the initial value.

Determination of Distribution Coefficient

The distribution of iodide ion was estimated by batch method. The DMF/NaOH solution (10 cm^3) containing 10 mM CH_3I and 1 to 100 mM NaOH was contacted with 0.1

g of IRA910CT at 25°C up to 1 h, which was found to be sufficient for attaining equilibrium. The distribution coefficient (K_d) is defined as,

$$K_d = (C_o - C_f)/C_f \times (V/m), (cm^3/g) \quad (1)$$

where C_o and C_f denote iodide ion concentration (mM) in the aqueous phase before and after adsorption, respectively. V (cm^3) indicates the volume of the aqueous phase and m (g) is the weight of dry absorbent.

Column Operation

The column was prepared by packing the IRA910CT in a glass column with thermostatic water jacket. The simulated dissolution of CH_3I, after the reaction in the gas sampler, was passed through the column. Elution of the column was carried out by flowing 2 M NaCl as eluent.

Results and Discussion

Effect of DMF volume on substitution

Figure 1 (a) shows the reaction product, iodide ion, of 100 mM CH_3I at d 5 vol% to 90 vol% DMF with 100 mM NaOH. Concentrations of iodide ion tend to increase with increasing DMF volume of 5 vol% to 30 vol%. In the volume of 30 to 90 vol%, the iodide ion concentration showed a constant value and it was equivalent to the initial concentration of CH_3I. This effect is due to nucleophilic substitution of a pair of a nucleophile (Nu) and leaving group (X). The nonbonded pair of nucleophile (hydroxide ion) forms the new Nu-C bond at the same time the leaving group (iodide ion) goes off with the C-X bonding pair. Figure 1 (b) shows the time-course of iodide ion at each volume: DMF/water (v/v) is 30/70, 50/50 and 70/30. At the beginning of the reaction, concentrations of iodide ion increased with time and then reached an equilibrium state by 30 min with each case. Until this 30 min, the reaction rate was high at high ratio of volume of DMF.

Capture of CH_3I on absorber

Figure 2 shows the time-course of adsorption of CH_3I at the absorber that is DMF/water (v/v): 30/70 with 100mM NaOH. At the beginning, the amount ratio (Q/Q_0) of iodine tends to increase linearly until 60 min and then reached 77% of the initial amount 120 min later. The increment was lower from around 60 min as a result that all liquid methyl iodide was volatilized. It is thought that remaining 20% moved to outside the

system.

Effect of NaOH concentration on K_d

Figure 3 shows adsorption ability of IRA910CT for iodide ions at different concentrations of 1 to 100 mM NaOH in mixed solvents of DMF/water (v/v:30/70). K_d value tends to decrease with increasing NaOH concentration of 10 to 100 mM and relatively small K_d value above 100 cm^3/g was obtained around 100 mM NaOH. This result shows that recovery of iodine is possible from the absorber using the DMF/NaOH solution.

Chromatographic Separation

Figure 4 shows the chromatogram of iodide separation from the DMF/ NaOH solution that is absorption using IRA910CT packed column. It was shown that a well-resolved chromatogram was obtained. Most of iodide ions were readily broken through column and effectively eluted with 2 M NaCl.

Figure 5 shows the concept of the gaseous radioactive methyl iodide measurement system. These findings indicated that the measurement system of radioactive methyl iodide in the accident can be performed as following steps: at first, the sampling air including radioactive methyl iodide with a large quantity of water is passed through the absorber using the DMF/NaOH solution, and then the resulting iodide ion is adsorbed by ion-exchange resin. Then, it is recovered with eluent of 2 M NaCl.

Conclusion

The DMF/NaOH solution abstracted iodide ion from CH_3I, and it was performed fast by the solution containing 70 vol% water, and then reached equilibrium within 30 min. The iodine recovery rate of the absorber (DMF/water (v/v) is 30/70 with 100 mM NaOH) was reached to 77%, 120 min later. The K_d value of IRA910CT for iodide ion was 10^2 to 10^3 in the DMF/NaOH solution. Iodide ions adsorbed on the top of the column were chromatographically eluted with 2 M NaCl.

The results suggested that absorber using the DMF/NaOH solution was effective for capture of CH_3I and recovery of iodide ion from the absorber, and the proposed process was feasible for practical application.

References

1) Buxton G.V., Sims H.E., *Rad. Phys. Chem.* **67** (2003) 623.

2) Ishikawa J., Moriyama K., *JAEA-Res*. 2010-051 (2011).
3) Fukuda S., Naritomi M., *Nucl. Technol.* **7** (1970) 450.
4) Naritomo M., Yoshida Y., *Nucl. Technol.* **10** (1973) 292.
5) Park S. W., Park H. S., et al., *Sep. Technol.* **5** (1995) 35.
6) Koarashi J., Mikami S., et al., *JAEA-Technol*. 2010-039 (2010).
7) Kitami S., Noro T., Kohara T., *Nucl. Technol.* **9** (1972) 197.
8) Takami T., Ohyoshi E., et al., *Nucl. Technol.* **13** (1976) 219.
9) Adachi M., Eguchi W., Haoka T., *Nucl. Technol.* **14** (1977) 370.
10) Adachi M., Eguchi W., Tsukada R., *Nucl. Technol.* **15** (1978) 40.
11) Matsuoka S., Nakamura H., et al., *Nucl. Technol.* **21** (1984) 862.
12) Kondo Y., Funabashi K., *Nucl. Technol.* **31** (1994) 1073.
13) Takeshita K., Takashima Y., *Nucl. Technol.* **32** (1995) 941.
14) Haefner D. R., Tranter T. J., *INL/EXT*-07-12299 (2007).
15) Asahara T., Seno M., Arai T., *Seisan-kenkyu* **19** (1967) 156.
16) Katritzky A. R., et al.,Recu. des *Trav. Chim*, **110** (1991) 369.

Table 1. Summary of the solid absorbents and wet scrubbing techniques available for iodine capture.

(a) Solid adsorbents

Absorbent	Temperature (^{o}C)	Comments
Activated carbon	< 120	High humidity may adversely affect performance
Macroreticular resins	< 50	High humidity may adversely affect performance
AgA, AC6120, AgX, AgZ, Ag°Z - silver based adsorbent	~ 150 ~ 130 (AC6120)	High temperature is necessary to avoid influence of the humidity.

(b) Wet scrubbing techniques

Process	Scrub solution	Decontamination factor for organic iodine	State of Development
Caustic scrub	1 to 2 M NaOH	~ 1	Deployed at full scale
Mercurex	0.2 to 0.4 M $Hg(NO_3)_2$ 14 M HNO_3	10^2 to 10^4	Pilot scale
Iodox	20 to 23 M HNO_3	> 10^4	Pilot scale
Fluorocarbon	CCl_2F_2 (Freon R-12)	10^4	Pilot scale
Electrolytic scrubbing	8 to 12 M HNO_3 0.1 M Co^{3+}	100	Lab scale
Silicon-organic liquid	Polymethylsiloxane	~ 1	Lab scale
Molten hydroxide	NaOH or KOH	-	Lab scale

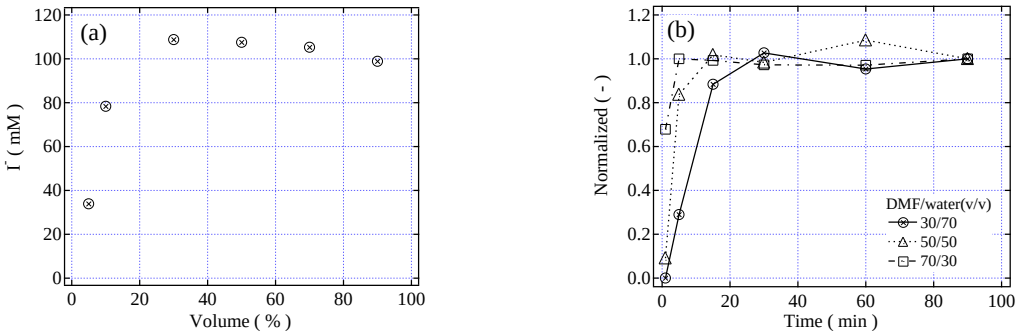

Figure 1. Effects of DMF volume on nucleophilic substitution of CH_3I.

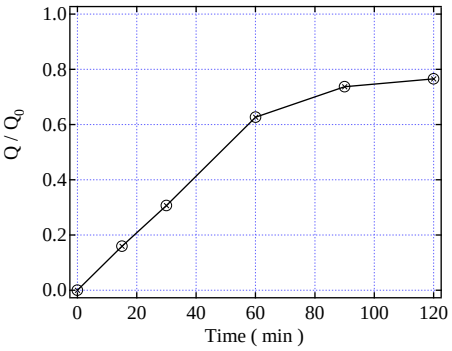

Figure 2. Capture of methyl iodide on absorber.

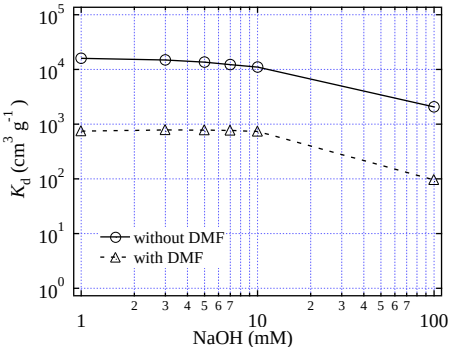

Figure 3. Effects of NaOH concentration on K_d.

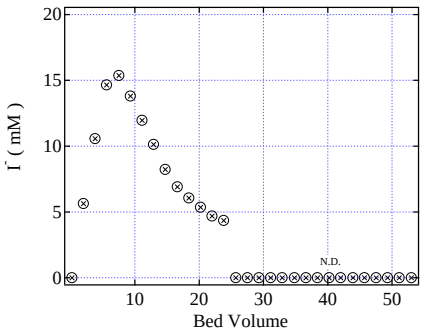

Figure 4. Chromatographic separation of absorbent through IRA910CT column.

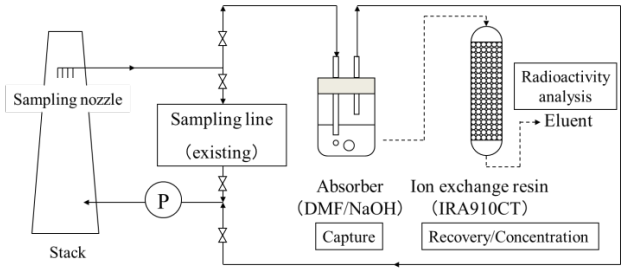

Figure 5. Concept of the gaseous radioactive methyl iodide measurement system.

VII. RADIOPHARMACEUTICAL CHEMISTRY AND BIOLOGY

VII. 1. Synthesis and Preclinical Evaluation of a Fluorine-18 Labeled BF-227 Derivative

Furumoto S.[1], Okamura N.[2], Ishikawa Y.[1], Iwata R.[1], Yanai K.[2], Tashiro M.[1], Furukawa K.[3], Arai H.[3], and Kudo Y.[3]

[1]Cyclotron and Radioisotope Center
[2]Tohoku University School of Medicine
[3]Institute of Development, Aging and Cancer, Tohoku University

Introduction

Alzheimer's disease (AD) is an age-dependent and irreversible neurodegenerative disorder leading to deterioration of memory and cognitive functions and the most common form of senile dementia. Although the exact mechanisms underlying pathogenesis of AD are not fully understood, formation of brain amyloid plaques through aggregation and deposition of β-amyloid proteins (Aβ) is considered to be the initial pathogenic event which precedes the appearance of clinical AD symptoms by decades. Thus, a non-invasive approach for detecting the amyloid plaques in the living brain could hold considerable promise for more accurate antemortem diagnosis of AD in the early and perhaps pre-symptomatic phases of AD. For that purpose, many PET tracers have been reported to date, such as ^{11}C-PiB, ^{11}C-SB-13, ^{18}F-florbetapir, ^{18}F-flutemetamol, ^{18}F-florbetaben and so on[1)]. We also had reported that ^{11}C-BF-227 is a promising PET ligand for in vivo detection of dense amyloid deposits in AD patients. Considering accessibility of the ligand, development of a new BF-227 derivative labeled with fluorine-18, which has a longer half-life than carbone-11, would be valuable. In this study, we synthesized several kinds of ^{18}F-labeled analogues of BF-227 and examined their feasibility for in vivo amyloid imaging[2)].

Methods

Fluorine-18 labeled derivatives of BF-227 were newly designed and synthesized as indicated in Fig. 1. The fluoroethoxy and dimethylamino groups of BF-227 were modified to optimize the probe properties for amyloid imaging. To confirm binding of these

compounds to amyloid plaques, fluorescent staining of AD brain sections with them. Biodistribution study using the ^{18}F-labeled derivatives and normal ICR mice was conducted to assess their brain kinetics and in vivo defluorination. Through these experiments, we selected ^{18}F-THK-763 as a potent agent for amyloid imaging. Binding nature of ^{18}F-THK-763 to Aβ plaques was evaluated by in vitro binding assay using Aβ fibrils, in vitro autoradiography (ARG) of AD brain sections, and ex vivo ARG of the brain of APP23 mouse and wild type one. Additionally, small animal PET imaging was performed using APP23 in comparison to ^{11}C-PiB. Finally, ability of of ^{18}F-THK-763 (^{18}F-FACT) to image amyloid depositions was preliminarily evaluated through human PET imaging study in AD patients.

Results and Discussion

Fluorescent staining of the AD brain sections revealed that senile plaques were clearly stained by the fluorinated BF-227 derivatives. Biodistribution study of the ^{18}F-labeled derivatives in normal mice elucidated that ^{18}F-THK-763 possesses the most favorable in vivo properties; rapid brain uptake (4.64 %ID/g at 2min), fast clearance from the normal brain without non-specific binding (0.28 %ID/g at 60min), and resistance to metabolic defluorination (low radioactivity uptake in bone) (Fig. 2). In addition, in vitro binding assay showed that ^{18}F-THK-763 binds to Aβ fibrils with a high binding affinity (Kd: 3.6 nM). ARG study using AD brain sections indicated a specific binding of ^{18}F-THK-763 to the cerebral amyloid plaques. Ex vivo ARG of the brain of APP23 mouse (Fig. 3A) and wild type mouse (Fig. 3B) using ^{18}F-THK-763 also demonstrated that the radioactive spots (Fig. 3C) were observed only in the APP-mouse brain and the distribution was identical (Fig. 3D) to that of amyloid plaques labeled with Thioflavin-S (Fig. 3E). PET images of wild-type and APP transgenic mice indicated that amyloid deposits in the cerebral cortices of APP23 mice were clearly visualized with the same distribution pattern between ^{18}F-THK-763 and ^{11}C-PiB. PET imaging in the normal aged (NA) subject and AD patient, still preliminary, showed significantly higher ^{18}F-THK-763 uptake in the neocortex compared to NA subjects. Significant correlation between regional SUVR of ^{18}F-THK-763 and ^{11}C-BF-227 were observed in 2 AD patients and one NA subject.

Conclusions

In conclusions, we had succeeded in developing a new ^{18}F-labeled amyloid

tracer, ^{18}F-THK-763. It showed a rapid and an adequate brain uptake, smooth washout from the normal mouse brain, no metabolical defluorination in vivo, a high binding affinity to Aβ fibrils and plaques, and a high retention in the brain regions containing amyloid plaques in both APP23 mice and AD patients by PET. These results strongly suggest that ^{18}F-THK-763 has enough potential for in vivo imaging of amyloid deposits in the AD brain.

References

1) Furumoto S, Okamura N, Iwata R, Yanai K, Arai H, Kudo Y., *Curr. Top. Med. Chem.* **7** (2007) 1773.
2) Furumoto S, Okamura N, Furukawa K, et al., *Mol. Imaging Biol.* **15** (2013) 497.

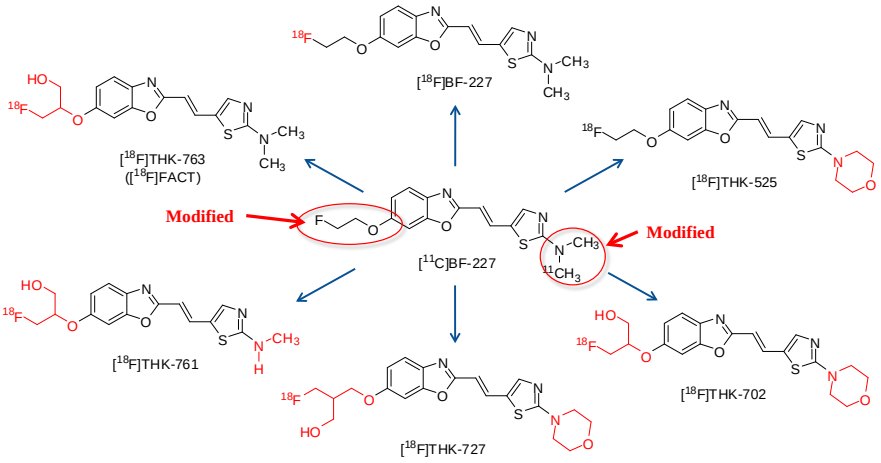

Figure 1. Fluorine-18 labeled BF-227 derivatives synthesized and evaluated in this study.

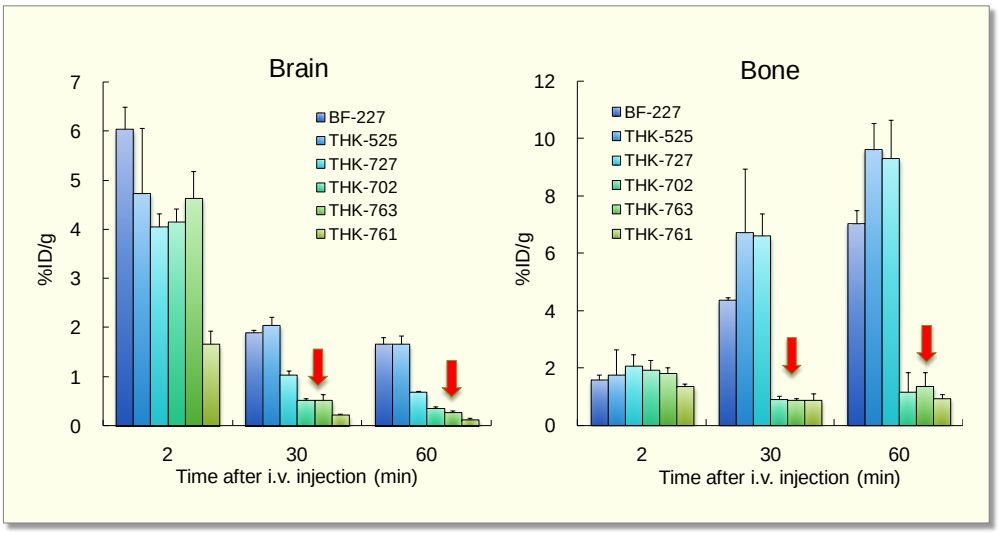

Figure 2. Radioactivity uptakes in the brain and bone of normal mice (n=4) after i.v. injection of the ^{18}F-labeled derivatives.

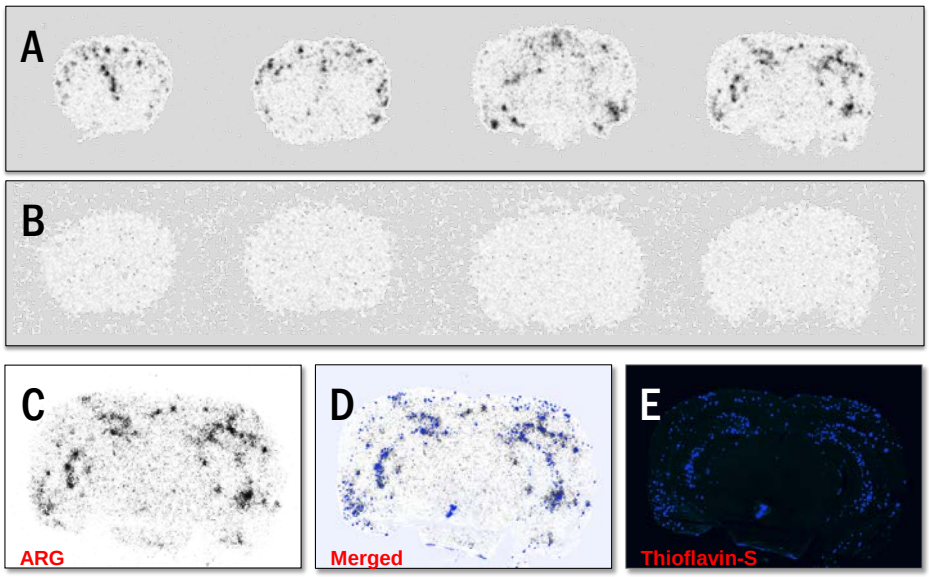

Figure 3. Ex vivo ARG of the brain of APP23 mouse and wild type one.

VII. 2. Preliminary Evaluation of 2-Arylhydroxyquinoline Derivatives for Tau Imaging

Tago T.[1,2], Furumoto S.[1,3], Okamura N.[4], Harada R.[5], shikawa Y.[2], Arai H.[5], Yanai K.[4], Iwata R.[1], and Kudo Y.[5]

[1]Cyclotron and Radioisotope Center, Tohoku University,
[2]Graduate School of Pharmaceutical Sciences, Tohoku University
[3]Frontier Research Institute for Interdisciplinary Sciences, Tohoku University
[4]Department of Pharmacology, Tohoku University School of Medicine
[5]Institute of Development, Aging and Cancer, Tohoku University

Introduction

Alzheimer's disease (AD) is a major causative disorder of dementia. In the brains of AD patients, amyloid-β (Aβ) plaques and hyperphosphorylated-tau tangles are observed as characteristic neuropathology of AD. These pathologies are thought to start a gradual accumulation before the onset of clinical signatures of AD. Therefore, the non-invasive quantitative techniques for these pathologies would make an invaluable role to estimation of the severity of AD. We have reported 2-arylquinoline derivatives as tau probes for positron emission tomography (PET)[1,2]. In the optimization of tau probes, the adjustment of lipophilicity of compounds is an important factor which affects the quality of PET images. The purpose of this study was to evaluate the characteristics of novel hydroxyquinoline derivatives with low lipophilicity as tau PET probes[3].

Materials and Methods

Fluorescent staining using AD hippocampal sections was performed in accordance with the regulations of the ethics committee of Tohoku University. The sections were immersed in a 100 μM compound solution containing 50% ethanol for 10 min. Competitive binding assay using [^{18}F]THK-523 and recombinant K18Δ280K tau aggregates was performed as described previously[2]. [^{11}C]THK-951 was radiosynthesized by the reaction of its precursor and [^{11}C]MeOTf. [^{11}C]MeOTf was bubbled through a DMSO solution containing the precursor and tBuOK, followed by heating at 100 °C for 1 min. 2 N HCl was added to the solution and it was heated for 10 min at the same temperature. After

neutralization with 4 N NaOH, the crude mixture was purified by semi-preparative HPLC. *Ex vivo* biodistribution assay in normal mice was performed as described previously[2]. This experiment was approved by the Committee on the Ethics of Animal Experiments at Tohoku University.

Results and Discussion

We synthesized six 2-arylhydroxyquinoline derivatives as tau PET probe candidates (Table 1). In terms of log P values, five of six compounds showed lower lipophilicity (Log P $\leq$ 1.59) than probes which we previously reported[2]. The result of fluorescent staining using AD brain sections is summarized in Table 1. 2-Phenylquinoline derivatives clearly stained tau tangles according with tau immunostaining. The result of competitive binding assay is described in Table 1. Three compounds, THK-951, 14R301 and 14R306, with relatively high log P values showed lower Ki values.

Following these results, we selected THK-951 for biodistribution study. To radiolabel *N*-methyl group of THK-951 with carbon-11, a precursor was reacted with [^{11}C]MeOTf (Fig. 1). [^{11}C]THK-951 was obtained with 39% of radiochemical yield (decay corrected) and higher than 99% of radiochemical purity. The average specific activity of [^{11}C]THK-951 was 83.2 GBq/μmol. To evaluate the brain kinetics of [^{11}C]THK-951, we performed an *ex vivo* biodistribution study in normal mice (Fig. 2). [^{11}C]THK-951 showed a high brain uptake immediately after the injection, and then it was eliminated rapidly from the brain by 30 min post-injection. The radioactivity in the blood also showed a fast clearance. To evaluate the rate of elimination from the brain quantitatively, 2-min-to-30-min uptake ratio was calculated. The ratio of [^{11}C]THK-951 was 21.5 and this value was higher than other THK tau probes[2]. This result suggests that [^{11}C]THK-951 will give high contrast images in the future *in vivo* PET studies in AD human patients or model animals.

Conclusion

In this study, low lipophilic hydroxyquinoline derivatives were evaluated as candidates of tau PET probes. They showed binding affinity to tau aggregates in the *in vitro* binding assay and fluorescent staining with AD brain sections. [^{11}C]THK-951 was radiosynthesized and its excellent brain kinetics in normal mice was revealed by the *ex vivo* biodistribution study. Future evaluation of [^{11}C]THK-951 and the structural optimization will give the high performance tau imaging technique.

References

1) Okamura N, Suemoto T, Furumoto S, et al., *J. Neurosci.* **25** (2005) 10857.
2) Okamura N, Furumoto S, Harada R, et al., *J. Nucl. Med.* **54** (2013)1420.
3) Tago T, Furumoto S, Okamura N, et al., *J. Label. Compd. Radiopharm.* **57** (2014) 18.

Table 1. Summary of evaluation results of hydroxyquinoline derivatives.

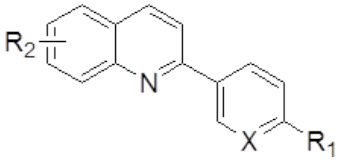

Compound name	X	R_1	R_2	log P	AD tau[a]	Ki (nM)[b]
THK-951	C	$NHCH_3$	7-OH	1.28	++	21
THK-953	N	$NHCH_3$	7-OH	0.56	-	110
THK-5272	C	NH_2	6-OH	0.61	+	36
14R301	C	$NH(CH_3)_2$	6-OH	2.37	++	2.4
14R306	C	$NHCH_3$	6-OH	1.59	+	1.6
THK-5273	N	$NHCH_3$	6-OH	0.90	+/-	30

[a]Results of fluorescent staining assay with AD brain sections.
[b]Results of competitive binding assay.

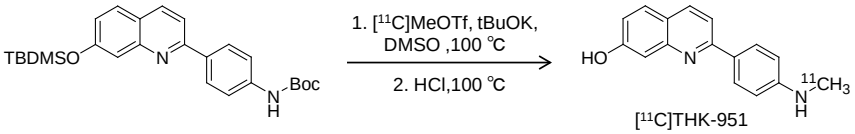

Figure 1. Radiosynthesis of [^{11}C]THK-951.

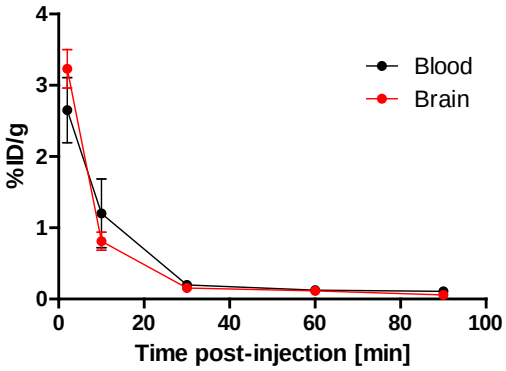

Figure 2. Time-activity curves after intravenous injection of [^{11}C]THK-951 in normal mice. Curves represent the mean value ± SD.

VII. 3. Comparison of the Binding Properties of Tau PET Radiotracer ^{18}F-THK523 and Other Amyloid PET Tracers to Alzheimer's Disease Pathology

Harada R.[1], Okamura N.[1,2], Furumoto S.[3,4], Tago T.[4], Yoshikawa T.[2], Arai H.[1], Iwata R.[4], Yanai K.[2], and Kudo Y.[1]

[1]*Institute of Development, Aging and Cancer, Tohoku University*
[2]*Department of Pharmacology, Tohoku University School of Medicine*
[3]*Frontier Research Institute for Interdisciplinary Science, Tohoku University*
[4]*Cyclotron and Radioisotope Center, Tohoku University*

Introduction

Alzheimer's disease (AD) is characterized by the protein depositions such as senile plaques and neurofibrillary tangles, which consist of amyloid-β (Aβ) and tau protein, respectively. In vivo amyloid imaging techniques provided useful information on presymptomatic Aβ pathology[1)]. Tau pathology is correlated with neuronal loss and cognitive decline and thought to begin before extensive neuronal loss occurs. Thus, non-invasive detection of tau pathology in AD would provide new insights such as early diagnosis, monitoring disease progression, and evaluating anti-tau therapies. Recently, ^{18}F-THK523 was developed as a potential tau PET tracer[2)]. This study reports comparison of binding characteristics of ^{18}F-THK523 and other amyloid PET tracers such as ^{18}F-FDDNP, ^{11}C-PiB, and ^{11}C-BF-227 to AD pathology[3-5)]. (Fig. 1)

Methods

In vitro saturation binding assays were conducted using synthetic amyloid-β_{42} and recombinant tau (K18ΔK280) fibrils. Non-specific binding was determined by the addition of unlabeled compounds at a concentration of 2 μM. Binding parameters such as K_d and B_{max} were calculated using GraphPad Prism 5. To examine binding ability to neuropathological lesions, in vitro autoradiography was conducted using sections of AD brain. The neighboring sections were stained by Gallyas Braak staining and immunohistochemistry (AT8 (tau) and 6F/3D (Aβ) antibodies).

Results

In vitro saturation binding assay indicated that ^{18}F-THK523 bound to tau fibrils (K_d = 1.99 nM) with higher affinity than Aβ fibrils (K_d = 30.3 nM). In contrast, the other amyloid PET tracers such as ^{18}F-FDDNP, ^{11}C-PiB, and ^{18}F-BF227 showed a higher affinity for Aβ fibrils (K_d < 10 nM). To further evaluate the binding selectivity of ^{18}F-THK523, in vitro autoradiography was conducted using postmortem brain sections from AD patients and compared with other amyloid PET tracers. ^{11}C-PiB showed diffuse patchy binding pattern in the frontal gray matter, while ^{18}F-THK523 binding was considerably lower. In the medial temporal brain sections from AD patients, ^{11}C-PiB and ^{11}C-BF227 did not accumulate in the hippocampal CA1/subiculum, whereas ^{18}F-THK523 did accumulate in this area. The presence of a high density of tau deposition and a low density of Aβ in this area was confirmed by immunohistochemistry (Fig. 2). ^{18}F -FDDNP showed no remarkable binding to AD brain sections (data not shown), which was consistent with previous report[6]. In the high magnification images, the distribution of ^{18}F-THK523 closely resembled Gallyas silver staining and tau immunostaining. ^{18}F-THK523 labeling in the layer pre-α of the entorhinal cortex corresponded to Gallyas silver staining (Fig. 2). In contrast to ^{18}F-THK523, ^{11}C-PiB binding corresponded to Lake-like amyloid in the parvopyramidal layer of the presubicular area and in the layers pre-β and pre-γ of the entorhinal cortex.

Conclusions

In conclusion, the binding profiles of ^{18}F-THK523, ^{11}C-PiB, ^{18}F-BF227, and ^{18}F-FDDNP were compared using in vitro saturation binding assays and autoradiography for AD brain sections. These data suggest that ^{18}F-THK523 shows a binding preference for tau aggregates. Therefore, ^{18}F-THK523 is a candidate as a tau PET radiotracer to identify tau pathology. Recently, Melbourne group have reported that ^{18}F-THK523 can selectively bind to tau pathology in the patients with Alzheimer's disease, despite there are several drawbacks such as problematic high white matter retention[7]. Further compound optimization is needed to obtain high signal-to-background ratio of PET images.

References

1) Nordberg A, Rinne JO, Kadir A, Langstrom B., *Nat. Rev. Neurol.* **6** (2010) 78.
2) Fodero-Tavoletti MT, Okamura N, Furumoto S, Mulligan RS, Connor AR, McLean CA., et al., *Brain* **134** (2011) 1089.
3) Shoghi-Jadod, Small GW, Agdeppa ED, Kepe V, Ercoli LM, Siddarth P., et al., *Am. J. Geriatr.*

Psychiatry **10** (2002) 24.
4) Klunk WE, Engler H, Nordberg A, Wang Y, Blmqvist G, Holt DP., et al., *Ann. Neurol.* **55** (2004) 306.
5) Kudo Y, Okamura N, Furumoto S, Tashiro M, Furukawa K, Maruyama M., et al., *J. Nucl. Med.* **48** (2007) 553.
6) Thompson PW, Ye L, Morgenstern JL, Sue L, Beach TG, Judd DJ., et al., *J. Neurochem.* **109** (2009) 623.
7) Villemagne VL, Furumoto S, Fodero-Tavoletti MT, Mulligan RS, Hodges J, Harada R., et al., *Eur. J. Nucl. Med. Mol. Imaging* **41** (2014) 816.

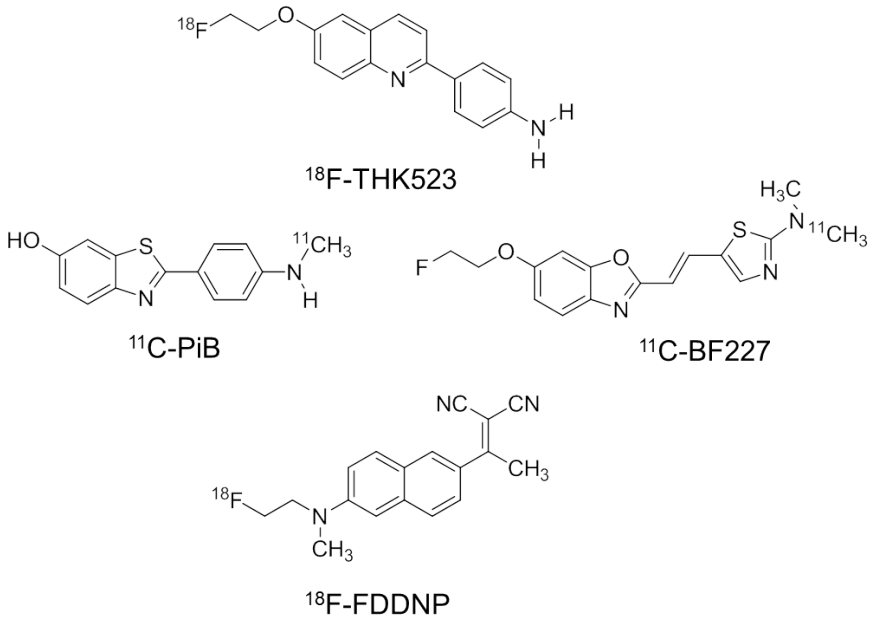

Figure 1. Chemical structures of ^{18}F-THK523, ^{11}C-PiB, ^{11}C-BF227, and ^{18}F-FDDNP.

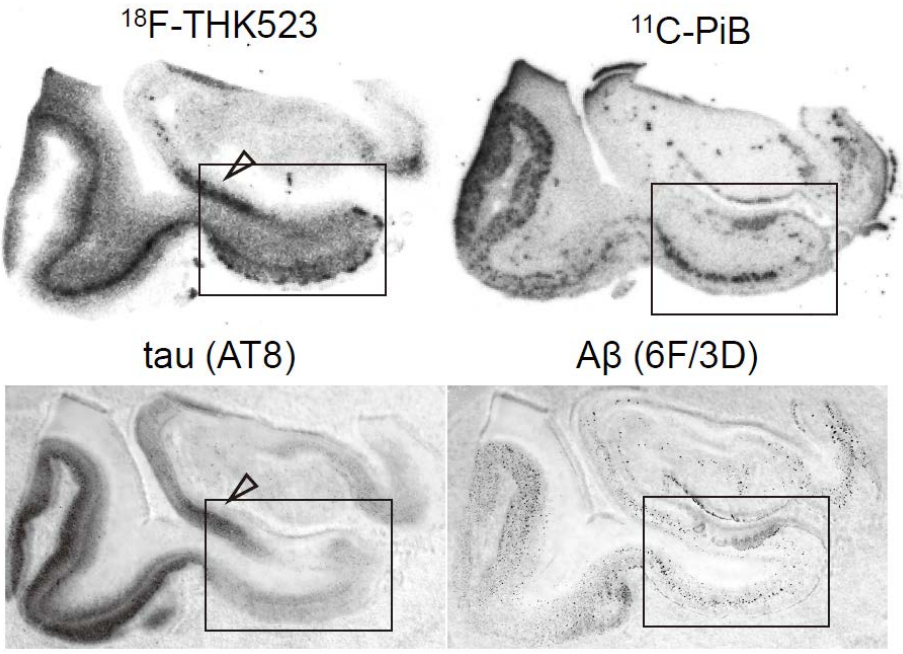

Figure 2. Comparison of ^{18}F-THK523 and ^{11}C-PiB autoradiographic images and tau and Aβ immunohistochemistry in the medial temporal brain sections from an AD patient.

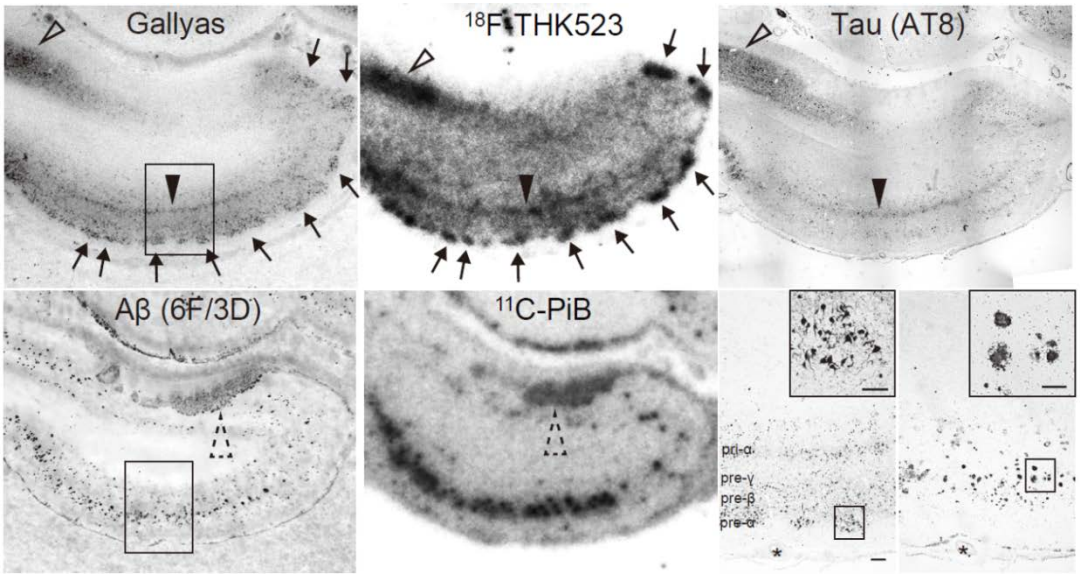

Figure 3. High magnification images of the medial temporal section from AD patient. Many clusters of ^{18}F-THK523 binding in the entorhinal cortex are consistent with Gallyas silver staining (Arrows). Lake-like amyloid in the presubicular region is labeled with ^{11}C-PiB, but not with ^{18}F-THK523. Aβ plaques located in the layer pre-β and pre-γ are intensely labelled with ^{11}C-PiB. Asterisks denote the same large vessel.

VIII. NUCLEAR MEDICINE

VIII. 1. Radiation Dosimetry of the F-18 Labelled Amyloid Imaging Probe [^{18}F]FACT in Humans

Shidahara M.[1,2], Tashiro M.[2], Okamura N.[3], Furumoto S.[3], Furukawa K.[4], Watanuki S.[2], Hiraoka K.[2], Miyake M.[2], Watabe H.[5], Iwata R.[6], Arai H.[4], Kudo Y.[7], Gonda K.[1], Tamura H.[1], and Yanai K.[2,]

[1]*Division of Medical Physics, Tohoku University Graduate School of Medicine*
[2]*Division of Cyclotron Nuclear Medicine, Cyclotron Radioisotope Center, Tohoku University*
[3]*Department of Pharmacology, Tohoku University School of Medicine*
[4]*Division of Geriatrics and Gerontology, Institute of Development, Aging and Cancer, Tohoku University*
[5]*Division of Radiation Protection and Safety Control, Cyclotron Radioisotope Center, Tohoku University*
[6]*Division of Radiopharmaceutical Chemistry, Cyclotron Radioisotope Center, Tohoku University*
[7]*Innovation of New Biomedical Engineering Center, Tohoku University*

Introduction

In vivo amyloid imaging using positron emission tomography (PET), which provides quantitation and visualisation of amyloid β (Aβ) deposition in brain, is useful for earlier diagnosis of Alzheimer's disease (AD). Therefore, several Aβ binding probes dedicated for PET imaging have been developed [1, 2]. Most of these PET Aβ ligands are ^{11}C labelled compounds (physical half life [$T_{1/2}$], 20 min), and ^{18}F labelled agents are being increasingly investigated owing to their long half life ($T_{1/2}$, 109.7 min). The long $T_{1/2}$ of ^{18}F enables several PET scans to be carried out from a single-synthesis of labelled agent and also enables its commercial distribution to any PET facility. On the other hand, the longer the $T_{1/2}$ of the radioisotope gets, the greater the radiation dose exposure for the PET subject for the same administered dose of radioligand.

For subjects undergoing PET, internal radiation exposure is inevitable and the radiation dose delivered is proportional to the level of radioactivity of the injected radioligand, and the number of injections. In the case of amyloid imaging, subjects often have multiple PET scans for diagnostic or therapeutic longitudinal monitoring of Aβ aggregation in the brain. Therefore, estimation of the radiation dose exposure from each PET radioligand, and the use of well-balanced PET scan protocols taking into consideration subject risk and benefit, are important.

Fluorinated amyloid imaging compound ([^{18}F]FACT) is an ^{18}F-labelled amyloid imaging agent developed at Tohoku University [3]. In the present study, the radiation dosimetry and biodistribution of [^{18}F]FACT was investigated in healthy elderly subjects, who are the target group for PET amyloid imaging.

Materials and Methods

PET studies were performed in three healthy male and in three healthy female volunteers (mean age±SD, 76.3±3.2 years) (Table 1**)**. All subjects were Japanese, and were free of somatic and neuropsychiatric illness, as determined by clinical history and physical examination. This study was approved by the Ethics Committee on Clinical Investigations of Tohoku University School of Medicine, and was performed in accordance with the Declaration of Helsinki. Written informed consent was obtained from all subjects after a complete description of the study had been made.

All whole body PET studies were performed using a SET-2400W scanner (Shimadzu Inc., Kyoto, Japan) in two-dimensional mode[4]. Four emission scans and two transmission scans (before administration and intermediate emission scans) using a ^{68}Ge/^{68}Ga source were performed. At 2 min after intravenous administration of 142–180 MBq [^{18}F]FACT, a series of whole body PET scans were performed. The schedule for the first and second transmission scans, and the first, second third and fourth emission scans were: 6 positions × 4 min; 6 positions × 4 min; 6 positions × 3 min; 6 positions × 3 min; 6 positions × 3 min; and 6 positions × 4 min, respectively. All emission data were reconstructed using OS-EM with iteration 16 and subset 2, after attenuation correction. Scatter correction was not performed because of the use of 2D-mode data acquisition. All individual PET images and MRI images were co-registered to the first individual PET images using a rigid matching module of PMOD version 3.1 (PMOD Technologies, Zurich, Switzerland). Urination was controlled before, after and during the series of PET studies. The volume and radioactivity levels of their urine samples were measured using a calibrated well counter.

The Medical Internal Radiation Dose (MIRD) committee of the Society of Nuclear Medicine developed the algorithm to calculate absorbed dose *D* (Gy) in organs. The mean absorbed dose to the *k*-th target organ is defined as follows:

$$\overline{D}(r_k) = \sum_h \tilde{A}_h \cdot S(r_k \leftarrow r_h) = \sum_h A_0 \cdot \tau_h \cdot S(r_k \leftarrow r_h)$$

$$\tau_h = \frac{\tilde{A}_h}{A_0}$$

(1)

where $S(r_k \leftarrow r_h)$ is the absorbed dose in the k-th target organ per unit of accumulated activity in the h-th source organ, called the S-value. $\tilde{A}_h$ is the number of disintegrations in the h-th source organ, A_0 is the injected dose, and τ_h is the number of disintegrations per unit activity administered in the h-th source organ. The effective dose E (Sv), as defined by International Commission on Radiological Protection (ICRP) 60 [5] was obtained using the following equation:

$$E = \sum_i Q \cdot w_i \cdot D_i \tag{2}$$

where D_i is the absorbed dose of the i-th target organ, w_i is the weighting risk factor in the i-th target organ and Q is the quality factor (Q = 1 for β and γ-rays).

In the present study, τ_h in Eq. (1) was derived from PET measurements and the organ volumes of the reference male or females. Averaged time-activity curves for each organ were obtained using the ROI values from each subjects' PET images. The number of source organs used for ROI drawing was 19 for male and 20 for female subjects (adrenal, brain, breast, gallbladder content, lower large intestine (LI) content, small intestine content, stomach content, upper LI content, heart content, heart wall, kidney, liver, lung, muscle, pancreas, red marrow, spleen, testis, thyroid and uterus). Two nuclear medicine physicians manually drew the ROIs using PMOD on co-registered MRI images. Individual non-decay corrected time-activity curves C(t) [Bq/ml] per injected dose A_0 [Bq] was extrapolated into the %ID of the reference subject as follows:

$$\%ID(t)_{\text{reference}} = \left(\frac{C(t)}{A_0} \right)_{\text{individual}} \times V_{\text{reference}} \tag{3}$$

where V [ml] is organ volume and $V_{\text{reference}}$ is V of the reference subject (we used a 70-kg adult male and 58-kg adult female as the male and female reference subjects) [6, 7]. The time-integrated activity coefficient τ [Bq-h/Bq] in Eq. (1) was obtained by fitting (%ID(t)) using a mono-exponential function and integrating from time zero to infinity. If the time-activity curve did not convergence at the last PET scan (e.g. intestines and gallbladder), time-activity curves were fitted using two exponential functions, and then the area under the curve after the acquisition of the last image was calculated by assuming only physical decay of F-18 and no additional biologic clearance to be conservative [5]. The time-integrated activity coefficient for urinary bladder content was calculated by applying the dynamic

urinary bladder model [5] to the urine samples with a bladder voiding interval of 2 h. All fitting procedures were undertaken using a mean fit of R^2 of 0.93±0.13. Finally the time-integrated activity coefficient τ [Bq-h/Bq] was used for calculation of the absorbed dose, *D*, in Eq. (1) and the effective dose, *E*, in Eq. (2). Both kinetics calculations (fitting and integration) and dose estimation were performed using OLINDA/EXM software version 1.0 (Department of Radiology and Radiological Sciences Vanderbilt University, Nashville, TN, USA)[7].

Results and Discussion

Figure 1 is the maximum intensity projection PET image for a single female subject (No. 5) and demonstrates the typical biodistribution of [^{18}F]FACT in the human body. The highest accumulations of this radioligand were observed in the gallbladder, liver, intestine and urinary bladder. The biodistribution pattern of [^{18}F]FACT in human subjects showed a predominant hepatobiliary excretion, which is similar to what has been observed for other amyloid ligands, such as [^{11}C]PIB, ^{18}F-AV-45, ^{18}F-GE067 and ^{18}F-BAY94-9172[5,8-10]. Figure 2 shows the decay-uncorrected time-activity curve of the %ID for typical source organs from the six volunteers. F-18 uptake in the intestines (Fig. 2C) indicated larger individual variations in radioactivity uptake relative to other organs (e.g. the Liver in Fig. 2A). Radioactivity uptake in the upper large intestine showed propagation of both ligand kinetics and inter-subject variation from the gallbladder (Fig. 2D).

The [^{18}F]FACT absorbed doses are shown in Table 2. High absorbed dose in humans was observed in the gallbladder (333±251 μGy/MBq). The effective dose estimated from the human PET study was 18.6±3.74 μSv/MBq. The effective doses of other ^{18}F-labelled PET amyloid radioligands were: ^{18}F-AV-45, 13 μSv/MBq and 19.3 μSv/MBq[8,11]; ^{18}F-GE067, 33.8 μSv/MBq[5]; and ^{18}F-BAY94-9172, 14.67 μSv/MBq[9].

In the present study, the averaged injected activity of 160.8 MBq corresponded to a radiation dose of 2.99 mSv per single administration. ICRP 62 [13] recommended that the maximum radiation dose that causes a “minor to intermediate” increase of risk levels, while preserving social benefit levels that are “intermediate to moderate”, has an effective limit of 10 mSv per year[13,14]. Thus, the maximum injectable activity is 537.6 MBq [^{18}F]FACT per year, and this injection dose limit allows two or three PET scans to be performed. Furthermore, amyloid imaging is mainly undertaken in elderly patients aged > 50 years, even though for early detection of AD, patients aged < 50 years will also have an amyloid

PET scan. According to the guidance on medical exposures in medical and biomedical research by the European Commission [15], dose restrictions for patients aged over > 50 years are not as strict as for younger patients. Therefore, considerably more multiple PET scans may be possible.

Conclusion

The effective dose of the F-18 labelled amyloid imaging agent, [^{18}F]FACT, was found to be acceptable for clinical study.

References

1) Furumoto S, Okamura N, et al., *Curr Top Med Chem*. **7** (2007) 1773.
2) Kudo Y, Okamura N, et al., *J Nucl Med*. **48** (2007) 553.
3) Furumoto S, Okamura N, et al., *Mol Img Biol.* **15** (2013) 497.
4) Fujiwara T, Watanuki S, et al., *Ann Nucl Med.* 1997 Nov;11(4):307-13.
5) Koole M, Lewis DM, et al., *J Nucl Med.* **50** (2009) 818.
6) Cristy M, Eckerman KF., *ORNL/TM.* (1987) 8381.
7) Stabin MG, Sparks RB, et al., *J Nucl Med.* **46** (2005) 1023.
8) Lin KJ, Hsu WC, et al., *Nucl Med Biol.* **37** (2010) 497.
9) O'Keefe GJ, Saunder TH, et al., *J Nucl Med*. **50** (2009) 309.
10) Scheinin NM, Tolvanen TK, et al., *J Nucl Med.* **48** (2007) 128.
11) Wong DF, Rosenberg PB, et al., *J Nucl Med*. **51** (2010) 913.
12) Lartizien C, Comtat C, et al., *J Nucl Med.* **43** (2002) 1268.
13) ICRP. Radiological Protection in Biomedical Research. Oxford, UK: Pergamon Press; 1992.
14) Kimura Y, Simeon FG, et al., *Eur J Nucl Med Mol Imaging*. **37** (2010) 1943.
15) Directorate-General Environment NSaCP. Radiation protection. 1998:1-14.

Table 1. Information regarding the human subjects.

Subject No.	Sex	Age [years]	Height [m]	Weight [kg]	BMI [kg/m^2]
1	M	77	1.59	61.2	24.2
2	M	78	1.62	65	24.8
3	M	77	1.75	74	24.2
4	F	70	1.46	39	18.3
5	F	77	1.56	60.2	26.1
6	F	79	1.55	56	23.3
Mean ± 1SD		76.3 ± 3.2	1.58 ± 0.75	59.2 ± 11.6	23.5 ± 2.7

Table 2. Averaged absorbed dose estimates [μGy/MBq] for the target organs from the whole-body PET data (n = 6) from experiments involving human subjects of [^{18}F]FACT.

Organ	All subject (n = 6)		
Adrenal	1.96.E+01	±	2.00.E+00
Brain	9.91.E+00	±	1.82.E+00
Breasts	8.69.E+00	±	2.55.E+00
Gallbladder wall	3.33.E+02	±	2.51.E+02
Lower large intestine wall	2.52.E+01	±	1.26.E+01
Small intestine	3.36.E+01	±	3.07.E+01
Stomach wall	1.61.E+01	±	3.44.E+00
Upper large intestine wall	2.98.E+01	±	1.50.E+01
Heart wall	1.62.E+01	±	1.70.E+00
Kidneys	2.01.E+01	±	4.30.E+00
Liver	7.75.E+01	±	1.45.E+01
Lungs	1.46.E+01	±	1.10.E+00
Muscle	1.03.E+01	±	1.27.E+00
Ovary	1.67.E+01	±	6.65.E+00
Pancreas	2.32.E+01	±	3.11.E+00
Red Marrow	1.31.E+01	±	1.70.E+00
Osteogenic Cells	1.60.E+01	±	3.65.E+00
Skin	7.30.E+00	±	1.39.E+00
Spleen	1.37.E+01	±	2.48.E+00
Testis	7.32.E+00	±	2.16.E+00
Tymus	1.00.E+01	±	1.85.E+00
Tyroid	8.36.E+00	±	1.38.E+00
Urinary bladder wall	2.23.E+01	±	7.33.E+00
Uterus	1.67.E+01	±	8.13.E+00
Total body	1.38.E+01	±	1.63.E+00
Effective Dose [μSv/MBq]	1.86.E+01	±	3.74.E+00

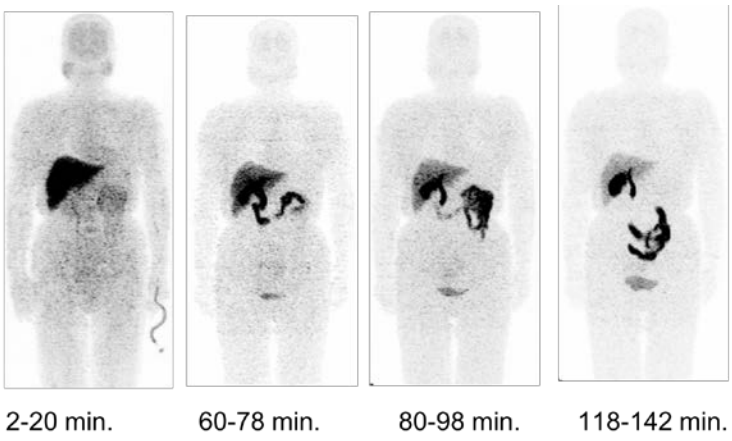

Figure 1. Example of Maximum intensity projection images.

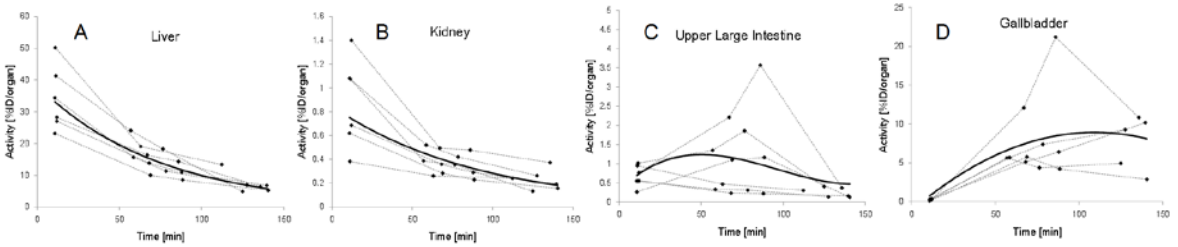

Figure 2. Typical time-activity curves (decay-uncorrected) for (A) liver, (B) kidney, (C) upper large intestine of the six subjects and (D) gallbladder contents. The thin line represents the six individual subjects, and the bold line is fitted using the data sets for the six subjects.

VIII. 2. Amyloid PET Imaging in Idiopathic Normal-Pressure Hydrocephalus

Hiraoka K.[1], Narita W.[2], Kikuchi H.[2], Baba T.[2], Kanno S.[2], Iizuka O.[2], Tashiro M.[1], Furumoto S.[3,5], Okamura N.[3], Furukawa K.[4], Arai H.[4], Iwata R.[5], Mori E.[2], and Yanai K.[3]

[1]*Division of Cyclotron Nuclear Medicine, Cyclotron and Radioisotope Center, Tohoku University*
[2]*Department of Behavioral Neurology and Cognitive Neuroscience, Tohoku University Graduate School of Medicine*
[3]*Department of Pharmacology, Tohoku University Graduate School of Medicine*
[4]*Department of Geriatrics and Gerontology, Institute of Development, Aging and Cancer, Tohoku University*
[5]*Division of Radiopharmaceutical Chemistry, Cyclotron and Radioisotope Center, Tohoku University*

Backgrounds

22.2 to 67.6% of idiopathic normal-pressure hydrocephalus (iNPH) subjects showed Alzheimer pathology such as senile plaques in the studies using frontal lobe cortical biopsy during shunt surgery or intracranial pressure monitoring[1, 2]. In cases of diagnosing iNPH, comorbidity of or differential diagnosis from Alzheimer's disease (AD) are sometimes problems.

Objective

To detect amyloid deposits in the brain before shunt surgery.

Methods

Amyloid imaging using positron emission tomography (PET) and a radiolabeled pharmaceutical comound, ^{11}C-BF227-PET[3] (Fig. 1) was performed in 5 probale iNPH patients (age 79.0±4.3) before shunt surgery. The mean standard uptake value of neocortical regions including frontal, temporal and parietal lobes and posterior cingulate gyrus was measured. Using cerebellar hemispheres as reference regions, the mean standard uptake value ratio (SUVR) of neocortices were estimated, which was regarded as index of amyloid deposits in the neocortices. The results were compared with SUVRs of 10 normal elderly subjects (age 70±2.8) and 10 AD patients (age 69.9±5.9) who underwent ^{11}C-BF227-PET

imaging previously.

Results

The SUVR of iNPH patients, normal elderly subjects, and AD patients were 1.21±0.08, 1.12±0.08, 1.27±0.05, respectively. The 3 iNPH cases showed relatively low SUVR, while the SUVRs of the 2 iNPH cases were as high as those of AD cases (Fig 2.).

Conclusions

There are amyloid-positive and amyloid-negative iNPH cases. We are planning to investigate the association between brain amyloid burden and clinical improvement following shunt surgery.

References

1) Bech RA, Waldemar G, Gjerris F, Klinken L, Juhler M. *Acta Neurochir.*, **141** (1999) 633.
2) Hamilton R, Patel S, Lee EB, et al. *Annal. Neurol.*, **68** (2010) 535.
3) Kudo Y, Okamura N, Furumoto S, et al. *J. Nucl. Med.*, **48** (2007) 553.

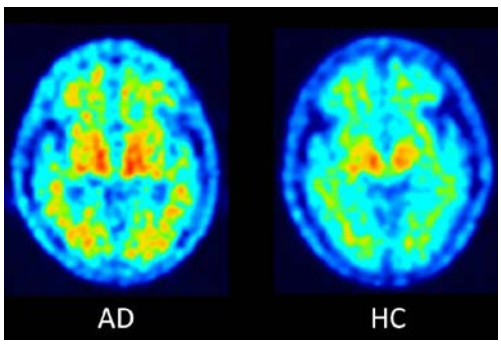

Figure 1. ^{11}C-BF227-PET images of a patient with Alzheimer's disease (AD) and a healthy control subject (HC).

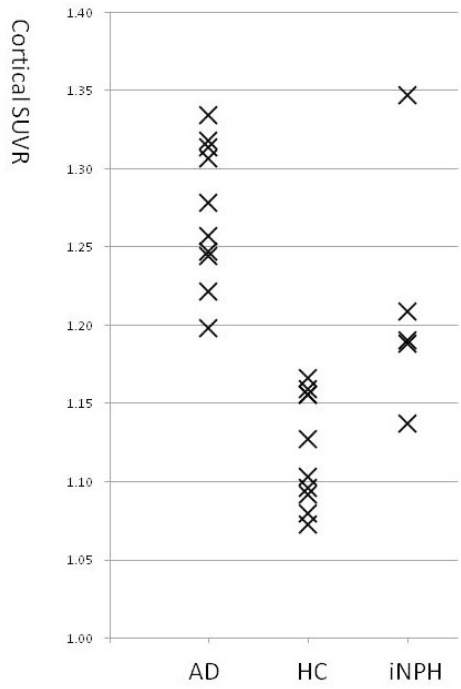

Figure 2. Cortical SUVR of each subject. AD= Alzheimer's disease; HC:=healthy control; iNPH=idiopathic normal-pressure hydrocephalus.

VIII. 3. Investigation of Renal Medullary Blood Flow Imaging in Human

Ohsaki Y.[1], Mori T.[1], Koizumi K.[1], Shidahara M.[1], Yagi A.[1], Tashiro M.[2], Iwata R.[2], Oba I.[1], Furushou M.[1], Makiko C.[1], Tanno M.[1], Hiraoka K.[2], Watanuki S.[2], Ishikawa Y.[2], Miyake M.[2], and Ito S.[1]

[1]Graduate School of Medicine, Tohoku University,
[2]Cyclotron And Radioisotope Center, Tohoku University

Introduction

Kidney plays important roles in regulation of body fluid and maintenance of electrolytes balance. Although kidney receives as much as 20% of cardiac output, renal blood flow (RBF) is mostly distributed to cortical region, and renal medullary region receives less than 10% of total RBF. However, thick ascending limb of loop of Henle (TAL) reabsorbs 25-30% of filtered sodium using active transport which consumes large amount of oxygen in renal medullary region. Therefore renal medullary region is vulnerable to hypoxia and thereby easily injured [1)]. Renal injury starts at corticomedullary border region in high blood pressure animal model [2,3)]. Renal medullary blood flow (MBF) is supplied by vasa recta which are downstream of juxtamedullary efferent artery; therefore juxtamedullary glomerulus injury could reduce MBF. Since change in MBF affects pressure natriuresis, reduction of MBF could cause result in the increase of body fluid and blood pressure [4)]. However, most of clinical renal function tests, including GFR and urinary albumin excretion, evaluate renal function mostly in the cortical area, and there is few established clinically available method for the diagnosis of renal medullary function.

Molecular imaging is one of the possible methods for diagnosis of renal medullary function. Our study, as cited by previous review, have demonstrated that renal medullary oxygen level was increased after 1 L water load in a healthy volunteer who was restricted water intake for 8 h using blood oxygenation level dependent magnetic resonance imaging (BOLD-MRI) 5. In this study, we tried to enhance the method for evaluation of renal medullary function using positron emission tomography (PET) with $[^{15}O]H_2O$.

Methods

Abdominal area of a healthy volunteer and three end stage renal disease (ESRD) patient on peritoneal dialysis therapy under water intake restriction condition were scanned by SET-2400W with $[^{15}O]H_2O$. Abdominal area of subjects was scanned again at 30 min after 1 L of water was loaded. Local blood flow in the kidney of subjects was evaluated by scanned image.

Results

PET image of healthy volunteer and representative PET image of ESRD patient is shown in Figs. 1 and 2, respectively. The intensity of $[^{15}O]H_2O$ signal in renal region of subjects before and after water ingestion is shown in Table 1. $[^{15}O]H_2O$ intensity of the renal area in the image obtained after water ingestion tend to increase compared to the image of water restricted condition in healthy volunteer. Compared to healthy volunteer, the intensity in the kidney of ESRD patients tend to be lower and did not increase by water ingestion.

Discussion

As consistent to our previous study [5], water intake tends to increase renal regional blood flow in health volunteer. Renal local blood flow tends to be decreased in ESRD patient compared to healthy volunteer in both dehydrated and hydrated condition, consistent with Alpert's report [6]. These results indicate that increase in renal flow by water intake is altered in ESRD which could results in the enhanced volume overload. Since we did not evaluate the region and mechanism involved in this observation, further study is required by measuring renal regional blood flow and response to drugs that could affect renal blood flow.

Acknowledgements

This study was partly supported by Grant-in-Aid for Challenging Exploratory Research 25670405. Authors appreciate all CYRIC staff for their professional support to our research.

References

1) Cowley AW Jr., *Physiol Rev.* **72** (1992) 231.
2) Mori T, Cowley AW Jr., *Hypertension* **43** (2004) 752.

3) Nagasawa T, Mori T, Ohsaki Y, Yoneki Y, Guo Q, Sato E, Oba I, Ito S., *Hypertens Res.* **35** (2012) 1024.
4) Mori T, Cowley AW Jr, Ito S., *J. Pharmacol. Sci.* **100** (2006) 2.
5) Miyata T, Kikuchi K, Kiyomoto H, van Ypersele de Strihou C., *Nat. Rev. Nephrol.* **7** (2011) 469.
6) Alpert NM, Rabito CA, Correia DJ, Babich JW, Littman BH, Tompkins RG, Rubin NT, Rubin RH, Fischman AJ., *J. Nucl. Med.* **43** (2002) 470.

Table 1. Regional blood flow in the kidney before and after water ingestion.

Subject No.	Subject type	Kidney side	Before	After
1	Healthy	Right	419	643
		Left	338	519
2	Patient	Right	110	101
		Left	88	96
3	Patient	Right	146	150
		Left	138	143
4	Patient	Right	164	124
		Left	153	132

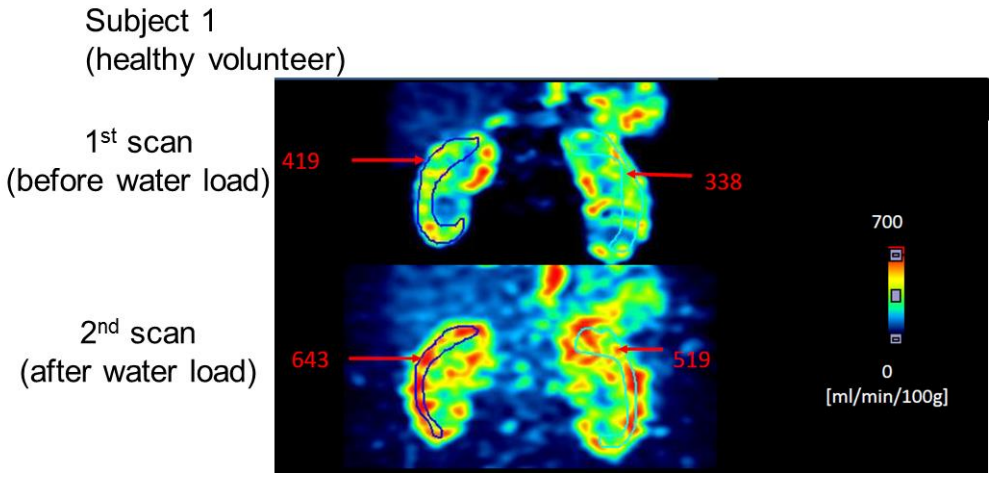

Figure 1. PET image before and after water ingestion in health volunteer.

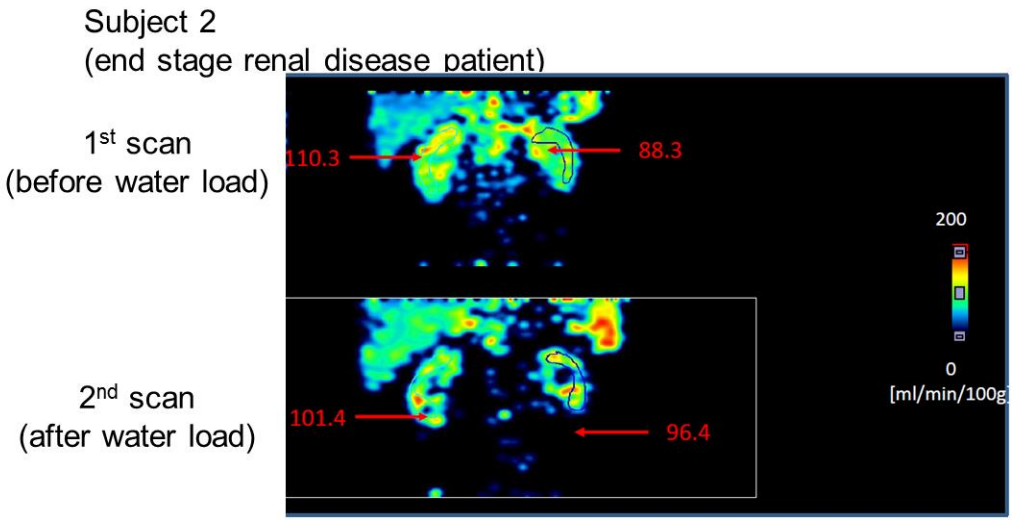

Figure 2. PET image before and after water ingestion in end stage renal patient.

IX. RADIATION PROTECTION AND TRAINING OF SAFETY HANDLING

IX. 1. Beginners Training for Safe Handling of Radiation and Radioisotopes at Tohoku University

Watabe, H., Ohtomo K., Mayama F., Tojo I., and Yuki H.

Cyclotron and Radioisotope Center, Tohoku University

This report summarizes the beginners training for safe handling of radiation and radioisotopes at Tohoku University from 2012 to 2013. Twice a year (in May and in November), we organize three educational courses including lectures and practices, namely 1) Radiation and Isotopes, 2) X-ray Machines and Electron Microscope, and 3) Synchrotron Radiation (SOR). Since November 2002, we have also organized lectures in English for students or researchers who are not familiar with Japanese language. The training was held twice a year, in May and November under the help for lectures and practice from various departments and research institutes of the university.

The training for "Radiation and Radioisotopes" is for persons who use unshielded radioisotopes and accelerators, and has been conducted from 1977. The contents of lectures and practices are shown in Table 1. The departments or institutes to which trainees belong and the distributions of trainees are shown in Table 2 and Table 3.

The training for "X-ray machines and electron microscopes" started at the end of 1983. The training is scheduled at the same time as that for "Radiation and Radioisotopes". In this course, only lectures are given with no practice. The contents of lectures are shown in Table 4. The departments or institutes to which trainees belong and the distributions of trainees are shown in Table 5 and Table 6.

The training for "Synchrotron Radiation" began at the end of 1995. The contents of the lectures are the same as those of the "Radiation and Radioisotopes" but no practice. The departments or institutes to which trainees belong and the distributions of trainees are shown in Table 7 and Table 8.

Table 1. Contents of the lectures and practices for "Radiation and Radioisotopes" in 2012 and 2013.

Lectures (one day)	Hours
Introduction to radiation	0.5
Effects of radiation on human	1.0
Radiation physics and measurements	1.0
Chemistry of radioisotopes	1.0
Radiological protection ordinance including video	1.5
Safe handling of radioisotopes	1.5

Practices (one day)	Hours
Treatment of unsealed radioactive solution	4.0
Measurement of surface contamination and decontamination	1.0
Measurement of gamma-rays and beta-rays	2.0

Table 2. Distribution of trainees for “Radiation and Radioisotopes” in 2012.

Department	Staff	Student	Total	English class
CYRIC	0	4	4	0
Medicine	21	55	76	4
Dentistry	0	12	12	1
Pharmacy	1	48	49	0
Science	6	61	67	4
Engineering	11	108	119	9
Agriculture	3	55	58	0
Research Institutes	24	51	75	7
The others	0	0	0	0
Total	66	394	460	25

Table 3. Distribution of trainees for “Radiation and Radioisotopes” in 2013.

Department	Staff	Student	Total	English class
CYRIC	0	8	8	0
Medicine	15	58	73	0
Dentistry	2	6	8	0
Pharmacy	1	54	55	1
Science	11	84	95	0
Engineering	5	117	122	5
Agriculture	1	48	49	0
Research Institutes	16	49	65	13
The others	0	0	0	0
Total	51	424	475	21

Table 4. Contents of the lectures for “X-ray machines and Electron microscopes” in 2012 and 2013.

Lectures (one day)	Hours
Safe handling of X-ray machines	1.5
Radiological protection ordinance	0.5
Video for safe handling of radiation and radioisotopes	0.5

Table 5. Distribution of trainees for “X-ray machines and Electron microscopes” in 2012.

Department	Staff	Student	Total	English class
CYRIC	0	0	0	0
Medicine	1	8	9	0
Dentistry	2	4	6	0
Pharmacy	0	5	5	0
Science	4	48	52	2
Engineering	12	176	188	6
Agriculture	0	0	0	0
Research Institutes	20	58	78	14
The others	0	0	0	0
Total	39	299	338	22

Table 6. Distribution of trainees for “X-ray machines and Electron microscopes” in 2013.

Department	Staff	Student	Total	English class
CYRIC	0	0	0	0
Medicine	5	5	10	0
Dentistry	7	14	21	1
Pharmacy	0	1	1	0
Science	2	26	28	4
Engineering	25	189	214	8
Agriculture	0	0	0	0
Research Institutes	29	58	87	26
The others	0	0	0	0
Total	68	293	361	39

Table 7. Distribution of trainees for “Synchrotron radiation” in 2012.

Department	Staff	Student	Total	English class
CYRIC	0	0	0	0
Medicine	0	0	0	0
Dentistry	0	1	1	0
Pharmacy	0	0	0	0
Science	3	23	26	0
Engineering	1	36	37	5
Agriculture	0	0	0	0
Research Institutes	9	22	31	4
The others	0	0	0	0
Total	13	82	95	9

Table 8. Distribution of trainees for “Synchrotron radiation” in 2013.

Department	Staff	Student	Total	English class
CYRIC	0	0	0	0
Medicine	0	0	0	0
Dentistry	0	0	0	0
Pharmacy	0	0	0	0
Science	1	24	25	1
Engineering	7	46	53	8
Agriculture	0	0	0	0
Research Institutes	16	34	50	10
The others	0	0	0	0
Total	24	104	128	19

IX. 2. Radiation Protection and Management

Yuki H.[1], Ohtomo K.[1], Watabe H.[1], and Nakae H.[2]

[1]Cyclotron and Radioisotope Center, Tohoku University
[2]Japan Environment Research Co., Ltd.

1. Overview

In the middle of the fiscal year of 2012, CYRIC was recovered from the damage by the Tohoku Region Pacific Coast Earthquake, and research and education in the center were conducted as active as usual.

2. Unsealed radionuclides used at CYRIC

The species and amounts of the four most used unsealed radionuclides during the fiscal year of 2012 and 2013 are listed in Table 1. The table includes the isotopes produced by the cyclotron as well as those purchased from the Japan Radio Isotope Association or taken over from other radioisotope institutes.

3. Radiation exposure dose of individual worker

The exposure doses of the workers at CYRIC during 2012 and 2013 are given in Table 2. The doses were sufficiently lower than the legal dose limits.

4. Radiation monitoring of the workplace

Radiation dose rates inside and outside of the controlled areas at CYRIC were monitored periodically and occasionally when needed. They were generally below the legal dose limits although there are several “hot spots” in mSv/hr range like slits or beam stopper of the 930 cyclotron and so on. Surface contamination levels of the floors inside the controlled areas were also measured with a smear method and a survey meter method. They were under the legal regulation levels.

5. Wastes management

The radioactive wastes were delivered to the Japan Radioisotope Association in the fiscal year of 2012.

The concentration of radioisotopes in the air released from the stack after filtration was monitored with stack gas monitors. The values of concentration were well below the legal regulation levels. The radioactive water was stocked in the tanks at least for 3 days and then released to the sewerage after confirming that the concentration was lower than the legal regulation levels.

Table 1. The four most used unsealed radioisotopes used at CYRIC during the fiscal year of 2012 and 2013.

	2012	2013
C-11	408.00 GBq	224.14 GBq
O-15	3.5450 GBq	1.6400 GBq
F-18	1.0329 TBq	1.3501 TBq
P-32	1.1470 GBq	1.1470 GBq

Table 2. Occupational radiation exposures in CYRIC during the fiscal year of 2012 and 2013.

Dose range (mSv)	Number of individuals	
	2012	2013
0.0 - 5.0	199	289
5.0 - 10.0	0	0
10.0 - 15.0	0	0
15.0 - 20.0	0	0
20.0 - 25.0	0	0
25.0 - 50.0	0	0
50.0 -	0	0
Total number of persons monitored	199	289

X. PUBLICATIONS

X. PUBLICATIONS

[839] Candidate for the 2+ excited Hoyle state at Ex ~ 10 MeV in ^{12}C.
M. Itoh, H. Akimune, M. Fujiwara, U. Garg, H. Hashimoto, T. Kawabata, K. Kawase, S. Kishi, T. Murakami, K. Nakanishi, Y. Nakatsugawa, B.K. Nayak, S. Okumura, H. Sakaguchi, H. Takeda, S. Terashima, M. Uchida, Y. Yasuda, M. Yosoi, and J. Zenihiro .
Phys. Rev. C, **84** (2012) 054308.

[840] High-resolution study of Gamow-Teller transitions via the ^{54}Fe(^{3}He,t)^{54}Co reaction
T. Adachi, Y. Fujita, A.D. Bacher, G.P.A. Berg, Black, D. De Frenne, C.C. Foster, H. Fujita, K. Fujita, K.Hatanaka, M. Honma, E. Jacobs, J. Janecke, K. Kanzaki, K. Katori, K. Nakanishi, A. Negret, T. Otsuka, L. Popescu, D.A. Roberts, Y. Sakemi, Y. Shimbara, Y. Shimizu, E.J. Stephenson, Y. Tameshige, A. Tamii, M. Uchida, H. Ueno, T. Yamanaka, M. Yosoi, K.O. Zell.
Phys. Rev. C, **85** (2012) 024308.

[841] Pygmy dipole resonance in ^{208}Pb.
I. Poltoratska, P. Neumann-Cosel, A. Tamii, T. Adachi, C.A. Bertulani, J. Carter, M. Dozono, H. Fujita, K. Fujita, Y. Fujita, K. Hatanaka, M. Itoh, T. Kawabata, Y. Kalmykov, A.M. Krumbholz, E. Litvinova, H. Matsubara, K. Nakanishi, R. Neveling, H. Okamura, H.J. Ong, B. Ozel-Tashenov, V.Yu. Ponomarev, A. Richter, B. Rubio, H. Sakaguchi, Y. Sakemi, Y. Sasamoto, Y. Shimbara, Y. Shimizu, F.D. Smit, T. Suzuki, Y. Tameshige, J. Wambach, M. Yosoi, J. Zenihiro.
Phys. Rev. C, **85** (2012) 041304.

[842] Complete sets of polarization transfer observables for the ^{208}Pb($p^{\rightarrow}$,$n^{\rightarrow}$) reaction at 296 MeV and Gamow-Teller and spin-dipole strengths for 208Pb.
T. Wakasa, M. Okamoto, M. Dozono, K. Hatanaka, M. Ichimura, S. Kuroita, Y. Maeda, H. Miyasako, T. Noro, T. Saito, Y. Sakemi, T. Yabe, and K. Yako.
Phys. Rev. C, **85** (2012) 064606.

[843] High-resolution study of Gamow-Teller transitions with the ^{37}Cl(^{3}He-3,*t*)^{37}Ar reaction.
Y. Shimbara, Y. Fujita, T. Adachi, G. P. A. Berg, H. Fujimura, H. Fujita, K. Fujita, K. Hara, K. Y. Hara, K. Hatanaka, J. Kamiya, K. Katori, T. Kawabata, K. Nakanishi, G. Martìnez-Pinedo, N. Sakamoto, Y. Sakemi, Y. Shimizu, Y. Tameshige, M. Uchida, M. Yoshifuku, M. Yosoi.
Phys. Rev. C, **86** (2012) 024312.

[844] Level structure of ^{30}S and its importance in the ^{26}Si(α,p)^{29}P and ^{29}P(p,γ)^{30}S reaction rates.
S. Almaraz-Calderon, W. P. Tan, A. Aprahamian, M. Beard, G. P. A. Berg, B. Bucher, M. Couder, J. Görres, S. O'Brien, D. Patel, A. Roberts, K. Sault, M. Wiescher, C. R. Brune, T.N. Massey, K. Fujita, K. Hatanaka, D. Ishiwaka, H. Matsubara, H. Okamura, H. J. Ong, Y.

Sakemi, Y. Shimizu, T. Suzuki, Y. Tameshige, A. Tamii, J. Zenihiro, T. Kubo, Y. Namiki, Y. Ohkuma, Y. Shimbara, S. Suzuki, R. Watanabe, R. Yamada, T. Adachi, Y. Fujita, H. Fujita, M. Dozono, T. Wakasa.
Phys. Rev. C, **86** (2012) 065805.

[845] Consistent analysis of the 2^+ excitation of the ^{12}C Hoyle state populated in proton and α-particle inelastic scattering.
M. Freer, M. Itoh, T. Kawabata, H. Fujita, H. Akimune, Z. Buthelezi, J. Carter, R.W. Fearick, S.V. Förtsch, M. Fujiwara, U. Garg, N. Hashimoto, K. Kawase, S. Kishi, T. Murakami, K. Nakanishi, Y. Nakatsugawa, B.K. Nayak, R. Neveling, S. Okumura, S.M. Perez, P. Papka, H. Sakaguchi, Y. Sasamoto, F.D. Smit, J.A. Swartz, H. Takeda, S. Terashima, M. Uchida, I. Usman, Y. Yasuda, M. Yosoi, J. Zenihiro.
Phys. Rev. C, **86** (2012) 034320-1-034320-6.

[846] Erosion of N=20 shell in ^{33}Al investigated through the ground-state electric quadrupole moment.
K. Shimada, H. Ueno , G. Neyens, K. Asahi, D.L. Balabanski, J.M. Daugas, M. Depuydt, M. De Rydt, L. Gaudefroy, S. Grevy, Y. Hasama, Y. Ichikawa, D. Kameda, P. Morel, T. Nagatomo, L. Perrot, Ch. Stodel, J.-C. Thomas, Y. Utsuno, W. Vanderheijden, N. Vermeulen, P. Vingerhoets, E. Yagi, K. Yoshida, A. Yoshimi.
Phys. Lett. B, **714** (2012) 246-250.

[847] Giant monopole resonance in even-A Cd isotopes, the asymmetry term in nuclear incompressibility, and the "softness" of Sn and Cd nuclei.
D. Patel, U. Garg, M. Fujiwara, H. Akimune, G.P.A. Berg, M.N. Harakeh, M. Itoh, T. Kawabata, K. Kawase, B.K. Nayak, T. Ohta, H. Ouchi, J. Piekarewicz, M. Uchida, H.P. Yoshida, M.Yosoi.
Phys. Lett. B, **718** (2012),447-450.

[848] A 461 nm Laser System and Hollow-Cathode Lamp Spectroscopy for Magneto-Optical Trapping of Sr Atoms.
T. Aoki, K. Umezawa, Y. Yamanaka, N. Takemura, Y. Sakemi1, Y. Torii.
J. Phys. Soc. Jpn., **81** (2012) 034401.

[849] Search for Alpha Condensed State in ^{24}Mg.
T. Kawabata, T. Adachi, M. Fujiwara, K. Hatanaka, Y. Ishiguro, M. Itoh, Y. Maeda, H. Matsubara, H. Miyasako, Y. Nozawa, T. Saito, S. Sakaguchi, Y. Sasamoto, Y. Shimizu, T. Takahashi, A. Tamii, S. Terashima, H. Tokieda, N. Tomida, T. Uesaka, M. Uchida, Y. Yasuda, N. Yokota, H.P. Yoshida, J. Zenihiro.
Prog. Theoret. Phys. Suppl., **196** (2012) 198-202.

[850] Digital pulse processing for planar TlBr detectors, optimized for ballistic deficit and charge-trapping effect.
M. Nakhostin, K. Hitomi.
Nucl. Instrum. Meth. A. **675** (2012) 47-50.

[851] An early survey of the radioactive contamination of soil due to the Fukushima Daiichi Nuclear Power Plant accident, with emphasis on plutonium analysis.
M. Yamamoto, T. Takada, S. Nagao, T. Koike, K. Shimada, M. Hoshi, K. Zhumadilov, T.

Shima, M. Fukuoka, T. Imanaka, S. Endo, A. Sakaguchi, S. Kimura.
Geochem. J., **46**, (2012) 341-353.

[852] A novel partitioning process for treatment of high level liquid waste using macroporous silica-based adsorbents.
S.-Y. Kim, Y. Xu, T. Ito, Y. Wu, T. Tada, K. Hitomi, E. Kuraoka, K. Ishii.
J. Radioanal. Nucl. Chem., **293** (2012) 13-20.

[853] Equilibrium and kinetic studies of selective adsorption and separation for strontium using $DtBuCH_{18}C_6$ loaded resin.
Y. Wu, S.-Y. Kim, D. Tozawa, T. Ito, K. Hitomi, E. Kuraoka, H. Yamazaki, K. Ishii.
J. Nucl. Sci. Tech., **49** (2012) 320-327.

[854] Characterization of TlBr x Cl 1-x crystals for radiation detectors.
T. Onodera, K. Hitomi, C. Onodera, T. Shoji, K. Mochizuki
IEEE Trans. Nucl. Sci., **59** (2012) 1559-1562.

[855] Development of a simplified separation process of trivalent minor actinides from fission products using novel R-BTP/SiO2-P adsorbents.
S. Usuda, Y. Wei, Y. Xu, Z. Li, R. Liu, S-Y. Kim, Y. Wakui, H. Hayashi, H. Yamazaki.
J. Nucl. Sci. Technol., **49** (2012) 334-342.

[856] Measures against radioactive contamination due to Fukushima First Nuclear Power Plant accident Part I: damage situation of the great east japan earthquake.
K. Ishii, A. Terakawa, S. Matsuyama, A. Haswgawa, K. Nagakubo, T. Sakueada, Y. Kikuchi, M. Fujiwara, H. Yamazaki, H. Yuhki, S.-Y. Kim, I. Satoh.
Int. J. PIXE, **22** (2012) 1-5.

[857] Measures against radioactive contamination due to Fukushima First Nuclear Power Plant Accident Part II: Measurement of space radiation dose rates and examination of contamination in food.
K. Ishii, A. Terakawa, S. Matsuyama, A. Haswgawa, K. Nagakubo, T. Sakueada, Y. Kikuchi, M. Fujiwara, H. Yamazaki, H. Yuhki, S.-Y. Kim, I. Satoh.
Int. J. PIXE, **22** (2012) 7-12.

[858] Measures against radioactive contamination due to Fukushima First Nuclear Power Plant accident Part III: Removing and decontamination of contaminated soil.
K. Ishii, A. Terakawa, S. Matsuyama, A. Haswgawa, K. Nagakubo, T. Sakueada, Y. Kikuchi, M. Fujiwara, H. Yamazaki, H. Yuhki, S.-Y. Kim, I. Satoh.
Int. J. PIXE, **22** (2012) 13-19.

[859] Challenges to develop single-column MA(III) separation from HLLW using R-BTP type adsorbents.
S. Usuda, Y. Wei, R. Liu, Z. Li, Y. Xu, Y. Wu, S.-Y. Kim.
Sci. China Chem., **55** (2012) 1732-1738.

[860] Adsorption and separation behavior of yttrium and strontium in nitric acid solution by extraction chromatography using a macroporous silica-based adsorbent.
Y. Xu, S.-Y. Kim, T. Ito, K. Nakazawa, Y.Funaki, T. Tada, K. Hitomi, K. Ishii.

J. Chromat., A **1263** (2012) 28-33.

[861] Evaluation study on properties of isohexyl-BTP/SiO_2-P resin for direct separation of trivalent minor actinides from HLLW.
R. Liu, Y. Wei, Y. Xu, S. Usuda, S.-Y. Kim, H. Yamazaki, K. Ishii.
J. Radioanal. Nucl. Chem., **292** (2012) 537-544.

[862] Study on selective separation of cesium from high level liquid waste using a macroporous silica-based supramolecular recognition absorbent.
Y. Wu, S.-Y. Kim, D. Tozawa, T. Ito, T. Tada, K. Hitomi, E. Kuraoka, H. Yamazaki, K. Ishii
J. Radioanal. Nucl. Chem., **293** (2012) 13-20.

[863] Electrochemical and Spectroscopic Studies of Pu(IV) and Pu(III) in Nitric Acid Solutions.
S.-Y. Kim, T. Asakura, Y. Morita.
J. Radioanal. Nucl. Chem., **295** (2012) 937-942.

[864] Reactivity of electrochemically concentrated anhydrous [^{18}F]fluoride for microfluidic radiosynthesis of ^{18}F-labeled compounds.
R. Wong, R. Iwata, H. Saiki, S. Furumoto, Y. Ishikawa, E. Ozeki.
Appl. Radiat. Isot., **70** (2012) 193-199.

[865] Synthesis of [^{11}C]interleukin 8 using a cell-free translation system and L-[^{11}C]methionine.
R. Harada, S. Furumoto, T. Yoshikawa, Y. Ishikawa, K. Shibuya, N. Okamura, R. Iwata, K. Yanai.
Nucl. Med. Biol., **39** (2012) 155-160.

[866] Simple preparation and purification of ethanol-free solutions of 3'-deoxy-3'-[^{18}F]fluorothymidine ([^{18}F]FLT) by means of disposable solid-phase extraction cartridges.
C. Pascali1, A. Bogni, L. Fugazza, C. Cucchi, O. Crispu, L. Laera, R. Iwata, G. Maiocchi, F. Crippa, E. Bombardieri.
Nucl. Med. Biol., **39** (2012) 540-550.

[867] Rapid biochemical synthesis of ^{11}C-labeled single chain variable fragment antibody for immuno-PET by cell-free protein synthesis.
T. Matsuda, S. Furumoto, K. Higuchia, J. Yokoyama, M.-R. Zhang, K. Yanai, R. Iwata, T. Kigawa.
Bioorg. Med. Chem., **20** (2012) 6579-6582.

[868] Cardiac positron-emission tomography images with an amyloid-specific tracer in familial transthyretin-related systemic amyloidosis.
K. Furukawa, S. Ikeda, N. Okamura, M. Tashiro, N. Tomita, S. Furumoto, R. Iwata, K. Yanai, Y. Kudo, H. Arai.
Circulation, **125** (2012) 556-557.

[869] Cholinergic deficit and response to donepezil therapy in Parkinson's disease with dimentia.

K. Hiraoka, N. Okamura, Y. Funaki, A. Hayashi, M. Tashiro, K. Hisanaga, T. Fujii, A. Takeda, K. Yanai, R. Iwata, E. Mori.
Eur. Neurol., **68** (2012) 137-143.

[870] Effects of presence of a familiar pet dog on regional cerebral activity in healthy volunteers: a positron emission tomography study.
A. Sugawara, M.M. Masud, A. Yokoyama, W. Mizutani, S. Watanuki, K. Yanai, M. Itoh, M. Tashiro.
Anthrozoos, **25** (2012) 25-34.

[871] [^{11}C]Doxepin binding to histamine H1 receptors in living human brain: reproducibility during attentive waking and circadian rhythm.
K. Shibuya, Y. Funaki, K. Hiraoka, T. Yoshikawa, F. Naganuma, M. Miyake, S. Watanuki, H. Sato, M. Tashiro, K. Yanai.
Front. Syst. Neurosci., **6** (2012) 45.

[872] Photoionization loss in simultaneous magneto-optical trapping of Rb and Sr.
T. Aoki, Y. Yamanaka, M. Takeuchi, Y. Torii, Y. Sakemi.
Phys. Rev. A, **87** (2013) 063426.

[873] Shallow and diffuse spin-orbit potential for proton elastic scattering from neutron-rich helium isotopes at 71 MeV/nucleon.
S. Sakaguchi, T. Uesaka, N. Aoi, Y. Ichikawa, K. Itoh, M. Itoh, T. Kawabata, T. Kawahara, Y. Kondo, H. Kuboki, T. Nakamura, T. Nakao, Y. Nakayama, H. Sakai, Y. Sasamoto, K. Sekiguchi, T. Shimamura, Y. Shimizu, and T. Wakui.
Phys. Rev. C, **87** (2013) 021601(R).

[874] Search for permanent EDM using laser cooled Fr atoms.
H. Kawamura, T. Aoki, H. Arikawa, S. Ezure, T. Furukawa, K. Harada, A. Hatakeyama, K. Hatanaka, T. Hayamizu, K. Imai, T. Inoue, T. Ishikawa, M. Itoh, T. Kato, T. Murakami, H. S. Nataraj, T. Sato, Y. Shimizu, T. Wakasa, H. P. Yoshida, Y. Sakemi.
Hyperfine Interact., **214** (2013) 133-139.

[875] Development of a gas cell-based laser ion source for RIKEN PALIS.
T. Sonoda, M. Wada, H. Tomita, C. Sakamoto, T. Takatsuka, T. Noto, H. Iimura, Y. Matsuo, T. Kubo, T. Shinozuka, T. Wakui, H. Mita, S. Naimi, T. Furukawa, Y. Itou, P. Schury, H. Miyatake, S. Jeong, H. Ishiyama, Y. Watanabe, Y. Hirayama.
Hyperfine Interact., **216** (2013) 103-107.

[876] Extraction of anti-analog giant dipole resonance and neutron skin thickness for ^{208}Pb.
J. Yasuda, T. Wakasa, M. Okamoto, M. Dozono, K. Hatanaka, M. Ichimura, S. Kuroita, Y. Maeda, T. Noro, Y. Sakemi, M. Sasano, K. Yako.
Prog. Theor. Exp.Phys., (2013) 063D02.

[877] Development of a resonant laser ionization gas cell for high- energy, short-lived nuclei.
T. Sonoda, M. Wada, H. Tomita, C. Sakamoto, T. Takatsuka, T. Furukawa, H. Iimura, Y. Itoh, Y. Matsuo, H. Mita, S. Naimi, S. Nakamura, T. Noto, P. Schury, T. Shinozuka, T.

Wakui, H. Miyatake, S. Jeong, H. Ishiyama, Y. X. Watanabe, Y. Hirayama, K. Okada, and A. Takamine
Nucl. Instrum. Methods B, **295** (2013) 1.

[878] Adsorption behavior of platinum group metals in simulated high level liquid waste using macroporous (MOTDGA-TOA)/SiO_2-P silica-based absorbent.
T. Ito, S.-Y. Kim, Y. Xu, K. Hitomi, K. Ishii, R. Nagaishi, T. Kimura.
Separat. Sci. Tech., **48** (2013) 2616-2625.

[879] A novel partitioning process for treatment of high level liquid waste using macroporous silica-based adsorbents.
S.-Y. Kim, Y. Xu, T. Ito, Y. Wu, T. Tada, K. Hitomi, E. Kuraoka, K. Ishii.
J. Radioanal. Nucl. Chem., **295** (2013) 1043-1050.

[880] Separation and recovery of Cm from Cm-Pu mixed oxide samples containing Am impurity.
H. Hayashi, H. Hagiya, S.-Y. Kim, Y. Morita, M. Akabori, K. Minato.
J. Radioanal. Nucl. Chem., **296** (2013) 1275-1286.

[881] Adsorption properties and behavior of the platinum group metals onto a silica-based (Crea+TOA)/SiO_2-P adsorbent from simulated high level Liquid waste of PUREX reprocessing.
Y. Xu, S.-Y. Kim, T. Ito, T. Tada, K. Hitomi, K. Ishii.
J. Radioanal. Nucl. Chem., **297** (2013) 41-48.

[882] Adsorption and desorption behavior of tetravalent zirconium onto a silica-based macroporous TODGA adsorbent in HNO_3 solution.
Y. Xu, S.-Y. Kim, S. Usuda, Y. Wei, K. Ishii.
J. Radioanal. Nucl. Chem., **297** (2013) 91-96.

[883] Application of ^{28}Mg for characterization of Mg uptake in rice seedling under different pH conditions.
N.I. Kobayashi, N. Iwata, T. Saito, H. Suzuki, R. Iwata, K. Tanoi, T.M. Nakanishi.
J. Radioanal. Nucl. Chem., **296** (2013) 531-534.

[884] Application of ^{28}Mg to the kinetic study of Mg uptake by rice plants.
K. Tanoi, N.I. Kobayashi, T. Saito, N. Iwata, A. Hirose, Y. Ohmae, R. Iwata, H. Suzuki, T.M. Nakanishi.
J. Radioanal. Nucl. Chem., **296** (2013) 749-751.

[885] Leaf senescence in rice due to magnesium deficiency-mediated defect in transpiration rate before sugar accumulation and chlorosis.
N.I. Kobayashi, T. Saito, N. Iwata, Y. Ohmae, R. Iwata, K. Tanoi, T.M. Nakanishi.
Physiol. Plantarum, **148** (2013) 490-501.

[886] Different magnesium uptake and transport activity along the rice root axis revealed by ^{28}Mg tracer experiments.
N.I. Kobayashi, N. Iwata, T. Saito, H. Suzuki, a R. Iwata, M. Tanoi, T.M. Nakanishi.
Soil Sci. plant Nutr., **59** (2013) 149-155.

[887] Expression and functional analysis of the CorA-MRS2-ALR-type magnesium transporter family in rice.
T. Saito, N.I. Kobayashi, K. Tanoi, N. Iwata, H. Suzuki, R. Iwata, T.M. Nakanishi.
Plant and Cell Physiol., **54**, (2013) 1673-1683.

[888] Comparison of the binding characteristics of [^{18}F]THK-523 and other amyloid imaging tracers to Alzheimer's disease pathology.
R. Harada, N. Okamura, S. Furumoto, T. Tago, M. Maruyama, M. Higuchi, T. Yoshikawa, H. Arai, R. Iwata, Y. Kudo, K. Yanai.
Eur. J. Nucl. Med. Mol. Imag., **40** (2013) 125-132.

[889] Brain accumulation of amyloid β protein visualized by positron emission tomography and BF-227 in Alzheimer's disease patients with or without diabetes mellitus.
N. Tomita, K. Furukawa, N. Okamura, M. Tashiro, K. Une, S. Furumoto, R. Iwata, K. Yanai, Y. Kudo, H. Arai.
Geriatr. Gerontol. Int., **13** (2013) 215-221.

[890] Evaluation of the biodistribution and radiation dosimetry of the ^{18}F-labelled amyloid imaging probe [^{18}F]FACT in humans.
M. Shidahara, M. Tashiro, N. Okamura, S. Furumoto, K. Furukawa, S. Watanuki, K. Hiraoka, M. Miyake, R. Iwata, H. Tamura, H. Arai, Y. Kudo, K. Yanai.
Eur. J. Nucl. Med. Mol. Imag. Res., **3** (2013) 32.

[891] Novel ^{18}F-labeled arylquinoline derivatives for non-invasive imaging of tau pathology in Alzheimer's disease.
N. Okamura, S. Furumoto, R. Harada, T. Tago, T. Yoshikawa, M. Fodero-Tavoletti, R.S. Mulligan, V.L. Villemagne, H. Akatsu, T. Yamamoto, H. Arai, R. Iwata, K. Yanai, Y. Kudo.
J. Nucl. Med. Mol. Imag., **54** (2013) 1420-1427.

[892] In-vitro and in-vivo characterization of 2-deoxy-2-[^{18}F]fluoro-D-mannose as a tumor-imaging agent for positron emission tomography.
S. Furumoto, R. Shinbo, R. Iwata, Y. Ishikawa, K. Yanai, T. Yoshioka, H. Fukuda.
J. Nucl. Med. Mol. Imag., **54** (2013) 1354-1361.

[893] A ^{18}F-Labeled BF-227 derivative as a potential radioligand for imaging dense amyloid plaques by positron emission tomography.
S. Furumoto., N. Okamura, K. Furukawa, M. Tashiro, Y. Ishikawa, K. Sugi, N. Tomita, M. Waragai, R. Harada, T. Tago, R. Iwata, K. Yanai, H. Arai, Y. Kudo.
Mol. Imaging Biol., **15** (2013) 497-506.

[894] Histamine H1 receptor occupancy by the new-generation antidepressants fluvoxamine and mirtazapine: a positron emission tomography study in healthy volunteers.
H. Sato, C. Ito, M. Tashiro, K. Hiraoka, K. Shibuya, Y. Funaki, R. Iwata, H. Matsuoka, K. Yanai.
Psychopharmacol., **230** (2013) 227-234.

[895] Differences in muscle activities during shoulder elevation in patients with symptomatic and asymptomatic rotator cuff tears: analysis using positron emission

tomography.
N. Shinozaki, H. Sano, R. Omi, K.N. Kishimoto, N. Yamamoto, M. Tashiro, E. Itoi.
J. Shoulder and Elbow Surgery, **23** (2013) e61-e67.

[896] Kinetics of neurodegeneration based on a risk-related biomarker in animal model of glaucoma.
Hayashi T., Shimazawa M., Watabe H., Ose T., Inokuchi Y., Ito Y., Yamanaka H., Urayama S., Watanabe Y., Hara H., Onoe H.
Mol. Neurodegener., **8** (2013) 4.

[897] Optimization of [^{11}C]methionine PET study: appropriate scan timing and effect of plasma amino acid concentrations on the SUV.
Isohashi K., Shimosegawa E., Kato H., Kanai Y., Naka S., Fujino K., Watabe H., Hatazawa J.
Eur.J. Nucl. Med. Mol. Imag. Res., 3 (2013) 27.

[898] Normal values of myocardial blood flow and myocardial flow reserve evaluated by 3-dimensional dynamic PET/CT system with ^{13}N-ammonia.
Kiso K., Shimosegawa E., Watabe H., Kanai Y., Fujino K., Hatazawa J.
J. Radiol. Radiat. Therapy, **1** (2013) 1-7.

[989] Impact of cardiac support device combined with slow-release prostacyclin agonist in a canine ischemic cardiomyopathy model.
Kubota Y., Miyagawa S., Fukushima S., Saito A., Watabe H., Daimon T., Sakai Y., Akita T., Sawa Y.
J. Thoracic Cardiovasc. Surg., **147** (2013) 1081-1087.

[900] Biodistribution of (125)I-labeled polymeric vaccine carriers after subcutaneous injection.
Toita R., Kanai Y., Watabe H., Nakao K., Yamamoto S., Hatazawa J., Akashi M.
Bioorg. Med. Chem., **21** (2013) 5310-53157.

[901] Quantitative evaluation of cerebral blood flow and oxygen metabolism in normal anesthetized rats: ^{15}O-labeled gas inhalation pet with MRI fusion.
Watabe T., Shimosegawa E., Watabe H., Kanai Y., Hanaoka K., Ueguchi T., Isohashi K., Kato H., Tatsumi M., Hatazawa J.
J. Nucl. Med., **54** (2013) 283-290.

[902] Development of an ultrahigh resolution Si-PM based PET system for small animals.
Yamamoto S., Watabe H., Kanai Y., Watabe T., Kato K., Hatazawa J.
Phys. Med. Biol., **58** (2013) 7875-7888.

[903] Timing Performance of TlBr Detectors.
Hitomi K., Tada T., Onodera T., Shoji T., Kim S.-Y., Xu Y., Ishii K.
IEEE Trans. Nucl. Sci., **60** (2013) 2883-2887.

[904] Characterization of Thallium Bromide Detectors Made From Material Purified by the Filter Method.
Onodera T., Hitomi K., Tada T., Shoji T., Mochizuki K.
IEEE Trans. Nucl. Sci., **60** (2013) 3833-3836.

[905] Advances in TlBr detector development.
Hitomi K., Shoji T., Ishii K.
J. Crystal Growth, **379** (2013) 93-98.

[906] Analyzing power in elastic scattering of polarized protons from neutron-rich helium isotopes.
S. Sakaguchi, Y. Iseri, T. Uesaka, M. Tanifuji, N. Aoi, E. Hiyama, Y. Ichikawa, S. Ishikawa, K. Itoh, M. Itoh, H. Iwasaki, T. Kawabata, T. Kawahara, H. Kuboki, Y. Maeda, T. Nakao, H. Okamura, H. Sakai, Y. Sasamoto, M. Sasano, Y. Satou, K. Sekiguchi, K. Suda, D. Suzuki, A. Tamii, T. Wakui, K. Yako, M. Yamaguchi, Y. Yamamoto.
Few-body systems, **54** (2013) 1393-1398.

[907] Laser-cooled radioactive francium factory at CYRIC.
Hirokazu Kawamura, H. Arikawa, S. Ezure, K. Harada, T. Hayamizu, T. Inoue, T. Ishikawa, M. Itoh, T. Kato, T. Sato, T. Aoki, T. Furukawa, A. Hatakeyama, K. Hatanaka, K. Imai, T. Murakami, H.S. Nataraj, Y. Shimizu, T. Wakasa, H.P. Yoshida, Y. Sakemi
Nucl. Instrum. Meth. B, **317** (2013) 582-585.

[908] Novel nuclear laser spectroscopy method using superfluid helium for measurement of spins and moments of exotic nuclei.
T. Furukawa, T. Wakui, X. F. Yang, T. Fujita, K. Imamura, Y. Yamaguchi, H. Tetsuka, Y. Tsutsui, Y. Mitsuya, Y. Ichikawa, Y. Ishibashi, N. Yoshida, H. Shirai, Y. Ebara, M. Hayasaka, S. Arai, S. Muramoto, A. Hatakeyama, M. Wada, T. Sonoda, Y. Ito, T. Kobayashi, S. Nishimura, M. Nishimura, Y. Kondo, K. Yoneda, S. Kubono, Y. Ohshiro, H. Ueno, T. Shinozuka, T. Shimoda, K. Asahi, Y. Matsuo
Nucl. Instrum. Meth. B, **317** (2013) 590-594.

[909] Development of a helium cryostat for laser spectroscopy of atoms with unstable nuclei in superfluid helium.
K. Imamura, T. Furukawa, T. Wakui, X. F. Yang, Y. Yamaguchi, H. Tetsuka, Y. Mitsuya, Y. Tsutsui, T. Fujita, Y. Ebara, M. Hayasaka, S. Arai, S. Muramoto, Y. Ichikawa, Y. Ishibashi, N. Yoshida, H. Shirai, A. Hatakeyama, M. Wada, T. Sonoda, Y. Ito, H. Odashima, T. Kobayashi, H. Ueno, T. Shimoda, K. Asahi, Y. Matsuo
Nucl. Instrum. Meth. B, **317** (2013) 595-598.

[910] Control of stopping position of radioactive ion beam in superfluid helium for laser spectroscopy experiments.
X. F. Yang, T. Furukawa, T. Wakui, K. Imamura, H. Tetsuka, T. Fujita, Y. Yamaguchi, Y. Tsutsui, Y. Mitsuya, Y. Ishikawa, Y. Ishibashi, N. Yoshida, H. Shirai, Y. Ebara, M. Hayasaka, S. Arai, S. Muramoto, A. Hatakeyama, M. Wada, T. Sonoda, Y. Ito, T. Kobayashi, S. Nishimura, M. Nishimura, Y. Kondo, K. Yoneda, H. Ueno, T. Shinozuka, T. Shimoda, K. Asahi, Y. Matsuo
Nucl. Instrum. Meth. B, **317** (2013) 599-602.

[911] Proton polarization in photo-excited aromatic molecule at room temperature enhanced by intense optical source and temperature control.
S. Sakaguchi, T. Uesaka, T. Kawahara, T. Ogawa, L. Tang, T. Teranishi, Y. Urata, S. Wada, T. Wakui
Nucl. Instrum. Meth. B, **317** (2013) 679-684.

XI. MEMBERS OF COMMITTEES

XI. MEMBERS OF COMMITTEES (as of Jan. 1, 2014)

General

(Chairman)	Kazuhiko	Yanai	(Graduate School of Medicine)
	Sadayoshi	Itou	(Executive Vice President)
	Kazushige	Maeda	(Graduate School of Science)
	Kazuaki	Iwasa	(Graduate School of Science)
	Yoshio	Hosoi	(Graduate School of Medicine)
	Keiichi	Sasaki	(Graduate School of Dentistry)
	Noriyasu	Hirasawa	(Graduate School of Pharmaceutical Sciences)
	Akira	Hasegawa	(Graduate School of Engineering)
	Hitoshi	Shrakawa	(Graduate School of Agricultural Science)
	Kazuhiro	Sogawa	(Graduate School of Life Sciences)
	Atsuki	Terakawa	(Graduate School of Biomedical Engineering)
	Hiroaki	Abe	(Institute for Materials Research)
	Yasuyuki	Taki	(Institute of Development, Aging and Cancer)
	Nobuaki	Sato	(Institute of Multidisciplinary Research for Advanced Materials)
	Shoki	Takahashi	(University Hospital)
	Hajime	Shimizu	(Research Center for Electron Photon Science)
	Ren	Iwata	(CYRIC)
	Yasuhiro	Sakemi	(CYRIC)
	Manabu	Tashiro	(CYRIC)
	Hiroshi	Watabe	(CYRIC)
	Shozo	Furumoto	(CYRIC)
	Hirokazu	Tamura	(Graduate School of Science)
	Keiichi	Jingu	(Radiation Safety Committee, Research Promotion Council)

	Michio	Niwano	(Radiation Safety Committee, Research Promotion Council)

Cyclotron

(Chairman)	Yasuhiro	Sakemi	(CYRIC)
	Toshio	Kobayashi	(Graduate School of Science)
	Hirokazu	Tamura	(Graduate School of Science)
	Kazushige	Maeda	(Graduate School of Science)
	Kazuaki	Iwasa	(Graduate School of Science)
	Yasushi	Kino	(Graduate School of Science)
	Satoshi	Nakamura	(Graduate School of Science)
	Akira	Hasegawa	(Graduate School of Engineering)
	Atsuki	Terakawa	(Graduate School of Engineering)
	Yuki	Satoh	(Institute for Materials Research)
	Nobuaki	Sato	(Institute of Multidisciplinary Research)
	Toshimi	Suda	(Research Center for Electron Photon Science)
	Ren	Iwata	(CYRIC)
	Manabu	Tashiro	(CYRIC)
	Hiroshi	Watabe	(CYRIC)
	Takashi	Wakui	(CYRIC)
	Masatoshi	Itoh	(CYRIC)

Radiation Protection and Training of Safe Handling

(Chairman)	Kazuhiko	Yanai	(Graduate School of Medicine)
	Naohito	Iwasa	(Graduate School of Science)
	Yoshihiko	Uehara	(Graduate School of Medicine)
	Noriyasu	Hirasawa	(Graduate School of Pharmaceutical Sciences)
	Atsuki	Terakawa	(Graduate School of Engineering)
	Ikuo	Ikeda	(Graduate School of Agricultural Science)
	Kazumasa	Ohashi	(Graduate School of Life Sciences)
	Tatsuo	Shikama	(Institute for Materials Research)

	Motoaki	Sugiura	(Institute of Development, Aging and Cancer)
	Kentaro	Takanami	(University Hospital)
	Ren	Iwata	(CYRIC)
	Manabu	Tashiro	(CYRIC)
	Hiroshi	Watabe	(CYRIC)

Life Science

(Chairman)	Manabu	Tashiro	(CYRIC)
	Kazuhiko	Yanai	(Graduate School of Medicine)
	Haruo	Saito	(Graduate School of Medicine)
	Yoshio	Hosoi	(Graduate School of Medicine)
	Nobuyuki	Okamura	(Graduate School of Medicine)
	Mikiko	Suzuki	(Graduate School of Medicine)
	Keiichi	Sasaki	(Graduate School of Dentistry)
	Masahiro	Hiratsuka	(Graduate School of Pharmaceutical Sciences)
	Atsuki	Terakawa	(Graduate School of Engineering)
	Kazumasa	Ohashi	(Graduate School of Life Sciences)
	Yasuyuki	Taki	(Institute of Development, Aging and Cancer)
	Nariyasu	Mano	(University Hospital)
	Yukitsuka	Kudo	(Innovation of New Biomedical Engineering Center)
	Shozo	Furumoto	(Frontier Research Institute for Interdisciplinary Sciences)
	Ren	Iwata	(CYRIC)
	Yasuhiro	Sakemi	(CYRIC)
	Hiroshi	Watabe	(CYRIC)
	Yoshihito	Funaki	(CYRIC)
	Kotaro	Hiraoka	(CYRIC)

Prevention of Radiation Hazards

(Chairman)	Manabu	Tashiro	(CYRIC)
	Naohito	Iwasa	(Graduate School of Science)
	Yasushi	Kino	(Graduate School of Science)
	Keizo	Ishii	(Graduate School of Engineering)
	Ren	Iwata	(CYRIC)
	Yasuhiro	Sakemi	(CYRIC)
	Hiroshi	Watabe	(CYRIC)
	Takashi	Wakui	(CYRIC)
	Hideyuki	Yuki	(CYRIC)
	Katsuo	Aizawa	(CYRIC)

Research Program

(Chairman)	Yasuhiro	Sakemi	(CYRIC)
	Hirokazu	Tamura	(Graduate School of Science)
	Kazushige	Maeda	(Graduate School of Science)
	Kimiko	Sekiguchi	(Graduate School of Science)
	Kazuhiko	Yanai	(Graduate School of Medicine)
	Shin	Fukudo	(Graduate School of Medicine)
	Etsuro	Mori	(Graduate School of Medicine)
	Akira	Hasegawa	(Graduate School of Engineering)
	Atsuki	Terakawa	(Graduate School of Engineering)
	Akira	Takahashi	(Graduate School of Medicine)
	Yuki	Satoh	(Institute for Materials Research)
	Hiroyuki	Arai	(Institute of Development, Aging and Cancer)
	Yasuyuki	Taki	(Institute of Development, Aging and Cancer)
	Keiichi	Jingu	(University Hospital)
	Atushi	Takeda	(University Hospital)
	Toshimi	Suda	(Research Center for Electron Photon Science)
	Hidetoshi	Kikunaga	(Research Center for Electron Photon Science)

	Tsutomu	Sekine	(Institute Excellence in Higher Education)
	Ren	Iwata	(CYRIC)
	Manabu	Tashiro	(CYRIC)
	Hiroshi	Watabe	(CYRIC)
	Tomohiro	Kaneta	(CYRIC)
(Observer)	Takashi	Wakui	(CYRIC)
(Observer)	Masatoshi	Itoh	(CYRIC)

XII. STAFF AND STUDENTS

XII. STAFF AND STUDENTS (as of Jan. 1, 2014)

Director Kazuhiko Yanai

Division of Accelerator

Yasuhiro	Sakemi[1)]
Takashi	Wakui
Yoshihiro	Shimbara
Yasuaki	Ohmiya[2)]
Naoto	Takahashi[2)]
Jyunya	Suzuki[2)]
Ken	Takahashi[2)]
Takayuki	Honma[2)]

Division of Instrumentations

Yasuhiro	Sakemi
Hirokazu	Tamura[3)]
Atsuki	Terakawa[4)]
Masatoshi	Itoh
Kenichi	Harada
Takeshi	Inoue

Division of Radiopharmaceutical Chemistry

Ren	Iwata
Yukitsuka	Kudo[5)]
Shozo	Furumoto[6)]
Yoshihito	Funaki
Yoichi	Ishikawa
Kazuko	Takeda

Division of Cyclotron Nuclear Medicine

Manabu	Tashiro
Miho	Shidahara[6)]
Kotaro	Hiraoka
Shoichi	Watanuki

Division of Radiation Protection and Safety Control

Hiroshi	Watabe
Keizou	Ishi[4)]
Shigeo	Matsuyama[4)]
Seong-Yun	Kim[4)]
Keitaro	Hitomi[4)]
Masayasu	Miyake
Hideyuki	Yuki
Kazuhiro	Ohtomo
Hirokazu	Nakae[7)]

Undergraduates and Graduate Students

Tomohiro	Hayamizu	(Graduate School of Science)
Hiroshi	Arikawa	(Graduate School of Science)
Shun	Andou	(Graduate School of Science)
Taisuke	Ishikawa	(Graduate School of Science)
Kou	Kato	(Graduate School of Science)
Takahiro	Aoki	(Faculty of Science)
Aiko	Uchiyama	(Faculty of Science)
Kousuke	Sakamoto	(Faculty of Science)
Tetsuro	Tago	(Graduate School of Pharmaceutical Sciences)
Tomomitsu	Iida	(Graduate School of Pharmaceutical Sciences)
Takahiro	Tominaga	(Graduate School of Pharmaceutical Sciences)
Hajime	Adachi	(Faculty of Pharmaceutical Sciences)
Azusa	Kazama	(Faculty of Pharmaceutical Sciences)

Kazumi	Mikado	(Faculty of Pharmaceutical Sciences)
Yujyu	Abe	(Faculty of Pharmaceutical Sciences)
Rikuto	Ichihara	(Faculty of Pharmaceutical Sciences)
Akie	Inami	(Graduate School of Medicine)
Rinn	Matsuda	(Graduate School of Medicine)

Office Staff

Kiyohiro	Sasaki
Katsuo	Aizawa
Namiko	Ito
Shinya	Terui
Kyoko	Fujisawa
Katsuo	Ibuka
Yoshio	Muroi
Kei	Ito
Miki	Yashima
Yumi	Kurashima
Hiroko	Ishiguro
Nayoko	Aota
Fumiko	Mayama
Ikuko	Tojo

1) Division of Instrumentation
2) SUMI-JU Accelerator Service Ltd.
3) Graduate School of Science
4) Graduate School of Engineering
5) University Hospital
6) Graduate School of Medicine
7) Japan Radiation Protection Co., Ltd.